The Electronic and Atomic Structure of Actinide Contaminants at the Mineral-Fluid Interface

by

Benjamin Bartholomew Gebarski

A dissertation submitted in partial fulfillment
of the requirements for the degree of
Doctor of Philosophy
(Earth and Environmental Sciences)
in The University of Michigan
2018

Doctoral Committee:

Professor Udo Becker, Chair
Assistant Professor Rose M. Cory
Assistant Professor Brian R. Ellis
Professor Kim F. Hayes
Professor Donald J. Siegel

Benjamin Bartholomew Gebarski

bbge@umich.edu

ORCID ID: 0000-0002-9391-9950

DEDICATION

For my parents,

Kathleen and Stephen

ACKNOWLEDGEMENTS

First and foremost I would like to thank my advisor, Udo Becker, whom I have known these many years for his support and guidance in both my undergraduate and graduate studies. Great thanks are also due to the members of my thesis committee, Rose Cory, Brian Ellis, Kim Hayes, and Don Siegel for their time and invaluable insight.

I would also like to thank my friends and family, especially Meg and Jeremy Jorgenson, Matt Gebarski, Lizzie and Ryan Payne, Ian Glanville, Mark Relson, and Peiyu Yu, whose constant support and compassion has seen me through this five-year journey.

Special thanks goes to my research group members, Sandy Taylor, Ke Yuan, Sarah Walker, Sulgiye Park, Will Bender, Evan Killeen, Youngjae Kim, Peter Cook, Sooyeon Kim, Saumitra Saha, and Krish Arumugam, some of the kindest and brightest people I have ever known. I am also especially grateful to Maria Marcano, Mike Messina, and Jerry Li for their extensive knowledge and research support.

I would also like to acknowledge the support of my collaborators, Benjamin Reinhart of ANL for his mentorship and guidance during my 6-month fellowship at APS; Mark Antonio of ANL for his insight, comments, and the use of his labs; Soenke Seifert of ANL for his assistance and generosity; and to Greg Dick of UM for the extensive use of his lab.

Thanks are due as well to the staff of the Department of Earth and Environmental Sciences, especially Anne Hudon for keeping me on track; Nancy Kingsbury for her financial assistance;

Bill Wilcox and Craig Delap for their careful maintenance and expertise; as well as Bill Custer and Steven Moser for their help sorting out a myriad of technical difficulties.

Thank you all so much!

TABLE OF CONTENTS

DEDICATION ii

ACKNOWLEDGEMENTS iii

LIST OF TABLES vii

LIST OF FIGURES ix

ABSTRACT xiii

CHAPTER 1 Introduction 1

1.1 Background 2

1.2 Overview of Research Chapters 11

1.3 Advantages and Complementarity of the Multi-method Approach 14

1.4 Works Cited 18

CHAPTER 2 Electrochemical Analysis of the Kinetics of Oxidation/Reduction Reactions of the Peroxide-Containing Mineral Studtite in Comparison to Uranyl Peroxide Clusters (U_{60}) 24

2.1 Abstract 24

2.2 Introduction 26

2.3 Materials and Methods 30

2.4 Results and Discussion 35

2.5 Conclusions 64

2.6 Acknowledgements 65

2.7 Appendix 66

2.8 Works Cited 71

CHAPTER 3 Surface-Mediated Reactions of Uranyl Peroxide Materials U_{60} and Studtite at the Mineral-Electrolyte Interface 77

3.1 Abstract 77

3.2 Introduction 78
3.3 Materials and Methods 83
3.4 Results 86
3.5 Discussion 105
3.6 Conclusions 108
3.7 Acknowledgements 109
3.8 Appendix 110
3.9 Works Cited 111

CHAPTER 4 Quantum Mechanical Determination of the Incorporation of Pentavalent Plutonium into Carbonate and Sulfate Minerals 116

4.1 Abstract 116
4.2 Introduction 118
4.3 Materials and Methods 122
4.4 Results and Discussion 124
4.5 Conclusions 147
4.6 Further Research 149
4.7 Acknowledgements 150
4.8 Appendix 150
4.9 Works Cited 151

CHAPTER 5 Conclusions 155

5.1 Works Cited 159

LIST OF TABLES

Table 2.1: Published Standard Reduction Potentials versus SHE (Austin et al., 2009; Bard and Faulkner, 2001; Bratsch, 1989) at pH 0 and pH 5. 38

Table 2.2: U(VI)/U(V) redox couples for selected uranyl compounds with differing ligands (vs. SHE)..... 40

Table 2.3: U(V)/U(IV) species in solution with associated theoretical peak shift values (x) and standard electrode potentials E° (vs. SHE). 52

Table 2.4: U(V)/U(IV) species with equilibrium constant and Gibbs free energy change [J/mol] calculated from thermodynamic data as pertains to experimental conditions in this study..... 53

Table 2.5: Percent contribution of U^{4+} species to the U(V)/U(IV) reaction calculated from Figure 2.3..... 57

Table 2.6: Electrode potentials at varied pH as predicted from standard reduction potentials and reaction quotient..... 57

Table 2.7: Electrode potentials at varied pH as predicted from experimentally relevant conditions, reactions, and the reaction quotient. 57

Table 2.8: From left to right: U^{6+} free energy of formation difference between uranyl complex and $UO_2(H_2O)_5$, U^{5+} free energy of formation difference between uranyl complex and $UO_2(H_2O)_5$, the expected shift in E_{mid} from the standard redox potential of UO_2^{2+} (+0.160 V), the expected E_{mid} of the uranyl complex using the calculated E_{mid} shift, the actual E_{mid} observed from experiments. 62

Table 3.1: Uranium/potassium relative ratio based on characteristic Auger peak heights. 105

Table 4.1: Incorporation energies for PuO_2^+ incorporation into selected sulfate and carbonate host minerals using solid oxide sources and sinks. The reaction energy is calculated utilizing CASTEP with an assigned Hubbard U parameter of 4 eV using Eqns. 7 for carbonates and 8 for sulfates. 130

Table 4.2: Plutonyl (PuO_2^+) incorporation into barite ($BaSO_4$). Transformation from solid oxide to charged aqueous source and sink. 137

Table 4.3: Plutonyl (PuO_2^+) incorporation into calcite ($CaCO_3$). Transformation from solid oxide to charged aqueous source and sink. 138

Table 4.4: Calculated hydration energies for small ionic species as compared with literature values (Marcus, 1994; Rashin and Honig, 1985; Shuller et al., 2013). The reaction energy is calculated utilizing DMol3 with the COSMO solvation model..... 140

Table 4.5: Incorporation energies for PuO_2^+ incorporation into selected sulfate and carbonate host minerals using aqueous sources and sinks as described in Tables 4.2 and 4.3. The reaction energy is calculated utilizing $DMol^3$ with the COSMO solvation model using Table 4.3 for carbonates and Table 4.2 for sulfates..... 140

Table 4.6: Incorporation energies for PuO_2^+ incorporation into selected sulfate and carbonate host minerals using aqueous sources and sinks as described using Equations 7 and 8. The reaction energy is calculated utilizing $DMol^3$ with COSMO solvation model using Equation 7 for carbonates and Equation 8 for sulfates.. 146

Table 4.7: Experimental vs. calculated Pu(V)-O distances. Calculations account for differing lengths for each of the two Pu-O bonds in PuO_2^+..... 147

Table 4.8 - Appendix: Unstable SrO, CaO, PbO, and BaO species are removed from reaction (1) and (2). The reaction energy is calculated utilizing CASTEP. 150

Table 4.9 - Appendix: Incorporation energies for PuO_2^+ incorporation into selected sulfate and carbonate host minerals using solid oxide sources and sinks. The reaction energy is calculated utilizing CASTEP with and without an assigned Hubbard U parameter using Eqns. 5 for carbonates and 6 for sulfates..... 150

Table 4.10 - Appendix: Incorporation energies for PuO_2^+ incorporation into selected sulfate and carbonate host minerals using solid oxide sources and sinks. The reaction energy is calculated utilizing CASTEP without an assigned Hubbard U parameter using Eqns. 7 for carbonates and 8 for sulfates..... 151

Table 4.11 - Appendix: Incorporation energies for PuO_2^+ incorporation into selected sulfate and carbonate host minerals using solid oxide sources and sinks. The reaction energy is calculated utilizing $DMol^3$ using Eqns. 5 for carbonates and 6 for sulfates. 151

Table 4.12 - Appendix: Incorporation energies for PuO_2^+ incorporation into selected sulfate and carbonate host minerals using solid oxide sources and sinks. The reaction energy is calculated utilizing $DMol^3$ using Eqns. 5 for carbonates and 6 for sulfates. 151

LIST OF FIGURES

Figure 1.1: A simplified diagram of the nuclear fuel cycle adapted from Schène (2007). Arrows in yellow denote the front-end of the cycle. Arrows in red signify the shift from a closed loop in the cycle (reprocessing) to an open loop (once through to disposal). Arrows in blue represent the back-end of the cycle wherein radioactive waste is treated, discarded, and disposed of in geologic repositories. This dissertation is focused on the back-end of this cycle, where radioactive contaminants have the greatest likelihood of entering the environment. **a.)** The extraction of U ore. **b.)** The enrichment of U ore to higher concentration of ^{235}U. **c.)** Nuclear fuel undergoing fission in a reactor to produce electricity. **d.)** Spent fuel can be reprocessed or directly discarded. **e.)** An underground nuclear waste repository. 4

Figure 2.1: **Red:** Empty PME in Na_2SO_4 solution at pH 5 demonstrating the electrochemical background. Distinct redox peaks are attributed to the reduction of Pt. **Black:** U_{60} in Na_2SO_4 solution at pH 5 demonstrating the redox behavior of powdered U_{60} crystals. The C_2/A_2 couple is attributed to the U(VI)/U(V) transition and the C_3/A_3 couple to the U(V)/U(IV) transition. Arrows represent scan direction. 37

Figure 2.2a: CV of U_{60} in progressively higher concentrations of $UO_2(NO_3)_2$ solution at constant pH 5. Growth of peaks indicates which peaks are uranium related (C_3, C_4, A_4, A_3). Stable peaks could denote the redox behavior of U_{60}'s peroxide constituents. Position A_5 does not represent a peak but rather an artifact of the potential reversal in CV. Two separate cathodic peaks indicate a two-step reduction of U(VI). Two overlapped anodic peaks suggest two oxidation processes at similar potential. 48

Figure 2.3: Log Concentration (Molal) vs. Solution pH diagram. Solution conditions from Figure 2.2 are modelled (2.3 mM $UO_2(NO_3)_2$). Curves have been normalized to reflect concentration of U^{4+} species only - some species are omitted for clarity. 54

Figure 2.4: Thermodynamically-derived pH shift vs. observed pH shift in experimental conditions (U_{60} PME in a 2.3 mM uranyl nitrate solution). Calculated values consistently underestimate observed pH shift. 56

Figure 2.5: (a.) U_{60} cluster molecular model. (b.) Studtite unit cell. (c.) U_{60} fragment from one of the uranyl centers in (a.). (d.) Studtite fragment from one of the uranyl centers in (b.). 63

Figure 2.6 - Appendix: (a.) U_{60} polyhedral illustration from (Burns, 2011) (b.) U_{60} wireframe graphical illustration from (Burns, 2011) (c.) Traditional soccer ball from MS Clipart. 66

Figure 2.7 - Appendix: Cell design used for *in situ* synchrotron solid-state electrochemical x-ray absorption spectroscopy. 68

Figure 2.8 - Appendix: *Ex situ* XAS Spectra of U_{60} (blue) and studtite (red). 70

Figure 2.9 - Appendix: Fourier transform rendering of U_{60} (blue) and studtite (red) uranium R-space showing U distances and multiple scattering effects. 70

Figure 3.1: Eh-pH (speciation) diagrams predict the species and oxidation state present as a function of redox potential and pH in reference to both environmentally-relevant and repository conditions. Eh-pH diagram for Fe (left) shows $FeOH^+$ (green rust) phase is expected for reducing conditions at pH 10.8. This is confirmed by observation of green rust at the steel surface. Eh-pH diagram for U (right) predicts a U(IV) phase at similar conditions. This is confirmed by observation of U_{60} clusters at the substrate surface. 83

Figure 3.2: AFM image of a steel surface in 1 M KCl solution at pH 10.8 **(1)** EC-AFM peak force error (PFE). **(2)** EC-AFM height image. **A:** Steel surface in air demonstrates the baseline surface. **B:** Steel surface in 1 M KCl solution at open circuit potential (OCP) exhibits growth of small KCl precipitates. **C:** Steel surface in 1 M KCl solution at reducing potential (-1000 mV) results in the breakdown of both the precipitated material as well as the uppermost layers of the steel surface. 88

Figure 3.3: Eh-pH diagram for a 1 M KCl solution. 89

Figure 3.4: AFM image of Steel surface in 1.6 mM U_{60} solution at pH 10.6 **(1)** EC-AFM peak force error (PFE) image. **(2)** EC-AFM height image. **A:** Steel surface in air demonstrates the baseline surface. **B:** Steel surface in U_{60} solution at open circuit potential (OCP) exhibits growth of small precipitates. **C:** Steel surface in U_{60} solution at reducing potential (-0.5 V vs. SHE) results in accelerated growth of precipitates shown here with polygonal sorbates (crystalline U_{60}). 91

Figure 3.5: AFM image of steel surface in 1.6 mM U_{60} solution at pH 10.6 **(1)** EC-AFM peak force error (PFE) image. **(2)** EC-AFM height image. **A:** Steel surface in U_{60} solution at open circuit potential (OCP) exhibits growth of small precipitates. **B:** Magnified steel surface in U_{60} solution at OCP exhibits the formation of U_{60} composite clusters. **C:** Magnified steel surface in U_{60} solution at OCP shows single composite cluster. 92

Figure 3.6: Sorbate quantification from EC-AFM imagery processing. Sorbate metrics in 1.6 mM U_{60} solution at pH 11 at OCP. **A**: Number of sorbates versus time. **B**: Mean sorbate area. **C**: Mean sorbate density. **D**: Mean sorbate diameter. **E**: Mean sorbate height. **F**: Mean sorbate volume. 93

Figure 3.7: SEM backscattered electron images of U adsorbate (Site 1). The 10-50 nm needlelike structures observed are composed of uranium oxide. 96

Figure 3.8: SEM-EDS Site 1. SEM-EDS composite image (left) showing steel surface (red, Spectrum 1) and uranium-bearing adsorbates (yellow, Spectrum 2). EDS **Spectrum 1** (right) shows the high Fe and C concentrations characteristic of steel. Minor U concentrations result from a thin layer of small adsorbates coating the majority of the surface. EDS **Spectrum 2**

(right) demonstrates composition of adsorbates. High U and O concentrations are characteristic of the needlelike sorbates. Spectrum 2 continues to return a Fe signal due to the steel substrate beneath coupled with the sampling depth and excitation volume of our instruments. 97

Figure 3.9: SEM Backscattered Electron images of U adsorbate (Site 2). Site 2 has a structure that appears as composite clusters of U_{60}. Representative images are difficult to obtain as the maximum resolution for the JEOL Instrument is 10 nm (roughly 4 times the diameter of U_{60}).. 98

Figure 3.10: SEM-EDS Site 2. SEM-EDS map (top) showing distribution of U-containing material. SEM-EDS spectrum (bottom) showing U and K composition characteristic of U_{60}..... 99

Figure 3.11: SEM Site 3. **A)** U-dense regions (lighter color) correspond with patches of the observed spherical nanoparticles attributed to uranyl peroxide cluster formation. **B)** Less U-dense regions (darker color) correspond with the U-associated needle-like particles observed in Site 1. 100

Figure 3.12: AES/SEM backscatter image of crystalline sorbates. (A.) U_{60} crystal grown according to the literature. (B.) U_{60} sorbate from EC-AFM experiments. 102

Figure 3.13: AES/SEM backscatter image of U_{60} composite cluster sorbates. **(A)** U-containing composite cluster sorbates. **(B)** Unaltered substrate surface (steel). **(C)** Steel surface corrosion. Exposure of steel surface and U_{60} solution to reducing potentials also forms green rust [$Fe(OH)_2$]. 103

Figure 3.14: Differentiated AES spectra. (1) **A**, **B**, and **C**: Auger spectra of crystalline U_{60} standard illustrated in Fig. 3.12A. Point compositional spectra for U adsorbate shows the presence of U, O, Fe, and K. Auger transitions shown from left to right: U L1, K L1, O L1, O L1, and Fe L3 (U L3 omitted for clarity). (2) **A**: Spectra of crystalline sorbate illustrated in Fig. 3.12B. **B**: Spectra of composite cluster sorbate illustrated in Fig. 3.13A. **C**: Spectra of unaltered steel surface background. 104

Figure 3.15: C_{60} Fullerenes vs. SEM Site 3. **A)** C_{60} fullerenes with fibrous interconnecting carbon nanotubes from (Umeyama and Imahori, 2008). **B)** SEM Site 3, note the fibrous interconnection between U nanoparticles. These fibers are reminiscent of carbon nanotubes found on C_{60} buckyballs. This could suggest the existence of a uranyl peroxide nanotube. 108

Figure 3.16 - Appendix: Schematic of EC-AFM cell from Bruker Inc. 110

Figure 3.17 - Appendix: Rigged EC-AFM cell ready to receive solution. 111

Figure 4.1: Simplified diagram of incorporation pathways for (an example) calcite ($CaCO_3$) host mineral. (a.) Host and incorporated species calculated separately. (b.) Adsorption of PuO_2^+ onto host surface. (c.) Incorporation of PuO_2^+ into the host surface layer. (d.) Incorporation of PuO_2^+ into the host bulk. 121

Figure 4.2: Simplified diagram of an example incorporation reaction. Host mineral ($CaCO_3$/$BaSO_4$) + Pu Source (Pu_2O_5) ⇌ Pu-Incorporated Host Mineral + Cation Sink (CaO/BaO) 126

Figure 4.3: Plutonyl incorporated into the surface of A.) celestine ($SrSO_4$), B.) aragonite ($CaCO_3$), C.) barite ($BaSO_4$), D.) anglesite ($PbSO_4$), E.) anhydrite ($CaSO_4$), and F.) calcite ($CaCO_3$). In each cell, one divalent cation is replaced by a PuO_2^+ and H^+ for charge compensation. H: white, O: red, S: yellow, Ca, Sr, Ba: green, Pb: grey, Pu: blue. 134

Figure 4.4: Coordination environment in the bulk of A.) celestine ($SrSO_4$), B.) aragonite ($CaCO_3$), C.) barite ($BaSO_4$), D.) anhydrite ($CaSO_4$), and E.) calcite ($CaCO_3$). H: white, O: red, S: yellow, Ca, Sr, Ba: green, Pu: blue. 135

Figure 4.5: Example incorporation cycle for the barite mineral host. A.) aqueous PuO_2^+ and HSO_4^- with a host mineral surface. B.) PuO_2^+ and HSO_4^- adsorbed to a mineral surface. C.) PuO_2^+ and SO_4^{2-} incorporated into the surface of the host mineral, with a Ba^{2+} and SO_4^{2-} released into solution. D.) PuO_2^+ and HSO_4^- incorporated into the bulk mineral structure. E_1) the change in incorporation energy (E_{inc}) between structure (A) and (B). E_2) the change in E_{inc} between (B) and (C). E_3) the change in E_{inc} between (A) and (C). E_4) the change in E_{inc} between (C) and (D). E_5) the change in E_{inc} from (A) to (D). 145

Figure 4.6: Incorporation cycle for all host minerals. Each step is representative of the net energy gain or loss (in eV) from each incorporation step from solution (starting point) to adsorption, surface incorporation, and finally to bulk incorporation. 146

ABSTRACT

Geochemical reactions at the mineral-water interface are a critical factor in the mobility of actinide contaminants such as those intrinsic to nuclear waste storage facilities. Actinides can undergo a number of sorption, phase, and oxidation state changes that control their interactions with the surrounding environment. This dissertation investigates the redox behavior, sorption, thermodynamics, and kinetics of actinides at a near-atomistic scale in order to further the understanding of actinide chemistry in the environment. Novel and combined multi-method approaches utilizing experimentation and atomistic modeling were developed to achieve a detailed understanding of both naturally-occurring and synthetic actinides, specifically uranium (U) and plutonium (Pu), and the mechanisms that may lead to their immobilization at the mineral-fluid interface.

In reducing conditions, soluble uranyl(VI) (UO_2^{2+}) can be reduced to insoluble U(IV)O_2 solid, resulting in the decrease of its mobility within the environment. Chapter 2 is an electrochemical investigation of U(VI) redox interactions in a relatively uncharacterized synthetic uranyl peroxide material called uranium-60 nanoclusters (U_{60}) and their natural analog, the mineral studtite. Results indicate a two-step, one-electron irreversible reduction of U(VI) to U(IV) resulting in the fragmentation of the U_{60} cluster and the studtite crystalline structure. Utilizing a combined approach with spectroscopic and computational methods, electrochemical redox responses were assigned to specific or concurrent reactions, possibly indicating the existence of an uncommon U(V) superoxo intermediate phase within U_{60} clusters.

Actinide contaminants such as uranyl peroxides can also be immobilized via redox or adsorption reactions catalyzed by mineral surfaces. Therefore Chapter 3 uses electrochemical atomic force microscopy (EC-AFM) in conjunction with spectroscopic methods to image redox reactions and sorbates at the mineral-fluid interface directly. Results indicate the growth of U_{60} nanostructures adsorbed to mineral surfaces in either face-centered cubic (FCC) crystalline or composite clusters, the fragmentation of U_{60} upon reduction, and the observation of a fibrous nanoparticle that could be completely uncharacterized in the literature.

Actinides exceptionally mobile in aqueous conditions, such as pentavalent plutonyl (PuO_2^+), can be immobilized without a change in oxidation state via adsorption or incorporation into mineral hosts. Thus, Chapter 4 is a theoretical investigation of incorporation of plutonyl [Pu(V)] ions into carbonates and sulfates; minerals ubiquitous in subsurface environments. This chapter describes new *ab initio* modeling methodology using quantum mechanics to calculate equilibrium energetics, hydration, and thermodynamics to assess structural and electronic changes in the host mineral. Results suggest that barite group and aragonite mineral structures with orthorhombic symmetry, high coordination number, and large ionic radii have greater interstitial cell space and are therefore more favorable for PuO_2^+ incorporation than other host minerals. The contribution to existing incorporation methodology is the consideration of mineral surfaces. Findings from this study have substantial implications for the long-term sequestration of mobile actinide contaminants.

CHAPTER 1

Introduction

Understanding the interactions at the mineral surface is key to understanding the chemistry, in particular the thermodynamics and kinetics, of natural systems. All interactions between a mineral and its surrounding environment take place at its surface. These surface interactions control the chemistry and mobility of contaminants such as radionuclides, especially in subsurface environments (Geckeis et al., 2013; Poinssot and Geckeis, 2012). The mobility of radionuclides in the environment is highly dependent on sorption, redox reactions, and several other interfacial geochemical processes. This dissertation focuses on understanding interactions at the mineral-fluid interface and their relation to the mobility of actinide contaminants such as uranium (U) and plutonium (Pu) in natural systems. Actinide sorption, incorporation, and redox reaction mechanisms occurring on common mineral surfaces and relatively uncharacterized uranyl compounds are investigated, and conclusions as to their behavior and mitigation within the environment are proposed. This is achieved by a combination of experimental and quantum-mechanical theoretical approaches. Chapter 2 of this dissertation uses electrochemistry, complemented by spectroscopic methods for reaction product analysis, to investigate the redox behavior of U in solution and within solid structures of U_{60} nanoclusters and the mineral studtite (including catalytic effects of U_{60}). Chapter 3 combines this electrochemical and spectroscopic approach with surface probe techniques (atomic force microscopy, AFM) to determine the local lateral mechanism of these surface-mediated redox reactions. To further explore the mechanisms

at work in Chapters 2 and 3, Chapter 4 uses quantum mechanical modeling to study the thermodynamics and approximate the kinetics of the stepwise incorporation of plutonyl ions from solution onto and into the surface of different minerals prior to incorporation into their bulk structure.

1.1 Background

The actinide elements U and Pu are used world-wide for three major applications: **1.** Nuclear weapons development and testing for defense projects. **2.** Scientific research to explore new applications, risk assessments, and actinide contamination mitigation strategies. **3.** Commercial nuclear power plants, which harness the high energy density of actinide fuels while producing low carbon emissions. The fate of all these actinide material applications and the methods required to produce them ultimately results in the production of huge quantities of nuclear waste. Nuclear power plants, by virtue of the world's growing demand for power (and the efficiency of such installations), are by far the largest contributor to this nuclear waste stream. The nuclear fuel cycle shown in Figure 1.1 describes the process by which uranium ore (mixed UO_2, Fig. 1.1a) is mined, processed, and enriched (from >1% ^{235}U to higher grades, Fig. 1.1b) to produce nuclear fuel (typically 100% UO_2). The fuel is then loaded into a reactor to undergo controlled fission, releasing heat which can then be harnessed to generate electricity (Fig. 1.1c). The back-end (disposal end) of the nuclear fuel cycle begins after the fuel has completed its useful life within the reactor and is put in interim storage in order to await the controlled decay of the highly radioactive short-lived isotopes (half-lives of less than 100 years), mainly fission products such as ^{131}I, ^{137}Cs, and ^{90}Sr (Ewing, 2015). The spent nuclear fuel (SNF) is at this point still about 95% UO_2 and can then undergo reprocessing (Fig. 1.1d) to extract fissile elements such as ^{239}Pu and ^{235}U and return to the front-end (supply end) of the nuclear fuel cycle.

Reprocessing does however increase the proportion of highly radioactive and longer-lived actinide elements such as ^{239}Pu, ^{237}Np, and ^{241}Am, with half-lives ranging from hundreds to millions of years. As a result of this problem, reprocessing is not typically performed in nuclear power programs except in France, Russia, Japan, and China. Either way, substantial nuclear waste is generated throughout this cycle and must be stored on-site to await long-term storage in a waste repository (Fig. 1.1e) (Burns and Finch, 1999; Ewing, 2015).

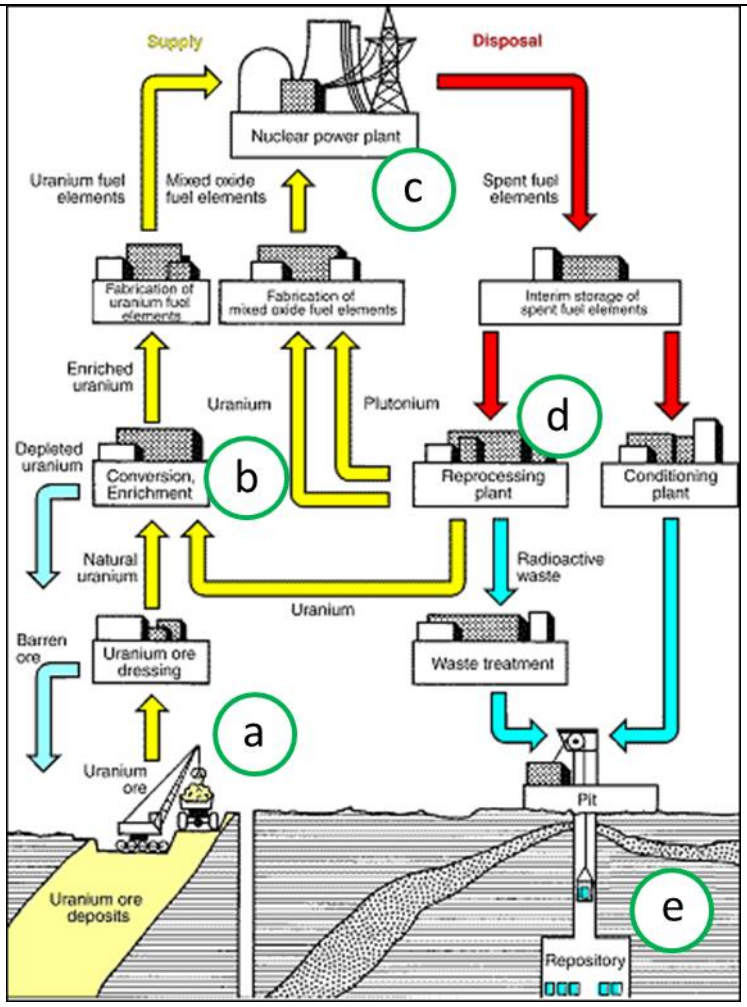

Figure 1.1: A simplified diagram of the nuclear fuel cycle adapted from Schène (2007). Arrows in yellow denote the front-end of the cycle. Arrows in red signify the shift from a closed loop in the cycle (reprocessing) to an open loop (once through to disposal). Arrows in blue represent the back-end of the cycle wherein radioactive waste is treated, discarded, and disposed of in geologic repositories. This dissertation is focused on the back-end of this cycle, where radioactive contaminants have the greatest likelihood of entering the environment. **a.)** The extraction of U ore. **b.)** The enrichment of U ore to higher concentration of ^{235}U. **c.)** Nuclear fuel undergoing fission in a reactor to produce electricity. **d.)** Spent fuel can be reprocessed or directly discarded. **e.)** An underground nuclear waste repository.

For the past 50 years, there has been an extensive international effort to develop strategies for the disposal of nuclear waste. With about 300,000 metric tons of radioactive fuel waste material accumulated globally over the years and an additional 10,000 metric tons produced each year from nuclear power plants alone, the proper disposal of SNF is of great importance. Of the many

disposal strategies proposed, disposal in a geologic repository remains the only viable, safe, and long-term method for all SNF waste types. Repository locations are chosen based upon the local geology and hydrology with respect to the eventual failure of the nuclear waste containers. For example, the Waste Isolation Pilot Plant (WIPP) located near Carlsbad, NM is mined into the center of a 610 m-thick salt formation located 655 m underground. Salt formations like those at WIPP have the benefit of being structurally sound and free of circulating ground water, thus preventing contaminants from leaking through rock fractures or being transported by groundwater. The disadvantages stem from the plastic behavior of salt formations, which are unable to accommodate dense loading of waste. The salt also flows into excavated rooms, sealing them off permanently after several years, thus preventing later retrieval (Timm and Fox, 2011). Another repository type, the Yucca Mountain repository, is located in the Nevada desert, mined 300 m below the surface into a solid mass of volcanic tuff. The benefits of repositories like Yucca are the low precipitation, permeability, water table, and population in the surrounding area. The drawbacks include the frequent seismicity and the formation of fissures within the tuff that can aid the transport of contaminant material (Bodvarsson et al., 1999; Long and Ewing, 2004). On the other hand, the ANDRA site in Bure, France is a repository bored into an aquitard formation 500 m beneath the surface. The benefits of this site include the low permeability (less than 30 m/million years) and the drawbacks stem from the low structural stability of the clay formations (Delay et al., 2008; Gaucher et al., 2004). When selecting repository locations like these, careful attention must also be paid to redox conditions within the subsurface environment, as repositories located in reducing environments (such as those containing reducing agents) are orders of magnitude more stable than those in oxidizing conditions (Ewing and Macfarlane, 2002).

Geological disposal of nuclear waste in salt, crystalline rock, clay, and volcanic tuffs persists as the preferred method of disposal due to the high levels of radioactivity in waste that can remain harmful for hundreds of thousands of years. Although many geologic repositories across the globe have been built, they contain only low- and intermediate-level waste (materials less radioactive than SNF). No repository for the disposal of accumulating high-level radioactive waste currently exists. Despite several planned sites for the disposal of high-level nuclear waste, the difficulty inherent in the radioactivity of waste, the heat produced from decay, and the selection of a site guaranteed to be stable for hundreds of thousands of years causes great uncertainty concerning the long-term safety of the site (Bruno and Ewing, 2006). Political factors add further delays as local laws and communities obstruct the construction of repositories, disputing both scientific and safety findings.

Until a viable geological repository is found, temporary on-site storage measures for high-level radioactive waste are implemented across the world. The majority of these sites are rapidly degrading, with soils and groundwater having been contaminated with actinides such as U and Pu worldwide. In the US alone, there are at least 76 Superfund sites (hazardous waste sites) that are contaminated with radioactive waste from spills or failed containment (EPA, 2012). For example, the Hanford site in WA, which produced Pu for the U.S. Department of Defense from 1943 to 1987, resulted in the Pu and U contamination of 12 million cubic meters of soil (Powell, 2012). Other notable sources of actinide contamination have been found in both civilian and defense operations, decommissioned uranium mines, and the oil and gas industry (Brown and Calas, 2012; Maher et al., 2013).

The future disposal of SNF poses an even greater risk than those observed from the defense and mining industries; as the stockpiles of used fuel continue to grow with no tangible plans for

their eventual disposal. Contamination from these temporary sites is of great concern. Should a suitable geologic repository be selected for the disposal of SNF, the same concerns remain about eventual contamination. The primary difficulty in the selection of a nuclear waste site is predicting the complex chemical interactions that influence the transport of actinides over hundreds of thousands of years. Water that comes into contact with steel fuel containment canisters will eventually cause corrosion, leading to the release of aqueous U, Pu, Fe, and other species into the subsurface environment. The extent to which leakage can infiltrate a site is controlled by the mobility of the actinide contaminants. Contaminant mobility is controlled primarily by the redox and sorption reactions that occur between minerals and the radioactive contaminants themselves (Kim and Grambow, 1999). In order to predict the extent of the migration of actinide contaminants and therefore devise strategies for their remediation, a detailed understanding of their environment, its aqueous geochemistry, and the potential chemical reactions involved is needed.

The purpose of this dissertation is to advance our understanding of the interactions between actinides, minerals, and metals that are present in nuclear repository conditions, with a focus on how redox mechanisms and sorption can control actinide mobility. Redox reactions have a great influence on the mobility of actinides due to the fact that their aqueous solubility is controlled by their chemical oxidation state (Brown and Calas, 2012; Roberts et al., 2003). Actinides are known for existing in several oxidation states; for example, U is found in the trivalent (U(III)), tetravalent (U(IV)), pentavalent (U(V)), and hexavalent (U(VI)) states. Of these, the tetravalent and hexavalent state are the most common in natural environments, and the pentavalent state has been recently found to be of increasing importance as a temporary state (Arnold et al., 2009; Renock et al., 2013; Yuan et al., 2015a; Yuan et al., 2015b). The presence of a particular

oxidation state is predicated by the local conditions, such as reducing or oxidizing environments, pH, and mineral species. U(VI) is known to be dominant in oxidizing conditions, such as those found in the stalled U.S. Yucca Mountain repository. U(IV) is known to be found in reducing environments such as the unfinished French ANDRA Bure site. U(VI) is soluble as the uranyl ion (UO_2^{2+}), and is therefore highly mobile within groundwater found in subsurface geologic repositories. U(IV) is however insoluble, precipitating to the mineral uraninite ($UO_{2(s)}$) and is therefore far less mobile. Given this, if an environment can be altered via the introduction of reducing compounds such as Fe(II), the highly mobile U(VI) in a given environment can be effectively immobilized as U(IV).

In order to immobilize actinide contaminants within natural systems, one must also consider the sorption reactions taking place, as they control whether actinides are dissolved in water or attached to mineral surfaces. Soluble, and therefore mobile, actinides like U(VI) can be adsorbed to reactive functional groups on mineral surfaces, thereby removing the contaminant from solution. The adsorbed actinide's mobility is then controlled by the transport of the host mineral grain. Adsorbed actinides are sensitive to changes in the redox characteristics of their environment and are just as easily desorbed as they are adsorbed. By allowing the mineral with the adsorbed actinide contaminant to grow, the actinide is then incorporated into the host mineral structure (absorption), making the immobilization far more stable. The sorption and redox processes at the mineral surface that control the mobility of actinide contaminants is the primary focus of this dissertation.

There are a number of studies concerned with the remediation of sites contaminated with actinides through the manipulation of redox and sorption reactions occurring at the mineral-fluid interface. The most common methods achieve remediation via permeable reactive barriers (Gu et

al., 1998; Morrison et al., 2001), bioremediation (Istok et al., 2004; Lovley et al., 1991; Wall and Krumholz, 2006), and *in situ* mineralization (Luo et al., 2009; Mehta et al., 2014, 2015; Rakovan et al., 2002). These methods prove effective for the reasons stated above; their ability to alter contaminant mobility by influencing their redox chemistry and sorption characteristics. Permeable reactive barriers are composed of reducing agents which are inserted into contaminated aquifers in order to immobilize actinides by reducing them to their insoluble solid phase. Bioremediation involves the injection of bacteria into contaminated sites to immobilize actinides via biological reduction. *In situ* mineralization, however, does not require actinide reduction for immobilization. Rather, fluids saturated with low solubility compounds (*i.e.* phosphate fluids) are injected into contaminated areas, thereby crystallizing actinide contaminants as stable minerals. This ability to harness redox and sorption reactions to immobilize actinide contaminants is what drives the research in the chapters to follow. Chapter 2 and 3 of this thesis investigate the potential oxidation state changes in naturally-occurring and synthetic uranyl peroxides; the mineral studtite $(UO_2)O_2(H_2O)_2{\cdot}(H_2O)_2$, and the uranyl nanocluster U_{60} $(Li_{40}K_{20}[UO_2(O_2)(OH)]_{60}(H_2O)_{214})$. Addressing the unknowns concerning stability, aqueous behavior, surface interactions, and redox characteristics of such radioactive compounds is essential in predicting their fate within the environment. Chapter 4 explores the immobilization of PuO_2^+ via *in situ* mineralization (specifically adsorption and incorporation) without a change in oxidation state. Identifying which specific minerals and mineral properties determine the degree of uptake of such contaminants is paramount to developing effective strategies for their sequestration within the environment.

Nuclear waste sites, reactor meltdowns, and uranium ore deposits have been known to form unique uranium molecules or secondary phases as a result of fission or radiolysis (Amme et al.,

2005; Arey et al., 1999; Burakov et al., 1997; Lazarevic and Spasojevic, 1978; Ticknor, 1994; Trueman et al., 2004; Wronkiewicz et al., 1992). One such secondary uranium product is uranyl peroxide, of which only one mineral is known to exist, studtite, the hydrate of metastudtite. Studtite is formed by incorporating peroxide produced via α-radiolysis of water and has been documented growing on uranium ores, nuclear waste casks, and even corium from the Chernobyl power plant meltdown in the Ukraine (Burakov et al., 1997; Walenta, 1974). In the molecular structure of studtite, uranyl ions are coordinated by two peroxide groups and two H_2O groups, resulting in a uranyl hexagonal bipyramid. The two of the equatorial edges defined by peroxide groups are shared between adjacent uranyl polyhedra, resulting in a chain structure. Adjacent chains are linked through pliable hydrogen bonds which allow for the uranyl-peroxide-uranyl dihedral angles to be bent at about 140°, giving the studtite structure a corrugated appearance (Sigmon et al., 2009). Sites capable of forming studtite are also known to create far more complex and largely uncharacterized structures (Armstrong et al., 2012; Burns et al., 2012; Di Lemma et al., 2015; Samsonov et al., 2014).

Since 2005, a myriad of nanoscale actinyl peroxide cage clusters have been synthetically produced, inspired by the extensive work on metal oxide clusters and the alternating bent dihedral bonds of studtite (Burns, 2005; Qiu and Burns, 2013; Sigmon et al., 2009). To date, 38 of these uranyl-based clusters and 1 neptunyl-based cluster have been published. The clusters range in size and molecular content from 20 actinide cations in a simple arrangement to as many as 120 actinide cations in a complex topology (Qiu and Burns, 2013). These unique clusters all contain actinyl ions bridged by peroxide ligands, and in a departure from studtite, all bent dihedral angles bend the same direction, *i.e.* about the center of the cluster, forming a closed cage. Such clusters have been theorized to self-assemble in specific conditions, such as the

addition of seawater to exposed U-Pu nuclear fuel rods during the Fukushima reactor accident (Armstrong et al., 2012; Burns et al., 2012). As with any newly-discovered compound, the synthesis of uranyl peroxide clusters and studtite, and their subsequent potential to exist in measurable quantities in natural systems underlines the need for investigations into the transport and properties of these unique structures.

The unknowns concerning these uranyl peroxide materials provide the basis for the primary research questions addressed in Chapter 2: 1.) Identify what redox transitions uranyl peroxide clusters undergo. 2.) Determine if clusters remain intact or break apart upon reduction. 3.) Develop standards and models to predict the redox behavior of this uncharacterized uranyl peroxide material and others like it. The findings from this chapter form the basis for the research questions in Chapter 3: 1.) Determine if the structural changes in U_{60} clusters can be measured *in situ* upon reduction. 2.) If spectroscopy be used to visualize and identify sorbates on substrate surfaces. Addressing the unknowns concerning uranyl peroxides in Chapter 2 and 3 produces information vital to their immobilization via reduction. Similarly, the research questions addressed in Chapter 4 include: 1.) Which host minerals can immobilize the most actinide contaminants and 2.) What mineral properties control the amount of contaminant uptake. Using pentavalent plutonyl (a less complex actinide than U_{60}), Chapter 4 provides key information concerning immobilization via *in situ* mineralization (co-precipitation) of a radioactive contaminant known to be highly mobile in aqueous environments, without a change in redox state.

1.2 Overview of Research Chapters

The research in this dissertation describes the use of a multi-method approach to understand the redox behavior and sorption processes that control the mobility of actinides U and Pu.

Electrochemical experiments, spectroscopic methods, surface probe techniques, and molecular simulations are used to identify reaction pathways and mechanisms affecting actinide mobility within natural systems and the function of mineral surfaces in the sequestration of both well-characterized and poorly-characterized actinide materials in underground waste repositories.

The electrochemical, thermodynamic, and kinetic behavior of uranyl peroxide nanoclusters (U_{60}) and their natural analog, the mineral studtite, is investigated in **Chapter 2**. This study was motivated by the discovery of the unusual uranyl peroxide nanostructures and their self-assembly and release in certain unique conditions (Armstrong et al., 2012; Burns, 2005; Burns et al., 2012). Although a range of uranyl peroxide nanoclusters (containing 20-120 actinide cations) have been described, the aqueous nature, solubility, stability, and redox properties of these clusters remains largely unknown, with the only published electrochemical study being the aqueous reduction of the relatively simple U_{28} cluster (Burns, 2011; Gil et al., 2012; Nyman and Burns, 2012; Qiu and Burns, 2013). The purpose of this research was to study the redox behavior, thermodynamics, and redox kinetics of uranyl peroxide materials (U_{60} and its naturally-occurring analog studtite) using cyclic voltammetry with powder microelectrodes. This chapter focuses primarily on the electrochemistry of the U(VI) reduction process, exploring the electrochemical properties, structure, and the effect that solution chemistry, pH, and scan rate have on the surface properties of U_{60} and studtite. Measuring the redox current as a function of redox potential using cyclic voltammetry, cyclic voltammograms (CVs) were established describing the behavior of U_{60} nanoclusters as solid-state mineral electrodes within a background electrolyte solution. This approach determined if redox reactions can occur, can be measured, and can be assigned to specific redox reactions as well as whether U_{60} clusters remain in the fullerene topology throughout experimentation or collapse upon reduction. Furthermore,

computational models determined if observed pH-shift was due to single or concurrent reactions, and estimated the magnitude and direction of electrode potential shift for the uncharacterized U_{60} complex. Given the importance of redox reactions in actinide minerals and spent nuclear fuels, such techniques represent an excellent tool for probing these processes.

Electrochemical studies of uranyl peroxides are continued in **Chapter 3**, with the introduction of scanning probe techniques to image the surface interaction and reduction of U_{60} directly. In this chapter, electrochemical atomic force microscopy (EC-AFM) is used to observe the adsorption, precipitation, and reduction of U_{60} *in situ,* as the mineral surface is electrochemically polarized. This methodology allows for *in situ* observations of reactions at a given Eh (as set using a potentiostat, avoiding the use of a pH buffer) and pH (as set by the solution chemistry), that can be mapped by an Eh-pH (Pourbaix) diagram. The Eh and pH act as master variables controlling speciation and thus the mobility and fate of uranyl peroxide materials in the environment. This technique has been used successfully in contaminant research to analyze epitaxial mineral growth, mineral dissolution, reaction kinetics, precipitation, adsorption, thin film formation, and electron transfer (Etienne et al., 2004; Higgins and Hamers, 1995, 1996; Higgins et al., 1996; Stack, 2008; Stack et al., 2004a; Stack et al., 2004b; Wigginton et al., 2009). This technique addresses the specific knowledge gaps concerning U_{60} nanocluster reductive immobilization. The purpose of this research is to determine the qualitative and quantitative behavior of U_{60} cluster reduction and adsorption onto crystalline surfaces at specific Eh and pH conditions. This morphological and kinetic information is combined with findings from surface-sensitive spectroscopic methods (SEM and AES) in order to view the resultant mineral surfaces with greater resolution *ex situ* and determine the composition and oxidation

state of adsorbates. These findings help to further our understanding of the behavior of uranyl peroxide clusters in environmental conditions.

In **Chapter 4**, actinide behavior is studied at an atomistic level, where the adsorption and incorporation of Pu into environmentally abundant mineral hosts can strongly influence the mobility and concentration of contaminants in both aqueous environments and the subsurface. The studies by Orlandini et al. (1986) and later by Choppin (2007) provide analytical evidence supporting that Pu(V) is the predominant form of oxidized plutonium in natural waters. This chapter investigates the feasibility of removing mobile Pu(V) contaminants from an aqueous system into different host minerals by evaluating the thermodynamics of incorporation using computational models of surface and bulk incorporation reactions with carbonate and sulfate minerals. *Ab initio* methods are applied to probe the mechanisms and energetics of atomistic- and nano-scale processes at the mineral-water interface that could influence the sorption and stability of Pu on mineral surfaces. Should such incorporation prove favorable, requiring only a small amount of energy input, these findings would aid sequestration efforts concerning mobile actinide contaminants. The approach developed in this chapter is an extension of the existing method of quantum-mechanical treatment of the incorporation of aqueous species into a mineral, including the thermodynamics of each of these intermediate steps. This allows for further investigation of the kinetics of a rate-controlling substep, paving the way for a complete kinetic analysis of each substep of the reaction (*i.e.*, adsorption, incorporation into the topmost surface layer, incorporation into the bulk).

1.3 Advantages and Complementarity of the Multi-method Approach

The mobility and sequestration of actinides within the environment depends on a large number of variables and processes including contaminant structure, surface interactions,

thermodynamics, kinetics, and redox reactions. Electrochemical techniques are ideal for such analysis giving both qualitative and quantitative measurement of surface behavior and redox characteristics. Atomic-scale measurements of actinide mobility can be addressed through a combination of electrochemical methods with spectroscopic, surface probe, or computational techniques. This combination represents a logical approach to study a complex process that has been utilized by a number of published investigations (Conway, 1995; Gao et al., 2011; Greeley et al., 2006; Hrapovic et al., 2004; Zhang et al., 2010).

The advantage of an electrochemical approach is that the redox potential close to the surface of the mineral electrode can be changed rapidly by varying the potential on the electrode, and therefore the mineral surface that is in contact with the electrode, sweeping through a range of potentials. Solid-state redox reactions occur at the solid/electrolyte interface and give rise to voltammetric responses (peaks) indicating electron transfer and ion transport that mark the redox transformation of the actinide solids (Mallon et al., 2012; Nicholson, 1965). The observed oxidation/reduction potential gives information about the thermodynamics (peak position) and kinetics (peak height) of electron transfer processes as a function of pH, solution chemistry, and electrode material (studtite, clusters in solids, or mineral surfaces with clusters in solution or adsorbed).

By combining electrochemistry with a surface probe technique like AFM, one can visualize the sorption, kinetics, and reduction of actinides *in situ* on relevant environmental surfaces (minerals and metals). Adsorption behavior and kinetic information are measured via growth of adsorbates over time and the number of adsorbates or adsorbate coverage per unit area in relation to time. Eh-pH diagrams are used to help identify the species present at particular pH and Eh

values. Through AFM imaging, we are able to discern growth features over time (volume, symmetry, height, growth face, etc.) and make predictions as to the reaction process observed.

Electrochemical means can produce and measure the actinide reaction products, precipitates, and sorbates, and AFM can visualize their surface formation *in situ*. However the redox state, structure, and composition of these products remain unclear. Thus, the use of spectroscopic methods such as scanning electron microscopy (SEM), auger electron spectroscopy (AES), and synchrotron x-ray absorption spectroscopy (XAS) are necessary to characterize the actinide materials sorbed to mineral surfaces. SEM can provide high-resolution structural information and with the attached energy dispersive x-ray spectroscopy (EDX), can supply compositional analysis. AES, a surface-sensitive technique ideal for adsorbate analysis, can provide structural, composition, and oxidation state information. XAS using synchrotron radiation is a powerful determinative method that can be used to verify the composition and oxidation state of reduction products, cluster and mineral structural integrity, as well as to obtain quantitative measures of U(V) and U(IV) phase products.

Quantum-mechanical models of such interactions can give complimentary insight into processes not visible to surface probe or spectroscopic techniques such as the atomistic mechanisms, energetics, stability, affected sites, adsorption state prior to incorporation, and an approximation of the reaction sequence. Computational approaches also provide a method of rapidly testing interactions of actinides upon a range of mineral surfaces in order to identify those most promising for experimental analysis. Additionally, molecular models offer approximations utilizing the total nuclear and electronic energy of actinide complexes to predict their behavior in solutions or electrochemical experiments.

This dissertation furthers the understanding of both natural and synthetic actinide materials (U and Pu) and their mobility and redox behavior as potential contaminants in the environment. Utilizing a combined approach of electrochemical experiments coupled with surface probe, spectroscopic, and computational techniques, the three following (research) chapters describe how actinide species in environmental conditions interact with mineral surfaces and surface-mediated redox processes. Such information is essential to any experiment concerning sorption, precipitation, diffusion, incorporation, surface complexation, and solid solution formation. Such experiments have immediate applications regarding the understanding and cleanup of sites contaminated with actinide materials.

Three publications are expected from this thesis work as shown below. The three papers have been revised based on the comments made by the committee members and are the three main research chapters of this thesis.

- *Electrochemical Analysis of the Kinetics of Oxidation/Reduction Reactions of the Peroxide-Containing Mineral Studtite in Comparison to Uranyl Peroxide Clusters (U_{60})*
- *Surface-Mediated Reactions of Uranyl Peroxide Materials U_{60} and Studtite at the Mineral-Electrolyte Interface*
- *Quantum-Mechanical Determination of the Incorporation of Pentavalent Plutonium into Carbonate and Sulfate Minerals*

Awards and Funding for the research in this dissertation are listed below.

Department of Energy Basic Energy Sciences Grant	2012 – Present
Department of Energy SCGSR Project Fellowship (Argonne National Lab)	Feb. 2015
Scott Turner Research Grant in Earth Science (University of Michigan)	Apr. 2016
Scott Turner Research Grant in Earth Science	Apr. 2015

(University of Michigan)

Scott Turner Research Grant in Earth Science — Apr. 2014
(University of Michigan)

Goldschmidt Conference Grant — July 2016
(NASA)

Goldschmidt Conference Grant — July 2015
(NASA)

Rackham Graduate Travel Grant — July 2015
(University of Michigan)

Rackham Research Grant — July 2015
(University of Michigan)

Transformational Technologies in Molecular Simulation Grant — Sept. 2014
(University of Wisconsin)

1.4 Works Cited

Amme, M., Wiss, T., Thiele, H., Boulet, P. and Lang, H. (2005) Uranium secondary phase formation during anoxic hydrothermal leaching processes of UO_2 nuclear fuel. *J. Nucl. Mater.* **341**, 209-223.

Arey, J.S., Seaman, J.C. and Bertsch, P.M. (1999) Immobilization of uranium in contaminated sediments by hydroxyapatite addition. *Environmental Science & Technology* **33**, 337-342.

Armstrong, C.R., Nyman, M., Shvareva, T., Sigmon, G.E., Burns, P.C. and Navrotsky, A. (2012) Uranyl peroxide enhanced nuclear fuel corrosion in seawater. *Proceedings of the National Academy of Sciences of the United States of America* **109**, 1874-1877.

Arnold, P.L., Love, J.B. and Patel, D. (2009) Pentavalent uranyl complexes. *Coord. Chem. Rev.* **253**, 1973-1978.

Bodvarsson, G.S., Boyle, W., Patterson, R. and Williams, D. (1999) Overview of scientific investigations at Yucca Mountain - the potential repository for high-level nuclear waste. *J. Contam. Hydrol.* **38**, 3-24.

Brown, G.E. and Calas, G. (2012) Mineral-aqueous solution interfaces and their impact on the environment. *Geochem Perspect* **1**, 483-742.

Bruno, J. and Ewing, R.C. (2006) Spent nuclear fuel. *Elements* **2**, 343-349.

Burakov, B.E., Strykanova, E.E. and Anderson, E.B. (1997) Secondary uranium minerals on the surface of Chernobyl "lava", in: Gray, W.J., Triay, I.R. (Eds.), Scientific Basis for Nuclear Waste Management Xx, pp. 1309-1311.

Burns, P.C. (2005) U^{6+} minerals and inorganic compounds: Insights into an expanded structural hierarchy of crystal structures. *Can. Mineral.* **43**, 1839-1894.

Burns, P.C. (2011) Nanoscale uranium-based cage clusters inspired by uranium mineralogy. *Mineralogical Magazine* **75**, 1-25.

Burns, P.C., Ewing, R.C. and Navrotsky, A. (2012) Nuclear fuel in a reactor accident. *Science* **335**, 1184-1188.

Burns, P.C. and Finch, R. (1999) Uranium : mineralogy, geochemistry and the environment. Mineralogical Society of America, Washington, DC.

Choppin, G.R. (2007) Actinide speciation in the environment. *J. Radioanal. Nucl. Chem.* **273**, 695-703.

Conway, B.E. (1995) Electrochemical oxide film formation at noble-metals as a surface-chemical process. *Prog. Surf. Sci.* **49**, 331-452.

Delay, J., Lesavre, A. and Wileveau, Y. (2008) The French underground research laboratory in Bure as a precursor for deep geological repositories, in: Rempe, N.T. (Ed.), Deep Geologic Repositories, pp. 97-111.

Di Lemma, F.G., Colle, J.Y., Rasmussen, G. and Konings, R.J.M. (2015) Fission product partitioning in aerosol release from simulated spent nuclear fuel. *J. Nucl. Mater.* **465**, 127-134.

EPA (2012) Cleaning up radioactive sites.

Etienne, M., Schulte, A., Mann, S., Jordan, G., Dietzel, L.D. and Schuhmann, W. (2004) Constant-distance mode scanning potentiometry. 1. Visualization of calcium carbonate dissolution in aqueous solution. *Anal. Chem.* **76**, 3682-3688.

Ewing, R.C. (2015) Long-term storage of spent nuclear fuel. *Nat Mater* **14**, 252-257.

Ewing, R.C. and Macfarlane, A. (2002) Nuclear waste - Yucca Mountain. *Science* **296**, 659-660.

Gao, J., Lowe, M.A., Kiya, Y. and Abruna, H.D. (2011) Effects of liquid electrolytes on the charge-discharge performance of rechargeable lithium/sulfur batteries: Electrochemical and in-situ x-ray absorption spectroscopic studies. *Journal of Physical Chemistry C* **115**, 25132-25137.

Gaucher, E., Robelin, C., Matray, J.M., Negral, G., Gros, Y., Heitz, J.F., Vinsot, A., Rebours, H., Cassagnabere, A. and Bouchet, A. (2004) ANDRA underground research laboratory: interpretation of the mineralogical and geochemical data acquired in the Callovian-Oxfordian formation by investigative drilling. *Physics and Chemistry of the Earth* **29**, 55-77.

Geckeis, H., Lutzenkirchen, J., Polly, R., Rabung, T. and Schmidt, M. (2013) Mineral-water interface reactions of actinides. *Chem. Rev.* **113**, 1016-1062.

Gil, A., Karhanek, D., Miro, P., Antonio, M.R., Nyman, M. and Bo, C. (2012) A journey inside the U_{28} nanocapsule. *Chemistry-a European Journal* **18**, 8340-8346.

Greeley, J., Jaramillo, T.F., Bonde, J., Chorkendorff, I.B. and Norskov, J.K. (2006) Computational high-throughput screening of electrocatalytic materials for hydrogen evolution. *Nat Mater* **5**, 909-913.

Gu, B., Liang, L., Dickey, M.J., Yin, X. and Dai, S. (1998) Reductive precipitation of uranium(VI) by zero-valent iron. *Environmental Science & Technology* **32**, 3366-3373.

Higgins, S.R. and Hamers, R.J. (1995) Spatially-resolved electrochemistry of the lead sulfide (galena) (001) surface by electrochemical scanning-tunneling-microscopy. *Surf. Sci.* **324**, 263-281.

Higgins, S.R. and Hamers, R.J. (1996) Chemical dissolution of the galena (001) surface observed using electrochemical scanning tunneling microscopy. *Geochim. Cosmochim. Acta* **60**, 3067-3073.

Higgins, S.R., Hamers, R.J. and Banfield, J.F. (1996) In-situ real-time imaging of the surface reactions of metal sulfide minerals with electrochemical STM. *Abstr Pap Am Chem S* **211**, 70-COLL.

Hrapovic, S., Liu, Y.L., Male, K.B. and Luong, J.H.T. (2004) Electrochemical biosensing platforms using platinum nanoparticles and carbon nanotubes. *Anal. Chem.* **76**, 1083-1088.

Istok, J.D., Senko, J.M., Krumholz, L.R., Watson, D., Bogle, M.A., Peacock, A., Chang, Y.J. and White, D.C. (2004) In situ bioreduction of technetium and uranium in a nitrate-contaminated aquifer. *Environmental Science & Technology* **38**, 468-475.

Kim, J.I. and Grambow, B. (1999) Geochemical assessment of actinide isolation in a German salt repository environment. *Eng Geol* **52**, 221-230.

Lazarevic, D. and Spasojevic, D. (1978) Dynamic equilibrium-model of secondary phases in uranium during irradiation. *J. Nucl. Mater.* **69-7**, 832-834.

Long, J.C.S. and Ewing, R.C. (2004) Yucca Mountain: Earth-science issues at a geologic repository for high-level nuclear waste. *Annual Review of Earth and Planetary Sciences* **32**, 363-401.

Lovley, D.R., Phillips, E.J.P., Gorby, Y.A. and Landa, E.R. (1991) Microbial reduction of uranium. *Nature* **350**, 413-416.

Luo, Y., Hughes, J.M., Rakovan, J. and Pan, Y.M. (2009) Site preference of U and Th in Cl, F, and Sr apatites. *Am. Mineral.* **94**, 345-351.

Maher, K., Bargar, J.R. and Brown, G.E. (2013) Environmental speciation of actinides. *Inorg. Chem.* **52**, 3510-3532.

Mallon, C., Walshe, A., Forster, R.J., Keyes, T.E. and Baker, R.J. (2012) Physical characterization and reactivity of the uranyl peroxide $UO_2(\eta^2\text{-}O_2)(H_2O)_2 \cdot 2H_2O$: Implications for storage of spent nuclear fuels. *Inorg. Chem.* **51**, 8509-8515.

Mehta, V.S., Maillot, F., Wang, Z.M., Catalano, J.G. and Giammar, D.E. (2014) Effect of co-solutes on the products and solubility of uranium(VI) precipitated with phosphate. *Chem. Geol.* **364**, 66-75.

Mehta, V.S., Maillot, F., Wang, Z.M., Catalano, J.G. and Giammar, D.E. (2015) Transport of U(VI) through sediments amended with phosphate to induce in situ uranium immobilization. *Water Res.* **69**, 307-317.

Morrison, S.J., Metzler, D.R. and Carpenter, C.E. (2001) Uranium precipitation in a permeable reactive barrier by progressive irreversible dissolution of zerovalent iron. *Environmental Science & Technology* **35**, 385-390.

Nicholson, R.S. (1965) Theory and application of cyclic voltammetry for measurement of electrode reaction kinetics. *Anal. Chem.* **37**, 1351+.

Nyman, M. and Burns, P.C. (2012) A comprehensive comparison of transition-metal and actinyl polyoxometalates. *Chem. Soc. Rev.* **41**, 7354-7367.

Orlandini, K.A., Penrose, W.R. and Nelson, D.M. (1986) Pu(V) as the stable form of oxidized plutonium in natural-waters. *Mar. Chem.* **18**, 49-57.

Poinssot, C. and Geckeis, H. (2012) Radionuclide behaviour in the natural environment : science, implications and lessons for the nuclear industry. Woodhead Publishing, Cambridge, UK ; Philadelphia, PA.

Powell, B.A. (2012) Environmental chemistry of uranium and plutonium. *Actinide Chemistry Series*.

Qiu, J. and Burns, P.C. (2013) Clusters of actinides with oxide, peroxide, or hydroxide bridges. *Chem. Rev.* **113**, 1097-1120.

Rakovan, J., Reeder, R.J., Elzinga, E.J., Cherniak, D.J., Tait, C.D. and Morris, D.E. (2002) Structural characterization of U(VI) in apatite by x-ray absorption spectroscopy. *Environmental Science & Technology* **36**, 3114-3117.

Renock, D., Mueller, M., Yuan, K., Ewing, R.C. and Becker, U. (2013) The energetics and kinetics of uranyl reduction on pyrite, hematite, and magnetite surfaces: A powder microelectrode study. *Geochim. Cosmochim. Acta* **118**, 56-71.

Roberts, K.E., Wolery, T.J., Atkins-Duffin, C.E., Prussin, T.G., Allen, P.G., Bucher, J.J., Shuh, D.K., Finch, R.J. and Prussin, S.G. (2003) Precipitation of crystalline neptunium dioxide from near-neutral aqueous solution. *Radiochimica Acta* **91**, 87-92.

Samsonov, M.D., Trofimov, T.I., Kulyako, Y.M., Vinokurov, S.E. and Myasoedov, B.F. (2014) The behavior of uranium and fission products in the processing of model spent nuclear fuel in iron(III) nitrate solutions in the presence of supercritical tributyl phosphate-containing carbon dioxide. *Russian Journal of Physical Chemistry B* **8**, 1033-1037.

Schène, R. (2007) Nuclear Fuel Cycle. European Nuclear Society.

Sigmon, G.E., Ling, J., Unruh, D.K., Moore-Shay, L., Ward, M., Weaver, B. and Burns, P.C. (2009) Uranyl-peroxide interactions favor nanocluster self-assembly. *J. Am. Chem. Soc.* **131**, 16648.

Stack, A.G. (2008) Applications of electrochemical scanning tunneling microscopy to adsorption and thin films in geochemical systems. *Abstr Pap Am Chem S* **235**.

Stack, A.G., Eggleston, C.M. and Engelhard, M.H. (2004a) Reaction of hydroquinone with hematite I. Study of adsorption by electrochemical-scanning tunneling microscopy and x-ray photoelectron spectroscopy. *J. Colloid Interface Sci.* **274**, 433-441.

Stack, A.G., Erni, R., Browning, N.D. and Casey, W.H. (2004b) Pyromorphite growth on lead-sulfide surfaces. *Environmental Science & Technology* **38**, 5529-5534.

Ticknor, K.V. (1994) Uranium sorption on geological-materials. *Radiochimica Acta* **64**, 229-236.

Timm, C. and Fox, J. (2011) Could WIPP replace Yucca Mountain? *Nuclear Engineering International* **56**, 22-25.

Trueman, E.R., Black, S., Read, D. and Hodson, M.E. (2004) Secondary phase formation on depleted uranium metal in soil. *Geochim. Cosmochim. Acta* **68**, A498-A498.

Walenta, K. (1974) Studtite and its composition. *Am. Mineral.* **59**, 166-171.

Wall, J.D. and Krumholz, L.R. (2006) Uranium reduction, Annual Review of Microbiology, pp. 149-166.

Wigginton, N.S., Rosso, K.M., Stack, A.G. and Hochella, M.F. (2009) Long-range electron transfer across cytochrome-hematite (αFe_2O_3) interfaces. *Journal of Physical Chemistry C* **113**, 2096-2103.

Wronkiewicz, D.J., Bates, J.K., Gerding, T.J., Veleckis, E. and Tani, B.S. (1992) Uranium release and secondary phase formation during unsaturated testing of UO_2 at 90°C. *J. Nucl. Mater.* **190**, 107-127.

Yuan, K., Ilton, E.S., Antonio, M.R., Li, Z.R., Cook, P.J. and Becker, U. (2015a) Electrochemical and spectroscopic evidence on the one-electron reduction of U(VI) to U(V) on magnetite. *Environmental Science & Technology* **49**, 6206-6213.

Yuan, K., Renock, D., Ewing, R.C. and Becker, U. (2015b) Uranium reduction on magnetite: Probing for pentavalent uranium using electrochemical methods. *Geochim. Cosmochim. Acta* **156**, 194-206.

Zhang, K., Zhang, L.L., Zhao, X.S. and Wu, J.S. (2010) Graphene/polyaniline nanofiber composites as supercapacitor electrodes. *Chem. Mater.* **22**, 1392-1401.

CHAPTER 2

Electrochemical Analysis of the Kinetics of Oxidation/Reduction Reactions of the Peroxide-Containing Mineral Studtite in Comparison to Uranyl Peroxide Clusters (U_{60})

- Ben Gebarski and Udo Becker -

Department of Earth and Environmental Sciences, University of Michigan, 2534 C.C. Little Building, 1100 North University Avenue, Ann Arbor, MI 48109-1005, USA

2.1 Abstract

An electrochemical analysis of U_{60} nanoclusters ($Li_{40}K_{20}[UO_2(O_2)(OH)]_{60}(H_2O)_{214}$) and their natural analog, the mineral studtite $(UO_2)O_2(H_2O)_2 \cdot (H_2O)_2$, was carried out using cyclic voltammetry with a powder microelectrode (PME) setup. The purpose of this research is to study the redox behavior, thermodynamics, and redox kinetics of uranyl peroxide materials in order to better understand their behavior and mobility in the environment.

U_{60} voltammograms exhibit coupled reduction peaks assigned to the U(VI)/U(V) transition at +239 mV (vs. SHE) indicative of a shift from UO_2^{2+} to UO_2^{+} consistent with published standard electrode potentials. The U(V)/U(IV) transition at -54 mV is assigned to the shift from $UO_2^{+}/U(OH)_4$. A model was created using all possible U(IV) species at the experimental conditions ($UO_{2(s)}$, $U^{4+}_{(aq)}$, $U(OH)^{3+}_{(aq)}$, $U(OH)_2^{2+}{}_{(aq)}$, $U(OH)_3^{+}{}_{(aq)}$, $U(OH)_{4(aq)}$, and $U(OH)_5^{-}{}_{(aq)}$) to describe this pH-dependent transition. The slight pH dependence (which diminishes at higher pH) is correlated with the dominant U(IV) species present in aqueous solution at each pH, with a $UO_2^{+}/U(OH)_3^{+}$ transition at acidic pH and a $UO_2^{+}/U(OH)_5^{-}$ transition at more basic pH.

A novel method for adjustment of published standard electrode potentials (typically derived from calorimetric data at pH 0) to environmentally-relevant conditions (pH 3-9) is proposed using the observed pH shift in conjunction with computational models of speciation in aqueous conditions. This methodology proves effective in predicting peak position as a function of pH and solution chemistry when compared with experimental observations.

The electrochemical behavior of isolated U_{60} nanoclusters was studied in order to determine if the redox transitions observed occur inside or outside the cluster and if clusters are destroyed upon reduction. Aqueous suspensions of U_{60} clusters (undersaturated with respect to nanoclusters) have been shown to dissolve or dissociate to yield aqueous monomeric U^{6+}, Li^{+}, and K^{+} species (Flynn et al., 2015). Thus it is possible that all observed electrochemical signal comes from dissolved U_{60}. However, such suspensions have also been shown to reach equilibrium between aqueous U_{60} and its dissolution products rapidly after the hydration of isolated U_{60} clusters, suggesting the presence of both U_{60} and aqueous monomeric species in our electrochemical results. Furthermore, agreement between observed pH-dependence of electrochemical data and calculated models is best when considering part of the signal from within isolated U_{60} clusters and part from outside U_{60} as monomeric aqueous species.

Voltammetry indicates an irreversible reduction of U(VI) to U(V) and a quasi-reversible reduction of U(V) to U(IV). Peroxide (O_2^{2-}) linkers within U_{60} are reduced irreversibly to OH^{-} and oxidized to O_2 through the formation of a quasi-reversible superoxo (O_2^{-}) complex with U(V). Results suggest that the U_{60} cluster is likely broken apart at the peroxo sites, forming $UO_{2(s)}$ after repeated cycling.

2.2 Introduction

The electrochemical nature of the unique uranium-60 nanocluster (U_{60}), a closed cluster of uranyl polyhedra, has yet to be characterized since its synthesis in 2005 (Burns et al., 2005; Sigmon et al., 2009a). U_{60} nanoclusters ($Li_{40}K_{20}[UO_2(O_2)(OH)]_{60}(H_2O)_{214}$) consist of a network of U atoms adopting the same topology as C_{60} Buckminster fullerenes ("buckyballs") and certain polyoxometalate clusters (see Appendix A). They contain 60 linear $(UO_2)^{2+}$ uranyl ion units with the two uranyl O atoms pointing radially towards and away from the center of the cluster with peroxide bonds connecting two adjacent uranium atoms along the surface of the buckyball (Kong et al., 2010; Ling et al., 2010). The uranyl ions on the surface of such clusters form pentagonal (much like the black patches on a traditional soccer ball) and hexagonal (the white patches) rings. Two-thirds of the rings are hexagonal with peroxide groups at the "seam" between two hexagons; the remaining third of the rings are pentagonal and the "seam" between a hexagon and pentagon is formed by two hydroxyl groups. The U-O_2-U dihedral angles are bent the same way, *i.e.,* about the center of the cluster. This topology results in clusters built entirely from uranyl hexagonal bipyramids, each connected to three others, containing 60 U atoms with a total mass of 19,891 u, roughly 83 times greater than that of a single uranium atom (Flynn et al., 2015). Computational quantum-chemical studies on U_{60} and smaller such clusters report bonding characterized by an overlap of U 6p orbitals with peroxy π-bonds, while the 6d and 5f orbitals are bonded with the oxo ligand (–yl oxygen) in the U(VI) ion (Burns, 2011; Gagliardi et al., 2013; Vlaisavljevich et al., 2010).

Peroxide bonds connecting metal cations are only observed in one naturally-occurring mineral, studtite, $(UO_2)O_2(H_2O)_2{\cdot}2(H_2O)$, the hydrate of metastudtite, $(UO_2)O_2(H_2O)_2$, found primarily as a phase alteration product in the presence of uranium, either in mines or nuclear

waste repositories. The peroxide is formed via the α-radiolysis of water during formation (Hixon et al., 2013; Ling et al., 2012; Mallon et al., 2012; Sigmon et al., 2009a). In this uranyl peroxide mineral, the U-O_2-U dihedral angles are bent back and forth, resulting in a corrugated periodic arrangement of uranyl building blocks. Computational investigations into the structure and bonding of studtite demonstrate that the bent peroxide bonds are essential to the self-assembly of large uranyl peroxide cage clusters like U_{60} (Gagliardi et al., 2013; Vlaisavljevich et al., 2010).

U_{60} has been shown to self-assemble in aqueous solution under ambient conditions and form crystals composed of nanocluster building blocks in a crystalline face-centered-cubic (FCC) configuration (Sigmon et al., 2009b). A range of uranyl peroxide nanocluster materials and crystals have been described, but the aqueous nature, solubility, stability, and behavior of these clusters remains largely unknown (Burns, 2011; Nyman and Burns, 2012; Qiu and Burns, 2013). Crystals of uranyl peroxide nanoclusters are in general highly soluble, the crystalline structure dissolving completely when placed in undersaturated solutions, leaving only isolated nanoclusters in solution (Qiu and Burns, 2013). These U_{60} clusters can remain in solution for several months or more before the cluster begins to dissociate or dissolve (Armstrong et al., 2012; Flynn et al., 2015).

Basic energy research into actinides and the storage of spent nuclear fuels is of particular concern for all institutions that use nuclear power to generate electricity. Under geological repository conditions such as those of the U.S. Yucca Mountain waste repository, specifically those in oxidizing conditions, the oxidation of U(IV) to U(VI) is thermodynamically favorable (Lutze and Ewing, 1988). Such conditions are favorable to the generation of phase alteration products like studtite (Burns et al., 1997; Hixon et al., 2013; Springell et al., 2015). In aqueous environments, such as the hydrated aquitard formations of the French ANDRA Bure waste

repository, the soluble (and highly mobile) U(VI) phases can be reduced to (typically metastable) U(V) and subsequently to a relatively insoluble U(IV). The redox state of uranium has a direct correlation with its solubility in aqueous conditions and therefore its overall mobility within the environment. As U(VI) is reduced to U(IV), its solubility decreases (along with its mobility) within an aqueous system (Arumugam and Becker, 2014; Becker et al., 2012; Finch and Ewing, 1992; Lutze and Ewing, 1988; Murakami et al., 1997; Shuller et al., 2011; Xu et al., 2002; Yuan et al., 2015b). The synthesis of U_{60} and its natural analog studtite, their high solubility, and their subsequent potential to exist in measurable quantities in natural systems underlines the need for investigations into the transport and properties of these unique structures. The electrochemical behavior of U_{60} nanoclusters is of particular interest due to their ability to self-assemble in certain unique conditions, such as the addition of seawater to exposed U-Pu nuclear fuel rods during the Fukushima reactor accident (Armstrong et al., 2012; Burns et al., 2012).

To study the electrochemical behavior of these uranyl peroxides, powder microelectrode (also known as cavity microelectrode) electroanalysis was conducted. Advantages the powder microelectrode (PME) include the use of only microgram amounts of powdered sample that is easily loaded into the electrode cavity, allowing for the electrochemical analysis of solids in direct contact with the electrode surface (see Section 2.3). The powder microelectrode was chosen because it provides easier sample preparation, higher speed of cycling, improved reversibility, high sample surface-area to volume ratio, and lack of sample surface damage when compared with conventional inert metal electrodes (Cha et al., 1994; Li and Cha, 1988; Locatelli et al., 2011; Renock et al., 2013; Vivier et al., 1999).

In electrochemical experiments, the applied potential on the electrode can be controlled precisely, making specific redox conditions feasible to achieve. In most electrochemical

methods, the redox reaction rate is driven by the applied potential across the electrode/sample/solution interface. The flow of electrons in and out of the electrode interface is interpreted as current (I) and the redox behavior can be assessed based on the relationship between current and potential (Bard and Faulkner, 2001). Solid-state redox reactions occur at the solid/electrolyte interface giving rise to voltammetric responses indicating electron transfer and ion transport that mark the redox transformation of the solid (Mallon et al., 2012; Nicholson, 1965).

The purpose of this research is to study the redox behavior, thermodynamics, and redox kinetics of uranyl peroxide materials (U_{60} and its naturally-occurring analog studtite) using cyclic voltammetry with powder microelectrodes. This study investigates the electrochemical properties, structure, and the effect of solution chemistry, pH, and scan rate on the surface properties of U_{60} and studtite, by obtaining cyclic voltammograms measuring the redox current as a function of redox potential. Conclusions based on the respective oxidation/reduction potential can be drawn about the thermodynamics (peak position) and kinetics (peak height) of electron transfer processes as a function of pH, solution chemistry, and electrode material (studtite, clusters in solids, or mineral surfaces with clusters in solution or adsorbed). Further interpretation of results seeks to determine if redox reactions can occur, can be measured, and can be assigned to specific redox reactions as well as whether U_{60} clusters remain in the fullerene topology throughout experimentation or collapse upon reduction and oxidation. Furthermore, computational models are used to determine if observed pH-shift is due to single or concurrent reactions, and to estimate the magnitude and direction of electrode potential shift for the U_{60} complex. Given the potential importance of redox reactions in actinide minerals and spent

nuclear fuels, electrochemical techniques in tandem with computational modeling represent an excellent tool for probing these processes.

2.3 Materials and Methods

U_{60} nanoclusters and studtite were prepared according to the literature (Debets, 1963; Mallon et al., 2012; Sigmon et al., 2009b) and crystallized from solution. Natural U^{238} was used in preparation of these samples and throughout the course of this project. U^{238} is an α-emitter and all experiments were carried out in laboratories designed for the use of radioactive materials. All other reagents were obtained from professional commercial sources.

2.3.1 Synthesis of U Solids and Solutions

The synthesis of the solids and solutions used are as follows: U_{60} clusters ($Li_{40}K_{20}[UO_2(O_2)(OH)]_{60}(H_2O)_{214}$) are prepared by combining 1 ml aqueous solutions of uranyl nitrate hexahydrate 0.5 M ($UO_2(NO_3)_2{\cdot}6H_2O$) (International Bio-Analytical Industries, Inc. maximum activity: 4.02×10^{-2} μCi), 1 ml of 30% hydrogen peroxide (H_2O_2, Fisher Scientific), and 0.1 ml potassium chloride (0.40 M KCl, Fisher Scientific). The pH of this solution is adjusted to 9 by adding 0.40 ml of LiOH (4.0 M, Fisher Scientific). The solution is left to nucleate for seven days, when visible, yellow, cubic U_{60} crystals develop (Burns, 2005; Flynn et al., 2015). Clusters are separated from mother solution via vacuum filtration and washed with Milli-Q ultrapure H_2O. Identity and purity of crystals is verified using Raman spectroscopy (Jegou et al., 2015; Stefanovsky et al., 2014; Wylie et al., 2014).

Studtite [$(UO_2)O_2(H_2O)_2{\cdot}(H_2O)_2$] ("·" indicating the water molecules of crystallization - two water molecules not bound directly to UO_2) is synthesized by combining solutions of 1 ml of 0.5 M uranyl nitrate hexahydrate ($UO_2(NO_3)_2{\cdot}6H_2O$), International Bio-Analytical Industries, Inc., maximum activity: 4.02×10^{-2} μCi, and 1 ml of 30% hydrogen peroxide (H_2O_2, Fisher

Scientific). The solution is left exposed to air for seven days, when fine, fibrous, yellow studtite crystals form (Burns, 2005; Sigmon et al., 2009b).

2.3.2 Powder Microanalysis

Microgram quantities of dry U_{60} were packed into the powder microelectrode (PME), which consists of a microcavity of about 35 μm depth and 100 μm in diameter, embedded in the tip of a glass capillary. The PME contains a platinum wire sealed in a soda-lime glass tube which has been cut, polished, and then put in *aqua regia* in order to etch away part of the platinum wire and form a cavity. The dimensions of the cavity are determined by the diameter of the Pt wire (cavity width) and the length of Pt etched away in the acid bath (cavity depth). The depth of the cavity is approximated by etching time elapsed in a temperature-controlled *aqua regia* bath of about 70-80 ºC that is renewed every 30 minutes. The standard formula of 14 μm/hr etching speed at these conditions was applied, and a bath exposure time of 2.5 hours results in a cavity depth of ~35 μm. Etching depth was verified using optical microscopy (Cachet-Vivier et al., 2001; Cha et al., 1994; Renock et al., 2013; Yuan et al., 2015b). A small amount of sample, approximated by the volume of the cavity ($2.75 \cdot 10^{5}$ μm^3, $2.75 \cdot 10^{-4}$ mm^3), makes electrical contact with the electrode platinum wire when packed (sample inserted into the PME cavity). Packing is a robust process, as samples are set upon a glass slide backing and are forced into the cavity by firmly pressing the empty powder microelectrode upon it. Experiments show that samples remain packed indefinitely when stored as such and endure for hours when immersed in Milli-Q ultrapure water (see Appendix C). After each experiment, samples are removed via sonication using three different cleaning solutions for about 15 seconds each. First, a packed microelectrode is sonicated in Milli-Q water, then 0.01 M HNO_3 (Fisher Scientific), and finally in ethanol. The electrode and cavity are then fully dried with compressed air before packing with new sample.

2.3.3 Electrochemistry Experiments

A potentiostat/galvanostat (EG&G Instruments Princeton Applied Research Model 263A) with computer output using the *PowerSuite* software package was used for voltammetry. Scan rates and voltage ranges were adjusted using the *PowerSuite* software. Voltage was applied to the working electrode with respect to the reference electrode and current passing through the working electrode and counter electrode was measured. Results were displayed by *PowerSuite* software and graphical representations were produced by *OriginLab* software. The packed powder microelectrode serves as the working electrode, and was inserted into standard Pyrex three-electrode electrochemical cells with platinum-mesh counter electrodes and a CH Instruments Ag/AgCl (saturated KCl) reference electrode (+0.197 V vs. SHE). Solutions were sparged with argon gas for ~30 minutes prior to inserting the PME and then continuously throughout the experiment. This bubbling of the solution with an ultrapure dry inert gas before measurement removes dissolved oxygen, a strong oxidizing agent. Cyclic voltammetry experiments were started from the open circuit potential (OCP, *i.e.*, working electrode equilibrium potential) and scanned from negative to positive potentials at a scan rate of 50 mV/s (unless otherwise stated) until the redox switching potential was reached. Each potential scan was repeated for 5-20 cycles. All voltammograms are plotted with positive current for the anodic scan and negative current for the cathodic scan.

Solutions were prepared using Milli-Q ultrapure H_2O and pH was adjusted using 0.1 M H_2SO_4 (Fisher Scientific) and 0.1 M Na_2SO_4 (Fisher Scientific) solutions. Values for pH of solutions were provided by a ThermoScientific Orion Star 111A pH meter with pH probe. Uranium solutions contained 0.025 M uranyl nitrate hexahydrate ($UO_2(NO_3)_2 \cdot 6H_2O$) (International Bio-Analytical Industries, Inc.) unless otherwise stated.

Voltammograms are annotated with anodic (A) and cathodic (C) to distinguish peaks. *OriginLab* software was used to calculate and plot peak area and current, defining peaks using CV inflection points or a Savitzky-Golay smoothing function for 1st and 2nd derivatives for local maxima and minima (Savitzky and Golay, 1964). Midpoint potential (E_{mid}) of the anodic (E_A) and cathodic (E_C) peaks were calculated as $E_{mid} = \frac{1}{2}(E_A + E_C)$. All potentials in this study are displayed with respect to the Standard Hydrogen Electrode (SHE).

2.3.4 Aqueous Geochemical Modeling

Aqueous Solutions LLC Geochemist's Workbench Rxn program was used to calculate thermodynamic data and the concentration of chemical species present in solutions specific to experimental conditions at varied pH levels.

2.3.5 Quantum Chemical Modeling

Calculations for aqueous phases were performed with the Local Density Functional Calculations on *MOL*ecules ($DMol^3$) software package (Delley, 1990). This software was chosen due to its ability to perform cluster and periodic calculations while retaining almost identical settings (basis set, pseudopotentials, density functionals, and COSMO approach of modeling surrounding water as a dielectric fluid). Computational parameters were kept consistent for all species in chemical equations. This is necessary because energies of individual species using different approaches cannot be compared; however, energies of reaction, each internally consistent but using different approaches from one another, can be combined in order to obtain an overall equation that contains (for example) charged hydrated molecular species and neutral infinite periodic crystals. The GGA scheme and PBE functional were used in conjunction with effective core potentials to account for core electrons (Dolg et al., 1987). To describe the atomic orbitals, Double Numerical plus D-functions (DND) were used as the basis set. All phases

containing U include a spin-polarized approach in order for the unpaired electron spins in the 5f orbitals to adopt their lowest energy configuration. Hydration energies were evaluated using the Conductor-like Screening Model (COSMO), a dielectric continuum model to simulate ions imbedded in a dielectric fluid (Klamt and Schuurmann, 1993). Water with a dielectric constant of 78.54 was used as the solvent.

2.3.6 In Situ Electrochemical XAS

All x-ray absorption spectroscopy (XAS) experiments were carried out at Argonne National Laboratory's Advanced Photon Source (ANL-APS) at beamline 12-BMB.

Oxidation state was ascertained by analysis of electron shell binding energies, or peak height in the x-ray absorption near edge structure (XANES) portion of the spectra. A higher oxidation state element (for example, U(VI) vs. U(IV)) will have a higher binding energy due to the extra charge. This is a result of the increased attraction forces between electrons (now that there are fewer of them). Electron configuration and vacant orbitals are assessed in much the same manner. Analysis of the relative peak height between sample runs show where the electrons are and are not located. If the peak height changes are significant, we can infer that the valence band orbital is empty in U^{6+} and full in U^{0}.

To assess changes in the coordination of samples in XANES, the first peak, or absorption edge shape, would differ between runs. Such changes can be corroborated using the extended x-ray absorption fine structure (EXAFS) spectra. Coordination information can be gathered in EXAFS by analyzing the peaks (oscillations) and the period of the EXAFS oscillations. The amplitude of EXAFS oscillation is proportional to the coordination number of the sample structure.

To assess the nature of the atoms surrounding the element for which the spectra was obtained (in this case U) the period and amplitude of the oscillatory behavior of the constructive and destructive interference patterns of emitted photoelectrons from the sample is observed. If the oscillations become larger between samples (or standards), we can conclude that heavier elements surround the U atoms under investigation (Adelani and Albrecht-Schmitt, 2012). The heavier atoms are responsible for this effect due to the abundance of e^- available to scatter.

To ascertain the interatomic distances and bond lengths, EXAFS results are fitted with software based on empirical measurements which correlate the wavelength of EXAFS oscillations with the wavelength of the emitted photoelectrons. Thus the wavelengths between successive peaks are equivalent to U-U and U-O and O-O interatomic distances. This information is processed within the Demeter® software package to obtain the Debye-Waller factor, or disorder factor. By comparing each interatomic distance with equivalent U-U, U-O, and O-O pairs; one can assess the variance of each individual interatomic distance with the computed average and solve for σ^2, or the disorder factor. Low σ^2 indicates a perfect crystalline structure with each respective interatomic distance quite close, whereas a high σ^2 indicates a flawed/distorted crystalline structure with a high degree of disorder and not very equivalent interatomic distances.

2.4 Results and Discussion

Electrochemical analysis using powder microelectrodes (PMEs) was employed to determine the electrochemical activity of U_{60} and studtite. The electrochemical characteristics of these uranyl peroxides were investigated in a variety of experimental solutions: NaCl, Na_2SO_4, and $UO_2(NO_3)_2$ (also as a reactant) in order to identify the redox transitions and probe the effect of cation and anion identity at the electrode/solid/solution interface. Electrochemical experiments

performed with these background electrolytes resulted in cyclic voltammograms (CVs) of similar shape.

2.4.1 Uranyl Peroxide Voltammetry

Cyclic voltammetry data for U_{60} crystals in a 0.05 M Na_2SO_4 (sodium sulfate) solution are shown in Figure 2.1. Prior to the addition of U_{60}, test runs were performed in the solution with clean and empty PMEs (Fig. 2.1) in order to establish a background for redox switching potentials (redox peaks or redox waves) unrelated to U_{60} and for later experiments in identical solutions. Powdered U_{60} crystals were packed into the electrode cavity to function as the working electrode and scanned at varied pH (9.3 to 3.4) and scan range. At the starting pH of 9.3, the fundamental shape and character of the voltammetric curve had changed significantly from the background. Indistinct broad redox peaks at the A_1, A_2, C_1, and C_2 position were resolved by decreasing the pH to 5 using 0.1 M H_2SO_4 as successive CVs were recorded (Fig. 2.1). Addition of acid had the effect of both reducing the background signal of the CV curve and revealing additional peaks. In solution at pH 5, an additional reduction (C_3) and oxidation peak (A_3) had emerged and all peaks had shifted slightly toward a more negative potential as compared with pH 9.3 with peak C_1 shifting by the greatest amount. No further peaks emerged at lower pH. The pH-dependence of these reactions is discussed further in Section 2.4.3.

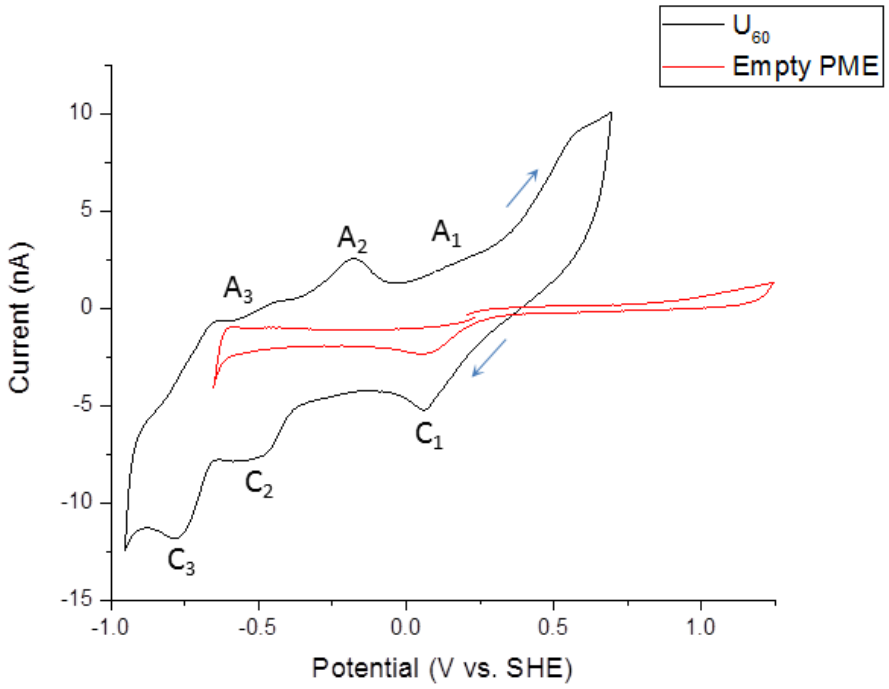

Figure 2.1: **Red:** Empty PME in Na_2SO_4 solution at pH 5 demonstrating the electrochemical background. Distinct redox peaks are attributed to the reduction of Pt. **Black:** U_{60} in Na_2SO_4 solution at pH 5 demonstrating the redox behavior of powdered U_{60} crystals. The C_2/A_2 couple is attributed to the U(VI)/U(V) transition and the C_3/A_3 couple to the U(V)/U(IV) transition. Arrows represent scan direction.

By varying the background solutions tested, the influence of the solution can be separated from the redox peaks of interest, confirming its role as the solvent only. Due to the limited number of reactive species used consistently in experimentation (U, peroxide, H_2O, and the Pt in our electrodes) and the potential range at which they appear, there are a limited number of redox transitions that can be assigned to those observed. Comparing observed redox peaks with standard reduction potentials and with values from literature further narrows the possible species undergoing reduction or oxidation (Table 2.1). Scan ranges were adjusted to potentials that would exclude reactions beyond the range of U, peroxide, H_2O, and Pt (approximately -1.0 to +1.0 V *vs.* Ag/AgCl) for Pt electrodes (Nurmi and Tratnyek, 2011).

Element	Reaction	E_0 [mV] $_{pH\ 0}$	E_0 [mV] $_{pH\ 5}$	Transition
Uranium	$(UO_2)^{2+} + e^- \rightleftharpoons (UO_2)^+$	+163	+163	$U^{6+} \rightleftharpoons U^{5+}$
	$[UO_2(H_2O)_5]^{2+} + e^- \leftrightarrow [UO_2(H_2O)_5]^+$	-483	-483	
	$UO_2^+ + 4H^+ + e^- \rightarrow U^{4+} + 2H_2O$	+380	-800	$U^{5+} \rightleftharpoons U^{4+}$
	$UO_2^+ + 3H^+ + e^- \rightarrow U(OH)^{3+} + H_2O$	+342	-1227	
	$UO_2^+ + 2H^+ + e^- \rightarrow U(OH)_2^{2+}$	+247	-343	
	$UO_2^+ + H_2O + H^+ + e^- \rightarrow U(OH)_3^+$	+92	-203	
	$UO_2^+ + 2H_2O + e^- \rightarrow U(OH)_4$	-81	-81	
	$UO_2^+ + 3H_2O + e^- \rightarrow U(OH)_5^- + H^+$	-397	-102	
	$UO_2^+ + e^- \rightarrow UO_{2(s)}$	+660	+660	
H_2O_2	$O_2 + 2H^+ + 2e^- \rightleftharpoons H_2O_2$	+690	+395	$O_2 \rightleftharpoons H_2O_2$
NO_3^-	$NO_3^-{}_{(aq)} + 2H^+ + e^- \rightleftharpoons NO_{2(g)} + H_2O_{(l)}$	+780	+190	$N^{5+} \rightleftharpoons N^{4+}$
	$NO_3^-{}_{(aq)} + 4H^+ + 3e^- \rightleftharpoons NO_{(g)} + 2H_2O_{(l)}$	+960	+567	$N^{5+} \rightleftharpoons N^{2+}$
Pt	$Pt^{2+} + 2e^- \rightleftharpoons Pt$	+1190	+1190	$Pt^{2+} \rightleftharpoons Pt^0$

Table 2.1: Published Standard Reduction Potentials versus SHE (Austin et al., 2009; Bard and Faulkner, 2001; Bratsch, 1989) at pH 0 and pH 5.

In Figure 2.1, redox couples are assigned for the redox reactions of both uranium species and non-uranium species. The reduction of U(VI) to U(V) is represented as peak C_2, with the re-oxidation of U(V) to U(VI) denoted as peak A_2. Together they are referred to as uranium redox couple C_2/A_2. The midpoint potential (E_{mid}) for the C_2/A_2 couple is calculated to be -342 mV, which does not align well with the standards in Table 2.1, but is roughly comparable to the reduction potential for the reaction describing the one e^- reduction of $[UO_2(H_2O)_5]^{2+}$ at -483 mV in the study by Austin et al. (2009). Further evidence for the assignment of C_2/A_2 being a corresponding redox couple comes from the comparable (within 10%) peak area and current between peak C_2 and A_2. The peak area and current for both C_2 and A_2 also increase in

magnitude simultaneously upon the addition of 0.025 mM uranyl nitrate ($UO_2(NO_3)_2$). This increased area with increased U in solution is observed only for peaks C_2/A_2 and C_3/A_3, and is observed for U-related peaks in several studies (Giridhar et al., 2007; Giridhar et al., 2006; Martinot et al., 1992; Renock et al., 2013; Yuan et al., 2015a).

E_{mid} values are not well defined thermodynamically as peak positions and activities of both oxidized and reduced species lack precision due to peak broadness. As a result, observed midpoint potential may differ from a thermodynamically derived (see Section 2.4.3 & 2.4.4) redox potential (E_0), but can still be used qualitatively to assign peaks to specific reactions. Furthermore, literature values for the redox potential of the U(VI)/U(V) redox couple vary widely depending on the ligand (and solvation sphere) which is attached to the U atom (Table 2.2). This has been suggested to be a result of the π-donation of the ligand, which can mix with the U 6d orbitals, thereby giving higher oxidation states of U greater stability (Hardwick et al., 2011). Further investigation into the ligand effects on U_{60} voltammetry is performed in Section 2.4.4.

The peaks denoted as C_3/A_3 are also likely representative of a coupled redox reaction as they emerge together and have comparable (within 10%) peak area and current between peak C_3 and A_3. The peak area and current for both C_3 and A_3 also increase in magnitude simultaneously upon the addition of 0.025 mM uranyl nitrate ($UO_2(NO_3)_2$). This result suggests that this peak may be attributed to the reduction (and re-oxidation) of the chemically unstable U(V) product from the preceding C_2/A_2 reaction. This behavior is furthermore indicative of uranium reduction/oxidation, as increased peak current is proportional to the amount of U product being formed, and with greater concentrations of U in the system, more product can be formed overall. The midpoint potential for C_3/A_3 is calculated to be -710 mV, which does not clearly agree with

the pH-adjusted standard redox potential (see Sec. 2.4.3 below) for the U(V)/U(IV) couple at -800 mV (Bard and Faulkner, 2001). As our redox peaks are generally characteristic of the standard reduction potentials for single-electron transitions of uranium species and peak area between couples is relatively consistent, we hypothesize that each peak in our CV is indicative of one-electron redox transitions that reduces or oxidizes the uranium within our U_{60} sample.

Compound	Solvent	E_0 (mV)	Reference
$[UO_2(O_2)(H_2O)]\cdot 2H_2O$	Solid-state	-563	Mallon et. al, 2012
$[UO_2(H_2O)_5]^{2+}$	H_2O	-483	Austin et. al, 2009
$[UO_2(DMSO)_5]^{2+}$	DMSO	-1513	Kim et. al, 2002
$[UO_2(acac)_2(DMSO)]$	DMSO	-1993	Lee et. al, 1996
$[UO_2Cl_4]^{2-}$	H_2O	+132	Morris, 2002
$[UO_2Cl_4]^{2-}$	$EMI^+BF_4^-/Cl^-$	-1523	Ogura et. al, 2011
$[U(CO_3)_5]^{6-}$	H_2O	-1003	Hennig et. al, 2010
$[UO_2(CO_3)_3]^{4-}$	H_2O	-663	Mizuguchi et. al, 1993

Table 2.2: U(VI)/U(V) redox couples for selected uranyl compounds with differing ligands (vs. SHE).
*DMSO = Dimethyl Sulfoxide, acac = acetylacetonate, EMI = 1-ethyl-3-methylimidazolium

The prominent peak at C_1 is quite distinct from C_2/A_2 and C_3/A_3. Observed peak shift towards more negative potentials with pH decrease is far more pronounced (see Section 2.4.3) indicative of a strong pH-dependence. Also absent is a defined coupled oxidation peak. Overlain on Figure 2.1 in red is the CV of an unpacked PME in identical solution conditions, which is representative of the redox behavior of platinum present in background conditions when using Pt electrodes. The figure demonstrates that the currents associated with the Pt electrode alone are relatively insignificant compared to those of the U_{60} packed in the PME in Na_2SO_4. This observation can be explained by the fact that the electroactive surface area of the U_{60} clusters is significantly greater than the electroactive surface area of the Pt at the bottom of the PME cavity. As such, redox reactions occurring on the Pt itself are not greatly affecting the peak characteristics for U_{60}. Such scans are consistent with CVs from Pt cavity and disk electrodes in

similar conditions (Furuya et al., 2015; Renock et al., 2013; Wang et al., 2009; Wang et al., 2016). However, the large reduction peak in the Pt curve is aligned with U_{60} peak C_1, therefore if the peak is not directly related to the reduction of Pt, it is likely to interfere with the peak current for any reactions occurring at that potential. The anodic scan for Pt has no such pronounced peak current, perhaps due to a shallow yet broad oxidation wave (consistent with literature findings) aligned with peak position A_1 (Furuya et al., 2015; Renock et al., 2013; Wang et al., 2009; Wang et al., 2016). Therefore any U_{60} reaction occurring near the oxidation potential for Pt is likely to be unaffected yet difficult to resolve.

Tracing the redox behavior of the bent peroxide linkers within U_{60} that make the cluster's icosahedral shape possible is far more complex than that of the uranium. A study by Gil et al. (2012) on the lower-symmetry U_{28} cluster $[K_{16}(H_2O)_2[UO_2(O_2)_2(H_2O)_2]_{0.4}((UO_2(O_2)_{1.5})_{28}]^{14-}$ suggests the peroxide (O_2^{2-}) within the cluster is reduced alongside UO_2^{2+} by two electrons to OH^-. With U_{60}, this would occur at peak position C_2 and is therefore additive to the signal from the U(VI)/U(V) transition (Fig. 2.1). On the anodic scans, OH^- is then oxidized back to O_2^{2-} along with UO_2^+. In U_{60} this occurs at peak A_2 at the U(V)/U(VI) transition. The study by Gil et al. (2012) suggests two mechanisms for a further oxidation of peroxide to dioxygen (O_2): **1.** That peroxide is oxidized directly to dioxygen via the O_2^{2-}/O_2 reaction at a standard electrode potential of -65 mV or **2.** That peroxide oxidizes first to superoxide (O_2^-) via O_2^{2-}/O_2 at a standard electrode potential of +200 mV. Given that peak A_1 is observed both after the U(V)/U(VI) transition and at a potential of +175 mV, it is probable that a superoxo complex of uranium is formed. This superoxo complex is stabilized from disproportionation by the presence of U(V) in the cavity as shown in similar experiments and calculations (Bryantsev et al., 2008; Dickman and

Pope, 1994; Gil et al., 2012). If this complex is forming, a coupled cathodic peak would be expected but was not found, possibly due to interference from the reduction of Pt at peak C_1.

Powder microelectrodes also allow for the determination of kinetic parameters of redox reactions occurring within the cavity (Cachet-Vivier et al., 2001; Cha et al., 1994; Renock et al., 2013). The separation of peak potentials between the anodic and cathodic reactions in a redox couple can be used to determine the reversibility of the reaction. An electrochemically reversible couple is any redox couple in which reduced or oxidized species rapidly gain or donate electrons to the working electrode. The reversibility is described by the equation

$$\frac{59\ mV}{n} = \Delta E_p$$

Where n is the number of electrons transferred (at 25 °C) in relation to the Nernst equation (Bard and Faulkner, 2001; Nicholson, 1965). A peak separation (ΔE_p) for a one-electron transition is considered fully reversible (Nernstian) if ΔE_p = 59 mV. A reaction that falls in the range of ΔE_p = 60-200 mV is considered quasi-reversible, and ΔE_p > 200 mV is considered an irreversible reaction. All reactions with ΔE_p > 59 mV are considered kinetically inhibited (less reversible).

The A_2/C_2 couple has an ΔE_p of 331 mV (Fig. 2.1) suggesting that the reduction of UO_2^{2+} is an irreversible process. A corresponding ΔE_p of 339 mV was observed in the irreversible reduction of UO_2^{2+} in U_{28} clusters (Gil et al., 2012). This irreversibility provides kinetic evidence for the breakdown of U_{60} clusters.

The C_3/A_3 couple describing the one-electron reduction of UO_2^{+} is quasi-reversible with an ΔE_p of 137 mV. This result indicates that the U(V)/U(IV) transition is less kinetically inhibited than the U(VI)/U(V) transition. This finding is consistent with the literature where U(V) has

been shown to be unstable in equilibrium conditions (Bryantsev et al., 2008; Choppin, 2007; Steele and Taylor, 2007; Topin and Aupiais, 2016; Yuan et al., 2015a; Yuan et al., 2015b). Gil et al. (2012) observed a quasi-reversible redox couple attributed to the oxidation of the innermost peroxo ligands of U_{28}, leading to the formation of a superoxo complex. Reversibility of the peroxo ligands in this study are complicated by the presence of a large Pt reduction peak (Fig. 2.1, peak A_1) at similar potential to any possible peroxo reduction potential. However, using peak A_1 as an approximate value of the coupled reduction wave for peroxo ligands, this study obtains a similar finding of a quasi-reversible reaction with an ΔE_p of 115 mV.

To test that the pH effects observed above were not simply a consequence of the increased conductivity of the system with the addition of H_2SO_4, U_{60} was analyzed in a solution of steadily increasing Na_2SO_4 solution at constant pH. As the solution concentration was increased from 0.05 M to 0.10 M (at constant pH), peak area and intensity diminished significantly. This finding contrasts with the result expected from simply increasing the conductivity of the solution. The result suggests that at high electrolyte concentrations, any peak intensification owing to increased conductivity is likely overshadowed by interference between the nonreactive Na_2SO_4 and electrons from the electrode. As the electrode surface becomes more and more oversaturated, the observed peak potential diminishes consistently. However, further experimentation is necessary to isolate the factors at play.

2.4.2 Uranyl Peroxide + U(VI)$_{aq}$ Voltammetry

Cyclic voltammograms of an unpacked PME in a 25 mM $UO_2(NO_3)_2$ (uranyl nitrate) solution at a pH of 9 and 5 were recorded to establish a baseline for the experimental solution. As before, scan range and pH were adjusted throughout the experiment. Uranyl nitrate CVs were found to be consistent with the literature, resulting in a single-step, two electron reduction of UO_2^{2+} to

$UO_{2(s)}$ characterized by a single large reduction peak (Giridhar et al., 2007; Giridhar et al., 2006; Hill et al., 1960; Martinot et al., 1992). U_{60} was then packed into the cavity and scanned in an identical solution. The combination of two redox-active species to an electrochemical cell carries the possibility of signal interference that complicates interpretation. However, the analysis of U_{60} in a solution of uranyl nitrate can facilitate the electrochemical characterization of U_{60}. The comparison of uranyl nitrate CVs with U_{60} CVs lends insight into the number of electrons transferred and the identification of U-related peaks.

To minimize the interference and test the effect of the $UO_2(NO_3)_2$ solution on U_{60}, subsequent experiments were performed at solution concentrations of uranium 10-100 times less than in the previous test. Background scans with empty PMEs resulted in uranyl nitrate signal intensities (peak heights) that were approximately 10-100 times less than with the U_{60}-packed electrode. In subsequent experiments where the amount of uranyl nitrate was varied from 0.2-2.3 mM (Fig. 2.2a), there was a similarly direct relationship between the amount of $UO_2(NO_3)_2$ added and the peak height (with the exception of peak A_1, A_5, C_1, and C_2). Thus, peaks A_3, A_4, C_3, and C_4 are related to the free UO_2^{2+} in solution, and these peak positions are likely uranium-related. As shown above, the increased U concentration in solution results in an increased U signal, which at high concentrations makes peaks difficult to resolve due to signal overload and peak overlap. However, the U in solution is found to resolve these peaks (as U related peaks) at lower uranyl nitrate concentrations (Fig. 2.2a). Thus, the cathodic peaks observed in Na_2SO_4 and absent in $UO_2(NO_3)_2$ (A_1, A_2, C_1, and C_2 in Fig. 2.1) are either not U related or are merely so close to one another that they overlap. The latter interpretation is comparable to that of voltammetry findings by Mallon et al. (2012) where peak positions within studtite overlap in a similar manner. Figure 2.2a demonstrates the development of such a process for the redox

transitions at peak A_3 and A_4. The two clearly defined reduction peaks at C_3 and C_4 exhibit a coupled oxidation process at peak A_4 overlapping with the oxidation at peak A_3 forming a shoulder peak at +350 mV. This, and the findings of Mallon et al. (2012) lead the assertion that, as with the more inert Na_2SO_4 solution (Section 2.4.1), we observe two coupled redox peaks with U_{60}; with the U(VI)/U(V) couple denoted as C_3/A_3, and the U(V)/U(IV) couple denoted as C_4/A_4 (Fig. 2.2b). A key diagnostic factor is the absence of the large U-reduction peak (-550 mV) characteristic of single-step, two electron, UO_2^{2+} to UO_2 uranyl nitrate voltammograms, providing further evidence that peaks C_3/A_4 and C_4/A_4 are displaying the electrochemical properties of the U_{60} packed in the PME rather than that of the uranyl nitrate solution (Giridhar et al., 2007; Giridhar et al., 2006; Hardwick et al., 2011; Martinot et al., 1992). The lack of such a proportionally large reduction wave, indicative of large reduced product formation, provides further support for a two-step, single electron reduction of U(VI) to U(IV).

As was addressed in Section 2.4.1 (and in further detail in Section 2.4.3 & 2.4.4), midpoint potentials may differ from a thermodynamically derived redox potential, but can still be used qualitatively to assign peaks to specific reactions. Therefore potentials for the C_3/A_3 couple, measured experimentally at +239 mV, are attributed to the published standard reduction potential for the U(VI)/U(V) at +163 mV (Bard and Faulkner, 2001). Potentials for the C_4/A_4 couple measured at -54 mV, however, do not align well with standard redox potentials (+273 mV for pH 0), suggesting that the UO_2^{2+} in our solution reduces/oxidizes differently in the presence of U_{60} (see Sec. 2.4.3). However, as the C_3/A_3 and C_4/A_4 couples occur at similar peak currents (+/- ~5 nA), we can infer and calculate (as shown in Sec. 2.4.3) that a similar total number of electrons (less than 7% difference *vs.* the >50% difference in uranyl nitrate) are being transferred, thus providing further support for a two-step U(VI) reduction to U(IV) in U_{60}.

The probable redox pathway for peroxide linkers within the U_{60} structure mirrors that of the findings in Na_2SO_4 solutions. Peroxide (O_2^{2-}) undergoes a two-electron reduction to OH^-, reduced at similar potential to the U(IV)/U(V) transition (C_3), then in positive-going scans oxidizes back to O_2^{2-} alongside the U(V)/U(VI) transition (A_3). This is confirmed by the observation of increased peak current and area at the C_2/A_3 couple relative to C_4/A_4 (U(V)/U(IV) transition). Furthermore, this increased peak area could account for the peak overlap observed in peak A_3 and A_4, as the signal in A_3 is enlarged by constructive signal from the 2-electron transition from OH^- to O_2^{2-}. Peroxide has subsequently been found to oxidize once more to O_2 with the possibility of an intermediate superoxide (O_2^-) state. Peak A_2 and A_1 are candidates for these transitions as the superoxide state has been shown previously to be stabilized by U(V), rendering any associated superoxo reaction proportional to the concentration of U species in solution (Gil et al., 2012). Furthermore, peroxide transitions on the surface of U have been shown to occur solely in a mixed U(V)/U(VI) state (Goldik et al., 2005). Peak A_1, unrelated to U, is therefore more likely to represent the transition from the superoxo state to dioxygen as U concentration (in the form of uranyl nitrate) does not affect the concentration of the peroxide reactant. However, as the oxidations described by peaks A_2 and A_1 do not align with the corresponding standard electrode potentials, further experimentation must be done before the presence of a superoxide complex can be confirmed.

The kinetic behavior of U_{60} in uranyl nitrate solution differs greatly from that in sodium sulfate. The ΔE_p of the U(VI)/U(V) transition (C_3/A_3) irreversible at 429 mV, indicating that the reaction is more kinetically inhibited than in Na_2SO_4. So too is the ΔE_p of the U(V)/U(IV) transition (C_4/A_4) at 595 mV far more kinetically hindered than in an inert solution. It is clear that the addition of a redox-active U-bearing solution kinetically inhibits the U redox reactions

on U_{60}. This result is however expected due to the increased U in solution leading to a diffusion-limiting factor in voltammetric response. The U(V)/U(IV) transition is found also to be more inhibited than the U(VI)/U(V) transition, reversing a trend observed in inert solutions due to the instability of the U(V) species (Bryantsev et al., 2008; Choppin, 2007; Steele and Taylor, 2007; Topin and Aupiais, 2016; Yuan et al., 2015a; Yuan et al., 2015b). However, this finding is likely to be a result of the difficulties in determining peak separations due to the broadness of the anodic and cathodic peaks and the overlapping of the U(V)/U(IV) and U(VI)/U(V) oxidation peaks (Renock et al., 2013).

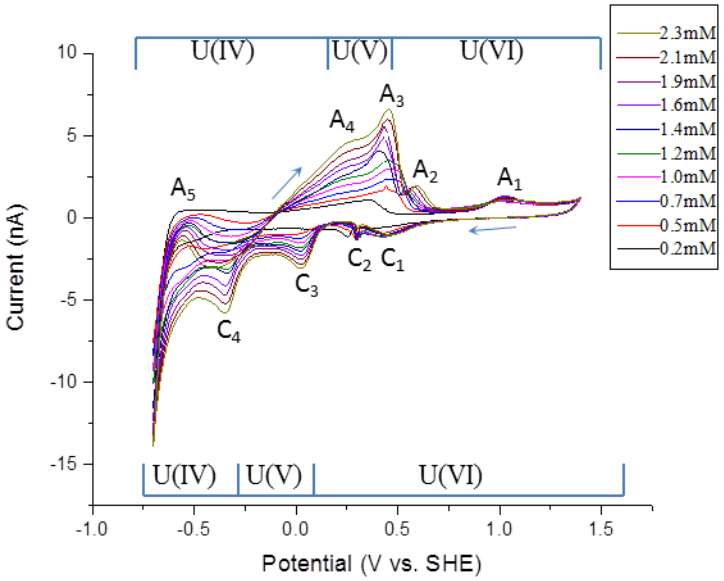

Figure 2.2a: CV of U_{60} in progressively higher concentrations of $UO_2(NO_3)_2$ solution at constant pH 5. Growth of peaks indicates which peaks are uranium related (C_3, C_4, A_4, A_3). Stable peaks could denote the redox behavior of U_{60}'s peroxide constituents. Position A_5 does not represent a peak but rather an artifact of the potential reversal in CV. Two separate cathodic peaks indicate a two-step reduction of U(VI). Two overlapped anodic peaks suggest two oxidation processes at similar potential.

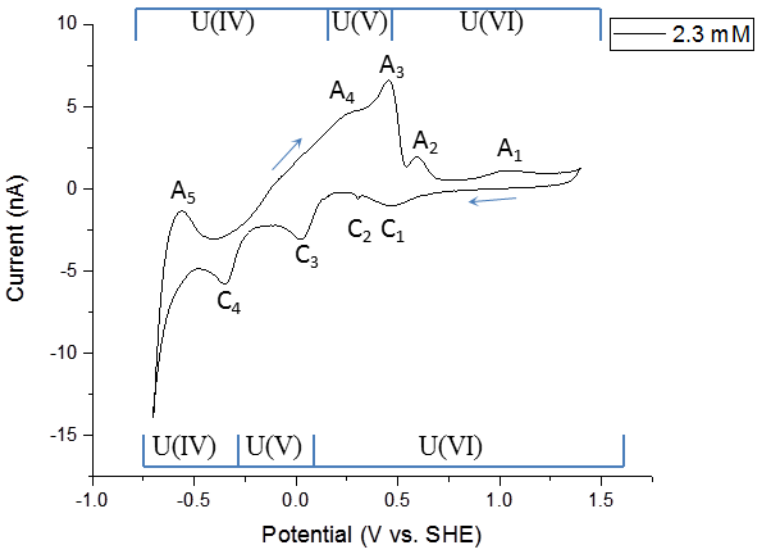

Figure 2.2b: U_{60} in 2.3 mM uranium nitrate ($UO_2(NO_3)_2$) solution at constant pH 5 (isolated from Fig. 2.2a). Arrows demonstrate the scan direction.

2.4.3 Reaction pH Dependence

A standard or formal electrode potential is the measure of the tendency of chemical species in a reaction to be reduced via the acquisition of electrons or oxidized via the loss of electrons as predicted by thermodynamic equations. The more positive the standard electrode potential, the more likely it is for the species to gain electrons and become reduced. Therefore, when a midpoint potential in cyclic voltammetry moves to the right (more positive), thereby increasing the tendency of the species to be reduced at a given external potential, key insight into the nature of the reaction (Equation 2 in this case) is provided. Midpoint potentials that shift in response to a change in pH are known as pH-dependent reactions with the amount of shift is dependant on the number of H^+ ions transferred in the reaction. By extrapolating from thermodynamic data given for reactions at different pH, one can predict where a redox peak will be located, and can used to identify the reaction taking place at any given pH.

Redox reactions that are pH-independent, like Equation 1, exhibit no change in electrode potential as the pH of the solution changes. Equation 1 lacks H^+ (or OH^-) as either a reactant or product. This is why the C_2/A_2 peaks in the voltammogram in Figure 2.1 do not shift horizontally as the pH changes (0 mV/pH).

$$(UO_2)^{2+} + e^- \rightarrow (UO_2)^+ \qquad E^o = +163 \text{ mV vs. SHE} \qquad \frac{\Delta E}{pH} = 0\frac{mV}{pH} \qquad (1)$$

U(VI)/U(V) redox couple at pH = 0-14 (Bard and Faulkner, 2001; Bratsch, 1989).

Reactions that are pH-dependent, such as Equation 2, are far more common and exhibit a shift in potential proportionate to the number of H^+ transferred (and therefore pH) that can be measured with cyclic voltammetry (Fig. 2.1 C_3/A_3). Published pH-dependent standard electrode potentials are almost always given at pH 0 or 14.

$(UO_2)^+ + 4H^+ + e^- \rightarrow U^{4+} + 2H_2O_{(l)}$ E^o = +273 mV vs. SHE $\frac{\Delta E}{pH} = 236\frac{mV}{pH}$ (2)

U(V)/U(IV) redox couple at pH = 0 (Bard and Faulkner, 2001).

For a Nernstian system, the potential shift as a consequence of pH is directly proportional to the number of protons transferred (**m**) per electron (**n**) in the system. Using the Nernst equation (3a) one can predict the amount of potential shift in an ideal system at equilibrium. Subsequent derivation can predict the number of protons transferred per electron (3b).

$$E = E^o - \frac{59\,\text{mV}}{n} \cdot \log(Q) \quad (3a)$$

$$E = E^o - \frac{59\,\text{mV}}{n} \cdot \log(Q' \cdot [H^+]^m)$$

$$E = E^o - \frac{59\,\text{mV}}{n} \cdot \log(Q') - \frac{(59\,\text{mV})(m)(\text{pH})}{n} \quad (3b)$$

Or at the midpoint potential, where the reductant and oxidant concentration are, on average, equal:

$$E = E^o - \frac{(59\,\text{mV})(m)(\text{pH})}{n} \quad (3c)$$

Where **E** is the experimental potential for a given reductant/oxidant ratio, $\mathbf{E^o}$ is the standard reduction potential, **n** is the number of electrons transferred according to reaction stoichiometry, **Q** is the reaction quotient (the activity of the reductants divided by the activity of the oxidants), **Q'** is the reaction quotient without the H^+ included, and $\boldsymbol{m}$ is the number of H^+ ions transferred in the reaction (negative if present in reaction products) at equal reductant/oxidant concentration.

To apply this methodology to the pH-dependent U(V)/U(IV) couple (C_3/A_3 in Fig. 2.1), the full redox reaction must first be identified. Based on the experimental conditions used in this study, the most likely reactions to occur were determined using thermodynamic data (Fig. 2.3).

$$UO_2^+ + 4H^+ + e^- \rightarrow U^{4+} + 2H_2O \quad (4a)$$

$$UO_2^+ + 3H^+ + e^- \rightarrow U(OH)^{3+} + H_2O \quad (4b)$$

$$UO_2^+ + 2H^+ + e^- \rightarrow U(OH)_2^{2+} \quad (4c)$$

$$UO_2^+ + H_2O + H^+ + e^- \rightarrow U(OH)_3^+ \quad (4d)$$

$$UO_2^+ + 2H_2O + e^- \rightarrow U(OH)_4 \quad (4e)$$

$$UO_2^+ + 3H_2O + e^- \rightarrow U(OH)_5^- + H^+ \quad (4f)$$

$$UO_2^+ + e^- \rightarrow UO_{2(s)} \quad (4g)$$

From Eqn. 3c it is shown that the number of H^+ transferred in each reaction will determine the amount of peak potential shift as the pH is varied. For example, using Eqn. 4a (the most prominent species at pH 0), it is predicted that this peak would shift to more positive potentials by a factor of 4·59 = +236 mV per pH unit decrease (Table 2.3). Likewise applying Eqn. 4d (the most prominent species at pH 3.5) results in a predicted shift of 1·59 = +59 mV per pH unit decrease. Equation 3b demonstrates that by increasing the H^+ concentration in the solution, reactants are increased, increasing the amount of (reduced) products, thereby increasing the ability of electrons to be accepted, which is consistent with the progressively higher reduction potentials observed.

Table 2.3: U(V)/U(IV) species in solution with associated theoretical peak shift values (x) and standard electrode potentials E° (vs. SHE).			
(a)	$UO_2^+ + 4H^+ + e^- \rightarrow U^{4+} + 2H_2O$	x_0 = 236 mV/pH	$E°_0$ = +380 mV
(b)	$UO_2^+ + 3H^+ + e^- \rightarrow U(OH)^{3+} + H_2O$	x_1 = 177 mV/pH	$E°_1$ = +342 mV
(c)	$UO_2^+ + 2H^+ + e^- \rightarrow U(OH)_2^{2+}$	x_2 = 118 mV/pH	$E°_2$ = +247 mV
(d)	$UO_2^+ + H_2O + H^+ + e^- \rightarrow U(OH)_3^+$	x_3 = 59 mV/pH	$E°_3$ = +92 mV
(e)	$UO_2^+ + 2H_2O + e^- \rightarrow U(OH)_4$	x_4 = 0 mV/pH	$E°_4$ = -81 mV
(f)	$UO_2^+ + 3H_2O + e^- \rightarrow U(OH)_5^- + H^+$	x_5 = -59 mV/pH	$E°_5$ = -397 mV
(g)	$UO_2^+ + e^- \rightarrow UO_{2(s)}$	x_6 = 0 mV/pH	$E°_6$ = +660 mV

Despite this linear relationship, experimental measurements exhibit a nonlinear U(V)/U(IV) redox peak shift of 12.9 mV per pH unit at pH 9.3-5 and a shift of 44.4 mV per pH unit at pH 5-3.4. This shift is a consequence of the reactions described in Equations 4a-g transferring too many or too few protons, resulting in redox peak shifts that are inconsistent with observed pH shift at pH 0-14. The U(V)/U(IV) transition in U_{60} is therefore a more complex system than described by Eqn. 3c. Furthermore, standard electrode potentials are typically given for reactions occurring at pH 0 (and sometimes at pH 14). This poses no issues with pH-independent reactions, but pH-dependent reactions must be adjusted from pH 0 to the relevant pH (*e.g.* groundwater pH). In so doing, one has changed the fundamental chemistry of the reaction relative to the standard and therefore it may no longer be accurate. Thus, the reactions described in Eqn. 4a-c need to be modified in order to reflect the pH shift observed and to represent the actual aqueous species to be expected at the experimental (or environmental) conditions. If no ligands other than hydroxide or water are in the system, the U(IV) species considered are: U^{4+}, $U(OH)^{3+}$, $U(OH)_2^{2+}$, $U(OH)_3^+$, $U(OH)_4$, $U(OH)_5^-$, and UO_2 with the pKa and ΔG values listed in Table 2.4.

For a general chemical equilibrium:

$$\alpha A + \beta B = \rho R + \sigma S \quad (5a)$$

$$K = \frac{[R]^{\rho}[S]^{\sigma}}{[A]^{\alpha}[B]^{\beta}} \quad (5b)$$

$$\Delta G = -RTlnK = -nFE^{\circ} \quad (5c)$$

Where **ΔG** is the Gibbs free energy change of the reaction, **K** is the equilibrium constant, **F** is the Faraday constant (96485.3 $C \cdot mol^{-1}$), **R** is the universal gas constant (8.314 $J \cdot K^{-1} \cdot mol^{-1}$), **T** is the temperature (298.15 K), and $\mathbf{E^o}$ is the standard reduction potential for a given reductant/oxidant ratio.

Table 2.4: U(V)/U(IV) species with equilibrium constant and Gibbs free energy change [J/mol] calculated from thermodynamic data as pertains to experimental conditions in this study.

(a)	$UO_2^+ + 4H^+ + e^- \rightarrow U^{4+} + 2H_2O$	$K_0 = 4.01 \cdot 10^6$	$G_0 = -3.76 \cdot 10^4$
(b)	$U^{4+} + H_2O \rightarrow U(OH)^{3+} + H^+$	$K_1 = 1.63 \cdot 10^{-1}$	$G_1 = 4.49 \cdot 10^3$
(c)	$U(OH)^{3+} + H_2O \rightarrow U(OH)_2^{2+} + H^+$	$K_2 = 1.97 \cdot 10^{-2}$	$G_2 = 9.74 \cdot 10^3$
(d)	$U(OH)_2^{2+} + H_2O \rightarrow U(OH)_3^+ + H^+$	$K_3 = 2.01 \cdot 10^{-3}$	$G_3 = 1.54 \cdot 10^4$
(e)	$U(OH)_3^+ + H_2O \rightarrow U(OH)_4 + H^+$	$K_4 = 2.10 \cdot 10^{-4}$	$G_4 = 2.10 \cdot 10^4$
(f)	$U(OH)_4 + H_2O \rightarrow U(OH)_5^- + H^+$	$K_5 = 1.15 \cdot 10^{-8}$	$G_5 = 4.53 \cdot 10^4$
(g)	$U(OH)_4 \rightarrow UO_2 + 2H_2O$	$K_6 = 2.49 \cdot 10^{-8}$	$G_6 = 4.33 \cdot 10^4$

Using aqueous geochemical modeling software (see Section 2.3.4), thermodynamic data (Table 2.4) and the concentration of chemical species present in our solutions at different pH levels (Fig. 2.3) was calculated. The chemical species with the highest concentration at a given pH was considered to be dominant in solution. Thus it was found (using Fig. 2.3) that the transition of UO_2^+ to U^{4+} is dominant (or favorable) only from pH 0-1.1, meaning that the published standard electrode potential (based on a reaction occurring at pH 0) is accurate only for reactions that take place between pH 0 and 1.1. However, transitions from UO_2^+ to $U(OH)_4$ (Eqn. 4e), UO_2^+ to $U(OH)_3^+$ (Eqn. 4d), and UO_2^+ to $U(OH)_5^-$ (Eqn. 4c) are more favorable over

experimental conditions (pH 3-9) and consequently most reactions occurring in nature. In the formation of solids, the most thermodynamically stable species was $UO_{2(s)}$. These results are consistent with experimental results found by Manfredi et al. (2006).

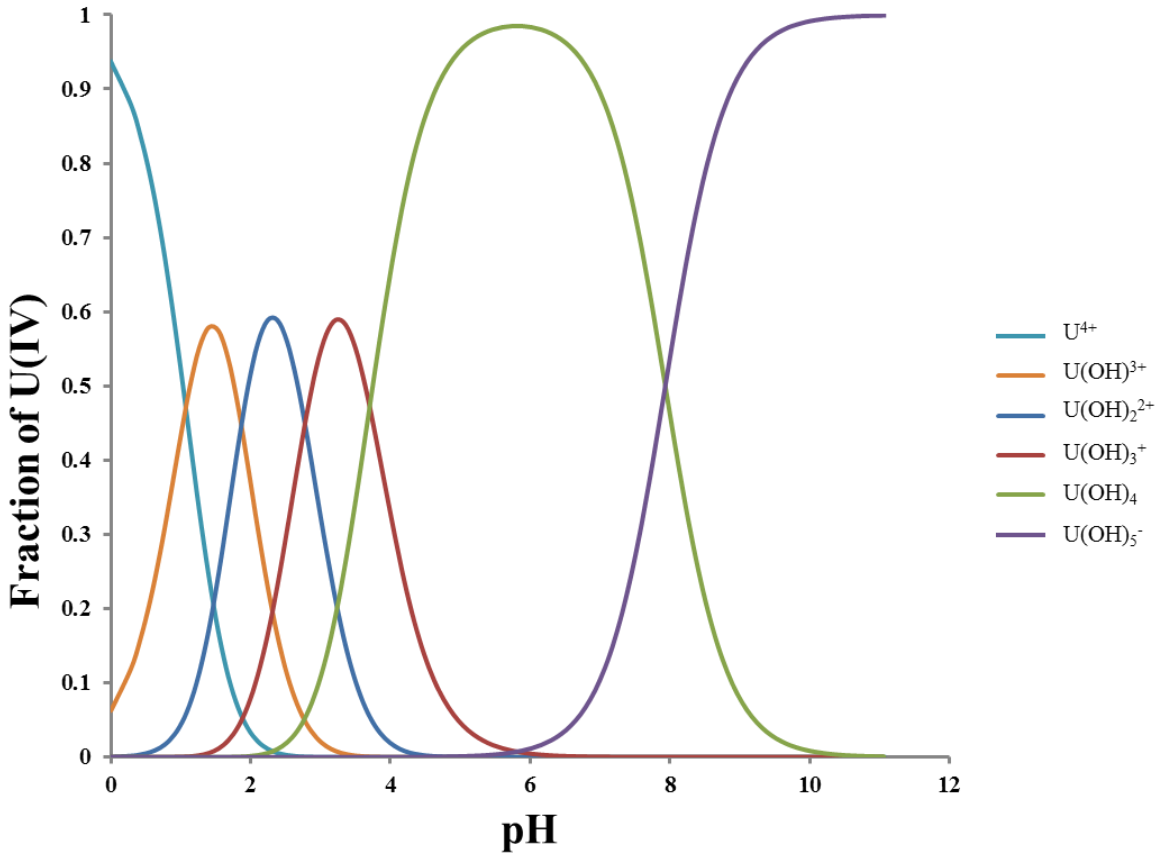

Figure 2.3: Log Concentration (Molal) vs. Solution pH diagram. Solution conditions from Figure 2.2 are modelled (2.3 mM $UO_2(NO_3)_2$). Curves have been normalized to reflect concentration of U^{4+} species only - some species are omitted for clarity.

Given that the published standard electrode potentials describe pH-dependent reactions occurring only at pH 0 and that such standards are typically derived from calorimetry data, this study has derived standards to match experimental pH conditions. To derive both experimentally and environmentally-relevant standard electrode potentials, calorimetry data was used in

conjunction with Eqn. 5c to produce Table 2.3 (Langmuir, 1978). It was found that these derived electrode potentials align well with the potentials calculated from concentration data in Fig. 2.3.

As this pertains to the CV of U_{60} in Fig. 2.2 (uranyl nitrate solution at pH 5), at these conditions we predict (using Table 2.5) that the U(V)/U(IV) reaction taking place 95.7% of the time is UO_2^+ to $U(OH)_4$. Given this, and the 4.3% contribution of other reactions (mostly UO_2^+ to $U(OH)_3^+$) we find (using Table 2.6 & 2.7) that the electrode potential at which we should observe the U(V)/U(IV) transition is -77 mV, which compares well with the observed U(V)/U(IV) transition at -54 mV from cyclic voltammetry. The 23 mV difference between the experimentally observed transition and the thermodynamically-derived potential could be due to error within published calorimetry data, measurements of solution composition, adsorption energy, small sample size, changes in electrode potential due to mineral powder, or to the slight differences in pH between solution outside the PME cavity and within, as suggested by Cook & Becker (2017) [in revision].

To discover the reason for the 23 mV discrepancy between experimental potentials and those based on solution condition, both thermodynamically-calculated and experimentally-determined pH shift was plotted versus solution pH in Figure 2.4. Agreement between calculated peak shift (predicted from thermodynamic data) and observed peak shift increases certainty in peak assignment. Figure 2.4 demonstrates that calculated values consistently parallel the peak shift observed in experimental conditions, resulting in greater confidence in assignment of the U(V)/U(IV) transition. However, the data in Fig. 2.4 show a slight underestimation in calculated values. This is expected due to the high reactive surface area inherent in powder microanalysis. Fine U_{60} crystals are forced into the electrode cavity making them finer still and as such, adjacent

clusters no longer form a uniform crystalline structure, exposing greater cluster surface area for voltammetric response.

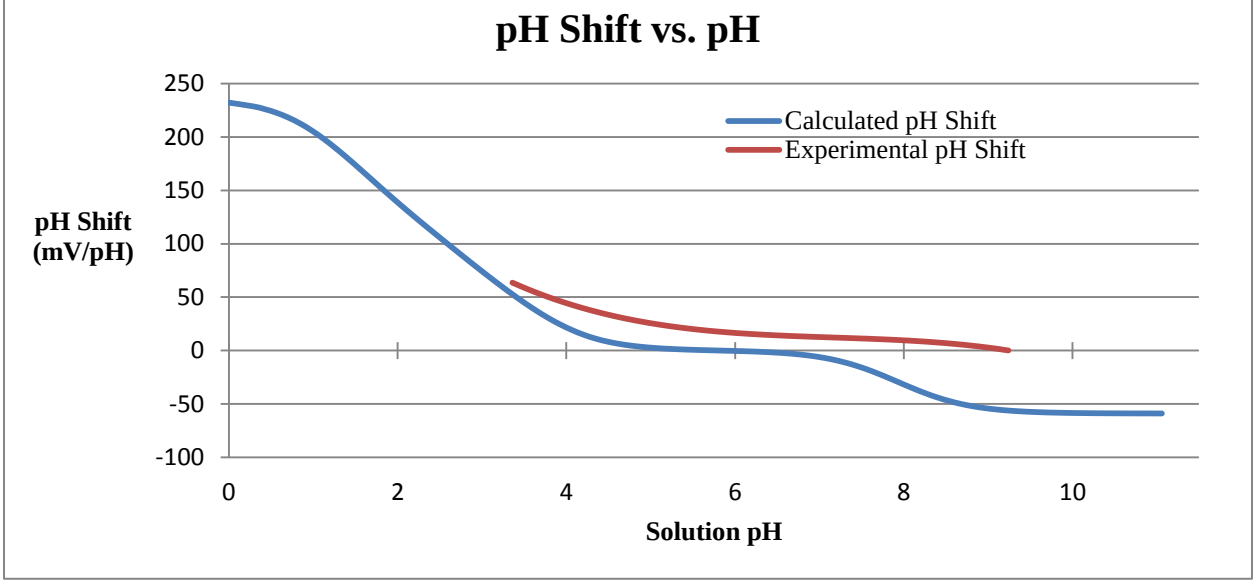

Figure 2.4: Thermodynamically-derived pH shift vs. observed pH shift in experimental conditions (U_{60} PME in a 2.3 mM uranyl nitrate solution). Calculated values consistently underestimate observed pH shift.

It was found that equilibrium peak shift across the experimental range is best modelled by first calculating the Nernstian peak shift for each reaction (Table 2.3), and then applying this shift to the relative contribution of each species to the reaction at each pH unit (Table 2.5). Experimental measurements exhibit a U(V)/U(IV) average redox peak shift of 12.9 mV/pH at pH 9.3-5 and a shift of 44.4 mV/pH at pH 5-3.4, which is consistent with the calculated peak shift values in Table 2.5, where solutions at pH 5 are expected to shift 2.4 mV/pH and those at pH 3.4 are expected to shift 44.5 mV/pH. Furthermore, the overall trend in Table 2.5 (wherein the peak shift increases with decreasing solution pH) is consistent with experimental observations (Fig. 2.4).

Table 2.5: Percent contribution of U^{4+} species to the U(V)/U(IV) reaction calculated from Figure 2.3.

pH	$\%U^{4+}$	$\%U(OH)^{3+}$	$\%U(OH)_2^{2+}$	$\%U(OH)_3^{+}$	$\%U(OH)_4$	$\%U(OH)_5^{-}$	Total %	mV/pH
0	93.7	6.3	0.0	0.0	0.0	0.0	100	**232.2**
3.4	0.0	0.2	9.9	55.0	34.9	0.0	100	**44.5**
5	0.0	0.0	0.0	4.2	95.7	0.1	100	**2.4**
9.3	0.0	0.0	0.0	0.0	3.6	96.4	100	**-56.9**

Table 2.6: Electrode potentials at varied pH as predicted from standard reduction potentials and reaction quotient.

Reaction	Standard Eh [mV]	pH-0	pH-1	pH-2	pH-3	pH-4	pH-5	pH-6	pH-7
$UO_2^{+} + 4H^{+} + e^{-} \leftrightarrow U^{4+} + 2H_2O$	273_a	275	39	-197	-433	-669	-905	-1141	-1377
$UO_2^{+} + 4H^{+} + e^{-} \leftrightarrow U^{4+} + 2H_2O$	390_b	392	156	-80	-316	-552	-788	-1024	-1260
$UO_2^{2+} + e^{-} \leftrightarrow UO_2^{+}$	163_a	145	145	145	145	145	145	145	145
$UO_2^{2+} + e^{-} \leftrightarrow UO_2^{+}$	160_b	145	145	145	145	145	145	145	145
Reaction	**Standard Eh [mV]**	**pH-8**	**pH-9**	**pH-10**	**pH-11**	**pH-12**	**pH-13**	**pH-14**	
$UO_2^{+} \leftrightarrow U^{4+}$	380	-1613	-1849	-2085	-2321	-2557	-2793	-3029	
$UO_2^{+} \leftrightarrow U(OH)^{3+}$	-342	-1496	-1732	-1968	-2204	-2440	-2676	-2912	
$UO_2^{+} \leftrightarrow U(OH)_2^{2+}$	247	145	145	145	145	145	145	145	
$UO_2^{+} \leftrightarrow U(OH)_3^{+}$	92	145	145	145	145	145	145	145	

(a) (Bard and Faulkner, 2001) (b) (Bratsch, 1989)

Table 2.7: Electrode potentials at varied pH as predicted from experimentally relevant conditions, reactions, and the reaction quotient.

Reaction	Standard Eh [mV]	pH-0	pH-1	pH-2	pH-3	pH-4	pH-5	pH-6	pH-7	Shift/pH [mV]
$UO_2^{+} \leftrightarrow U^{4+}$	380	380	144	-92	-328	-564	-800	-1036	-1272	-263
$UO_2^{+} \leftrightarrow U(OH)^{3+}$	-342	-342	-519	-696	-873	-1050	-1227	-1404	-1581	-177
$UO_2^{+} \leftrightarrow U(OH)_2^{2+}$	247	247	129	11	-107	-225	-343	-461	-579	-118
$UO_2^{+} \leftrightarrow U(OH)_3^{+}$	92	92	33	-26	-85	-144	-203	-262	-321	-59
$UO_2^{+} \leftrightarrow U(OH)_4$	-81	-81	-81	-81	-81	-81	-81	-81	-81	0
$UO_2^{+} \leftrightarrow U(OH)_5^{-}$	-397	-397	-338	-279	-220	-161	-102	-43	16	+59
Reaction	**Standard Eh [mV]**	**pH-8**	**pH-9**	**pH-10**	**pH-11**	**pH-12**	**pH-13**	**pH-14**		**Shift/pH [mV]**
$UO_2^{+} \leftrightarrow U^{4+}$	380	-1508	-1744	-1980	-2216	-2452	-2688	-2924		-263
$UO_2^{+} \leftrightarrow U(OH)^{3+}$	-342	-1758	-1935	-2112	-2289	-2466	-2643	-2820		-177
$UO_2^{+} \leftrightarrow U(OH)_2^{2+}$	247	-697	-815	-933	-1051	-1169	-1287	-1405		-118
$UO_2^{+} \leftrightarrow U(OH)_3^{+}$	92	-380	-439	-498	-557	-616	-675	-734		-59
$UO_2^{+} \leftrightarrow U(OH)_4$	-81	-81	-81	-81	-81	-81	-81	-81		0
$UO_2^{+} \leftrightarrow U(OH)_5^{-}$	-397	75	134	193	252	311	370	429		+59

Through analysis of the pH-dependence of redox reactions in cyclic voltammetry and solution composition modeling, it is possible to identify the precise reactions taking place in solution and the electrode surface. These reactions can then be paired with thermodynamic data to provide an accurate prediction for electrode potentials at any pH and any solution composition. The rate at which Eh changes with pH as observed (44.4 mV/pH at pH 3.4) is consistent with no known single redox reaction, but when reactions are partitioned in direct relationship to their concentration in solution, the resultant shift can be calculated to within 0.2% of experimental values (44.5 mV/pH at pH 3.4). Additionally, it has been shown that if predicted reaction pH dependence matches the observed pH dependence of a reaction, then the peak assignment is likely correct. Further work is currently underway to discover if there are implications for this methodology outside of the U(V)/U(IV) system. The application of this procedure to U_{60} clusters is promising, as uranyl clusters have been shown to exhibit behavior consistent with that of dissolved aqueous complexes.

2.4.4 Computational Modeling of Ligand-Facilitated Peak Shift in Electrochemistry

The standard reduction potential is the tendency for a chemical species to be reduced, and is measured in volts at standard conditions. It is the potential difference between the cathode and anode upon reduction or oxidation. However, when performing solid-state electrochemistry, such as with a PME or mineral electrode, adsorption and hydration should also be considered when determining a reduction potential.

(6) $$UO_2^{2+}{}_{solution} \rightarrow \text{Adsorption} \rightarrow \mathbf{UO_2^{2+}{}_{ads}} \rightarrow \mathbf{UO_2^{+}{}_{ads}} \rightarrow UO_2^{+}{}_{solution}$$

The signal observed in cyclic voltammetry (the E_{mid}) in this study is likely related to the reaction specified in bold in Equation 6. As such, the E_{mid} from this reaction may not correlate with the standard reduction potential for uranyl (Eqn. 7).

(7) $UO_2^{2+} + e^- \leftrightarrow UO_2^+$ $E_0 = +0.160$ V (vs. SHE)

Furthermore, we find that midpoint potentials for a given transition (like UO_2^{2+}/UO_2^+) are not consistent between complexes (Table 2.2).

Although the standard electrode potential for Equation 7 is well defined in the literature, less common and newly-synthesized complexes of uranium (like U_{60}) have not been well characterized. In order to approximate the electrode potential for an uncharacterized complex of uranium, we used computational models to compare the adsorption energy and free energy of formation between the unknown uranyl complex (U_{60}) and a known complex (UO_2^{2+}). However, it must be noted that the energies calculated here are not equal to the Gibbs free energy of the reaction, but rather the total nuclear and electronic energy of the complex in a vacuum at 0 K. Despite this, we can determine the voltage difference between the observed and the standard reduction potential from formation energies. Similarly, if we can determine the adsorption energy, we can determine the voltage difference between the observed and the standard reduction potential (Eqn. 8).

(8) $(E_{adsoprtion}^{6+} \rightarrow E_{adsorption}^{5+}) = (\Delta G/F) = \text{Shift in } E_{mid}$

Correspondingly, if we determine the formation energy of an unknown uranyl complex, we can predict the shift in E_{mid} between it and a known uranyl complex.

As a result we consider U_{60} and free uranyl:

(9) $[UO_2(H_2O_2)_2(H_2O)_2]^{2+} + e^- = [UO_2(H_2O_2)_2(H_2O)_2]^+$

$E_{mid} = -0.342$ V (vs. SHE) [Experiment]

(10) $[UO_2(H_2O)_5]^{2+} + e^- = [UO_2(H_2O)_5]^+$

$E_{mid} = +0.160$ V (vs. SHE) [Bratsch, 1989]

And calculate:

(11) $\Delta G^{6+} = [UO_2(H_2O_2)_2(H_2O)_2]^{2+} - [UO_2(H_2O)_5]^{2+}$

(12) $\Delta G^{5+} = [UO_2(H_2O_2)_2(H_2O)_2]^{+} - [UO_2(H_2O)_5]^{+}$

Then determine:

(13) $K^{6+} = e^{-\frac{\Delta G^{6+}}{RT}}$

(14) $K^{5+} = e^{-\frac{\Delta G^{5+}}{RT}}$

Then apply the following formula (equivalent to Eqn. 3):

(15) $-RT\ln(K^{6+}/K^{5+})F^{-1} = [-RT\ln(K^{6+}) - RT\ln(K^{5+})]F^{-1} = (\Delta G^{6+} - \Delta G^{5+})F^{-1}$

$= (\text{Free E of reduction})F^{-1} = \text{Shift in } E_{mid}$

$= (-20243 \text{ J/mol})(96485 \text{ C/mol})^{-1} =$ **-0.210 V**

Applying this solid-state methodology (Eqn. 11-15) to the U_{60} uranyl complex (no known standard reduction potential or midpoint potential) we estimate that the midpoint potential for the U(VI)/U(IV) transition will shift toward more negative potentials by 0.210 V (Table 2.8). Equation 15 provides the shift in potential between reaction 9 & 10, between the reduction potential for the free uranyl complex and the reduction potential of the U_{60} complex. Although this calculation underestimates the experimentally-observed -0.502 V difference between $UO_2(H_2O)_5$ and $UO_2(H_2O_2)_2(H_2O)_2$, it does however provide an approximation of the magnitude and direction of the peak shift in question. An exact value is not expected due to the complexity of calculations that exactly model electrochemical interactions and the use of a simplified U_{60} molecular fragment $UO_2(H_2O_2)_2(H_2O)_2$ (Fig. 2.5) in place of the true U_{60} structure ($Li_{40}K_{20}[UO_2(O_2)(OH)]_{60}(H_2O)_{214}$). This is confirmed by using this methodology to predict the

shift of a well-known complex of uranium from UO_2^{2+} (see Appendix B). Another contributing factor to the disparity between the calculated and observed midpoint potentials for U_{60} is the effect of the background electrolyte solution chemistry. Mallon et al. (2012) found that the larger the ionic radii of the background solution cation, the more negative the reduction potential observed.

Studtite, a uranyl complex that has no known standard electrode potential (but does have a published midpoint potential: E_{mid} = -0.563 V) was chosen to further test this methodology as an analog (Table 2.8). Calculations performed (in the solid state) with $UO_2(H_2O)_5$ and a simplified studtite molecular fragment $UO_2(H_2O_2)_2(H_2O)_2$ (Fig. 2.5) (from $UO_2((UO_2)O_2(H_2O)_2 \cdot (H_2O)_2$, applying the Eqn. 11-15, estimate a peak shift of studtite from the standard free uranyl ($UO_2(H_2O)_5$, E_0 = +0.160 V) will be -0.317 V, again underestimated with respect to the experimentally-observed -0.723 V difference (Mallon et al., 2012).

In order to provide a more realistic model for the formation energies of different uranyl complexes and their relationship to the observed shift in midpoint potential in cyclic voltammetry for a future study, a solvation model was applied to the solid-state methodology above. The Conductor-like Screening Model (COSMO) program is a continuum solvation model in which the uranyl can form a cavity within a dielectric continuum representing the solvent (such as that used in each electrochemical experiment). This model, implemented to imbed each uranyl complex in a dielectric fluid (solvent) with a dielectric constant of 78.54 (at 25°C) to represent water, can evaluate the electrostatic contribution to the free energy of solvation. The best comparison between calculation and experiment is typically found by combining explicit water molecules with a dielectric fluid surrounding the first hydration sphere (Klamt and Schuurmann, 1993). The calculations in this study for the uranyl aquo complex would include

the 5 equatorial water molecules and an additional 10 explicit water molecules in the first hydration shell (a configuration where each of the 5 equatorial waters can have two explicit water molecules directly hydrogen-bonded) (Austin et al., 2009; Buhl and Kabrede, 2006). The resulting formation energy for the known uranyl aquo complex can be compared to those found in the literature; from -18.02 eV to -17.78 ± 0.2 eV and explicit water configurations can be kept consistent for the uncharacterized U_{60} uranyl complex (Buhl et al., 2006; Gutowski and Dixon, 2006). It is however known that COSMO consistently underestimates the hydration energies of smaller ionic species (Renock et al., 2013).

Furthermore, Hay et al. (2000) found that exact reproduction of electrochemical potentials using computational models is completely dependent on the type of effective potential used in calculations and can vary by as much as 2 eV. Despite this, it was found that computational models represent relative trends in reduction potentials quite effectively, within a few tenths of an eV.

$U_{complex}$ vs. UO_2	**$\Delta G(U^{6+})$ [V]**	**$\Delta G(U^{5+})$ [V]**	**E_{mid} Shift [V]**	**Expected E_{mid} [V]**	**Actual E_{mid} [V]**
Studtite vs. UO_2^{2+}	-0.721	-0.404	-0.317	-0.157	-0.563
U_{60} vs. UO_2^{2+}	0.787	0.997	-0.210	-0.050	-0.341

Table 2.8: From left to right: U^{6+} free energy of formation difference between uranyl complex and $UO_2(H_2O)_5$, U^{5+} free energy of formation difference between uranyl complex and $UO_2(H_2O)_5$, the expected shift in E_{mid} from the standard redox potential of UO_2^{2+} (+0.160 V), the expected E_{mid} of the uranyl complex using the calculated E_{mid} shift, the actual E_{mid} observed from experiments.

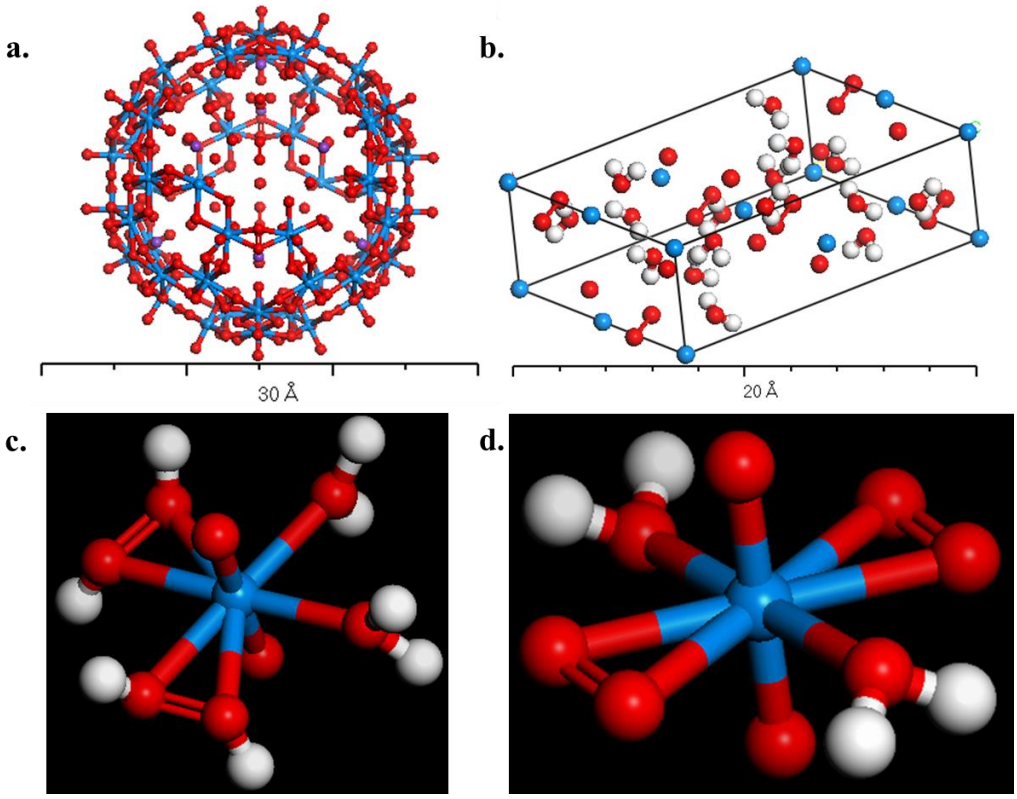

Figure 2.5: (a.) U_{60} cluster molecular model. (b.) Studtite unit cell. (c.) U_{60} fragment from one of the uranyl centers in (a.). (d.) Studtite fragment from one of the uranyl centers in (b.).

An additional hypothesis from Austin et al. (2009), Morris (2002), and Mallon et al. (2012) suggest that differences in E_{mid} stem from differences in the coordination and solvation environment about the uranyl. The stronger the electron donor ligand a uranyl complex has, the more negative the E_{mid} will be.

2.4.5 In Situ Synchrotron Electrochemical XAS

In order to ascertain the oxidation state as a function of electrochemical potential, *in situ* synchrotron electrochemical x-ray absorption spectroscopy (XAS) was carried out at Argonne National Laboratory's Advanced Photon Source (ANL-APS). Unfortunately, the electrochemical cell designed for this study in observance of the radiation shielding requirements at APS

diminished XAS signal return by ~70%. While there is some indication of reduced U_{60} phases present under *in situ* electrochemical reduction, this evidence is not conclusive. See Appendix C for more detail.

2.5 Conclusions

Electrochemical methods with powder microelectrodes were used to explore the unique electronic structure, properties, and kinetics of uranium-60 nanoclusters as a function of electrochemical potential. This study represents the sole electrochemical investigation of U_{60} in the literature and only the second of any uranyl peroxide nanocluster. Analysis of U_{60} in both electrochemically inert and U-containing solutions results in the observation of a two-step, one-electron reduction of U(VI) to U(IV). This is encouraging for remediation applications, as U(IV) is much less mobile than U(VI), and is therefore far less hazardous (Boyanov et al., 2011; Jeon et al., 2005; Liu et al., 2002; Scott et al., 2005). The strong oxidation-reduction couples C_1/A_1 and C_2/A_2 (Fig. 2.1 & 2.2) suggest that U(VI) in U_{60} is likely to reduce to U(IV). Low peak current for the U(IV) oxidation peak demonstrates the difficulty of re-oxidization of the species. It was found that the midpoint potentials for U redox couples correspond best with published standard electrode potentials for the pH-independent U(VI)/U(V) transition. Electrode potentials in the literature for the pH-dependent transitions of U(V)/U(IV) were much less comparable due to the lack of standards at environmentally-relevant conditions (pH 3 to 9). Results from a combined approach by means of electrochemistry and computational modeling elucidated the contribution of multiple aqueous uranyl species as a mechanistic explanation for the anomalous pH-dependence of U_{60} redox reactions. Furthermore, this multi-method approach demonstrated on an atomistic level how solution chemistry can shift redox peak position, predicting a general magnitude and direction of redox peak shift in cyclic voltammetry. Using

published standard electrode potentials in tandem with models for speciation in aqueous conditions, midpoint potentials in experimental conditions could be predicted within 23 mV.

Findings in this study also indicate the reduction of the peroxide linkers within U_{60} to hydroxide, which are then re-oxidized to peroxide, to superoxide, then finally to dioxygen. There is evidence for the ability of U_{60} to switch from a U(VI) to U(V) oxidation state with and without disruption of the cluster (and probably both at different ratios happening at the same time, depending on solution conditions, redox potential, and time of reduction). This may be due to the formation of a superoxo complex of U(V). The presence of a superoxide phase establishes U_{60} as one of the rare compounds that can stabilize a superoxo complex.

The results suggest that the U_{60} cluster is irreversibly destroyed upon reduction to U(V) due to the breaking of the bent peroxide bonds that give stability to the fullerene topology. Reduction to U(IV) results in the loss of the axial oxygens and their bonds replaced by H_2O or stabilized by OH^-. Exhaustive cycling suggests that a fraction of U_{60} is dissolved as U(IV) and the rest remains in cluster form. The insight gained from this study presents a pathway for the redox behavior and, by extension, the mobility of U_{60} in environmental conditions.

2.6 Acknowledgements

This study was funded by the Department of Energy, Office of Basic Energy Sciences, Heavy Element Chemistry Program under Grant: DE-FG02-06ER15783 and a Department of Energy Office of Science Graduate Research Program Fellowship award to Benjamin Gebarski. We thank Michigan Technological University and Christopher Stefano for natural uranium mineral samples, and Ke Yuan, Youngjae Kim, Zhongrui Li, and Mark Antonio for their invaluable comments and DOE Fellowship collaborator and Beamline Scientist Benjamin

Reinhart (ANL-APS) for his expertise in XAFS cell design, data collection, processing, and interpretation.

2.7 Appendix

A. U_{60} Structure

Figure 2.6 Illustrates the U_{60} structure, reminiscent of a traditional soccer ball.

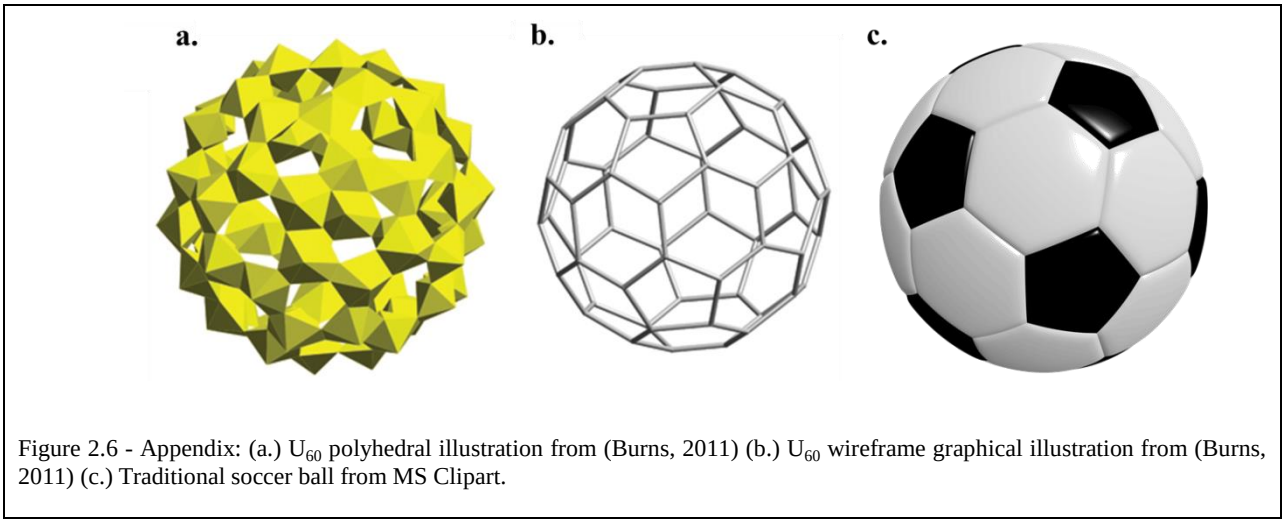

Figure 2.6 - Appendix: (a.) U_{60} polyhedral illustration from (Burns, 2011) (b.) U_{60} wireframe graphical illustration from (Burns, 2011) (c.) Traditional soccer ball from MS Clipart.

B. Computational Peak Shift

Using the well-characterized uranyl carbonate complex, it is found that the methodologies employed in this study are applicable and accurate outside of the data specific to this work.

(B1) $[UO_2(CO_3)_3]^{4-} + e^- = [UO_2(CO_3)_3]^{5-}$ E_{mid} = -0.623 V (vs. SHE)

(B2) $[UO_2(H_2O)_5]^{2+} + e^- = [UO_2(H_2O)_5]^{+}$ E_{mid} = +0.160 V (vs. SHE)

And calculate:

(B3) G^{6+}: $[UO_2(H_2O)_5]^{2+} + 3CO_3 = [UO_2(CO_3)_3]^{4-}$

(B4) G^{5+}: $[UO_2(H_2O)_5]^{+} + 3CO_3 = [UO_2(CO_3)_3]^{5-}$

Then determine:

(B5) $K^{6+} = [(UO_2(CO_3)_3)^{4-}]/[(UO_2(H_2O)_5)^{2+}(CO_3)^3]$

(B6) $K^{5+} = [(UO_2(CO_3)_3)^{5-}]/[(UO_2(H_2O)_5)^{+}(CO_3)^3]$

Then apply the following formula (equivalent to Eqn. 3, Section 2.4.4):

(B7) $-RTln(K^{6+}/K^{5+})F^{-1} = [-RTln(K^{6+}) - RTln(K^{5+})]F^{-1} = (\Delta G^{6+} - \Delta G^{5+)}F^{-1}$

$= (\text{Free E of reduction})F^{-1} = \text{Shift in } E_{mid}$

$= (-150520 \text{ J/mol})(96485 \text{ C/mol})^{-1} =$ **-1.56 V**

Equation B7 providing the shift in potential between reaction B1 & B2, between the reduction potential for free uranyl and the reduction potential of the uranyl carbonate complex. Although this calculation overestimates the -0.783 V difference between $[UO_2(H_2O)_5]$ and $[UO_2(CO_3)_3]$, it does however provide an approximation of the magnitude and direction of the peak shift in question (Morris, 2002). These findings are in alignment with those of the uncharacterized U_{60} complex in Section 2.4.4.

C. In Situ Synchrotron Electrochemical XAS

In situ electrochemical XAS refers to performing electrochemical experiments under operating conditions of the electrochemical cell, *i.e.*, under potential control. This is opposed to performing experiments *ex situ,* in the absence of potential control. Potential control preserves the electrochemical environment essential to maintain the double layer structure intact and the electron transfer reactions occurring at that particular potential at or near the electrode/electrolyte interface.

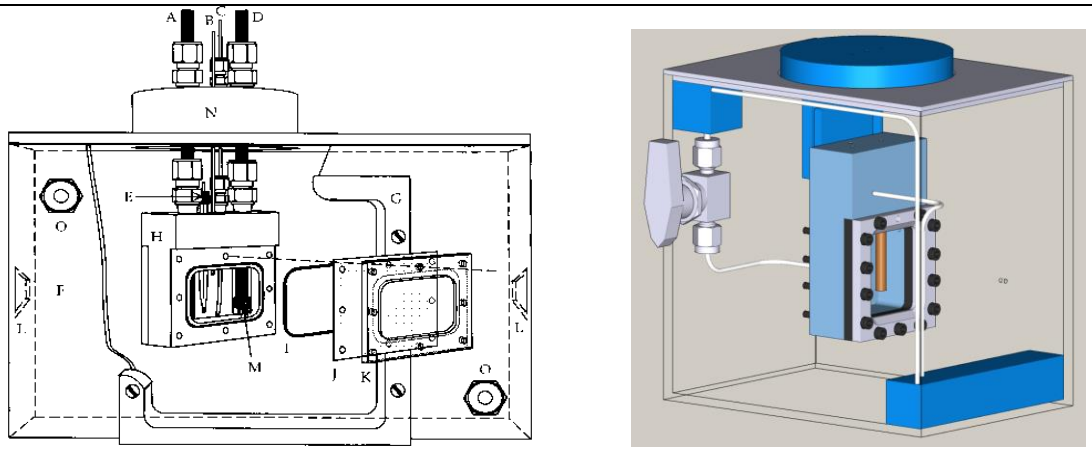

Figure 2.7 - Appendix: Cell design used for *in situ* synchrotron solid-state electrochemical x-ray absorption spectroscopy.

In situ electrochemical synchrotron XAS data was collected by running an electrochemical potential hold and collecting XAS spectra at successive voltages. By combining these runs and viewing them in relation to a CV with the same sample, voltage range, and solution; one can piece together what exactly happens to uranyl peroxides as they are electrochemically reduced and oxidized. Our work at Argonne National Lab's Advanced Photon Source began with the design of a custom *in situ* electrochemical cell with a solution injection reservoir based on a similar design from Antonio et al. (1997) (Fig. 2.7). Utilizing powder microelectrodes, and a 1 M NaCl and Na_2SO_4 solution, potential was held every 0.1 V and spectra were gathered at each potential. Unfortunately, due to the increased amount of matter in between our sample and the detector, as necessitated by ANL-APS radiation shielding requirements and the solution imperative to electrochemical experiments, all *in situ* data collected experienced a signal loss of 70% or greater, leading to noisy and uncharacteristic XAS spectra.

Despite this setback, we were able to obtain characteristic electrochemical data when using the *in situ* cell on-site and while the beam was on, eliminating several sources of error for future experiments. Upon draining the cell of solution, we found that our *ex situ* XAS spectra matched

exactly with our *ex situ* spectra prior to solution injection. Likewise, CVs collected at the beginning and end of our experiments showed very little change. This indicates that our U_{60} sample was still intact after ~9 hours of immersion in NaCl and Na_2SO_4 solution with repeated potential holds and cycling. This also shows that U_{60} does not degrade completely with repeated cycling, returning to its original stable state after induced reduction and oxidation. This supports our earlier hypothesis that some U_{60} remains intact despite exhaustive cycling.

In situ electrochemical synchrotron XAS results support our initial peak characterizations (U^{6+}) and purity of our synthetic samples in relation to natural UO_2 samples uraninite, carnotite, tyuyamunite, kasolite, and coffinite. This provides further evidence that our U_{60} and studtite are manufactured correctly and without significant variation from one batch to the next.

Analysis of U_{60} and studtite *ex situ* using XAS demonstrates the differences of the uranyl peroxide materials (nanocluster and sheet structure, respectively) despite their molecular similarities. Absorption edge (XANES) data show that in both samples uranium is in the hexavalent state U(VI) and subsequent peaks (EXAFS) denote the differences in coordination of synthetic U_{60} as compared with its natural analog, studtite (Fig. 2.8). Fourier transform rendering of R-space XAS data show the uranium interatomic distances to be shorter than literature value (4.05Å), but can be corrected by inclusion of the phase function in the Fourier transform (Fig. 2.9) (Shuller et al., 2010). The studtite sheet structure, a more densely packed uranyl structure, accounts for the increased multiple scattering effects observed in Figure 2.9.

Experimentation is currently underway at ANL-APS to reduce signal loss from shielding for *in situ* electrochemical XAS and to probe the electronic structure and adsorption properties of uranyl peroxide materials.

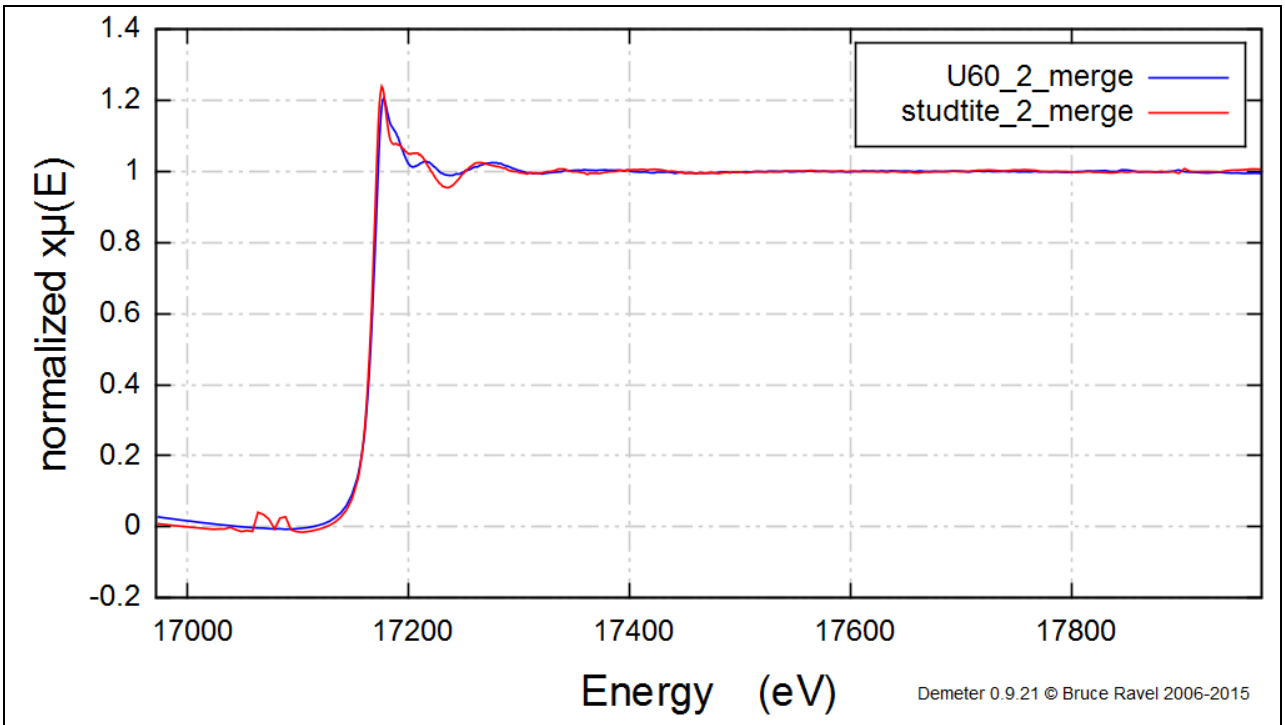

Figure 2.8 - Appendix: *Ex situ* XAS Spectra of U_{60} (blue) and studtite (red).

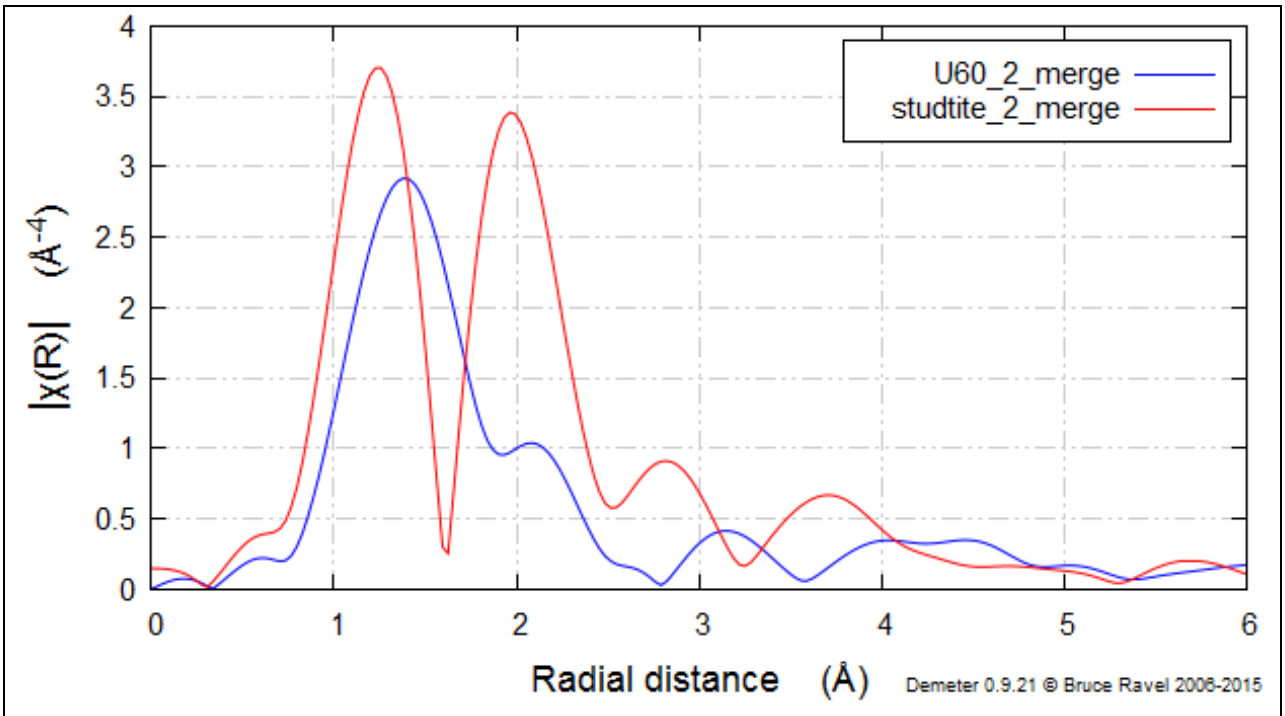

Figure 2.9 - Appendix: Fourier transform rendering of U_{60} (blue) and studtite (red) uranium R-space showing U distances and multiple scattering effects.

2.8 Works Cited

Adelani, P.O. and Albrecht-Schmitt, T.E. (2012) Thorium and uranium diphosphonates: Syntheses, structures, and spectroscopic properties. *J. Solid State Chem.* **192**, 377-384.

Antonio, M.R., Soderholm, L. and Song, I. (1997) Design of spectroelectrochemical cell for in situ X-ray absorption fine structure measurements of bulk solution species. *J. Appl. Electrochem.* **27**, 784-792.

Armstrong, C.R., Nyman, M., Shvareva, T., Sigmon, G.E., Burns, P.C. and Navrotsky, A. (2012) Uranyl peroxide enhanced nuclear fuel corrosion in seawater. *Proceedings of the National Academy of Sciences of the United States of America* **109**, 1874-1877.

Arumugam, K. and Becker, U. (2014) Computational redox potential predictions: Applications to inorganic and organic aqueous complexes, and complexes adsorbed to mineral surfaces. *Minerals* **4**, 345-387.

Austin, J.P., Sundararajan, M., Vincent, M.A. and Hillier, I.H. (2009) The geometric structures, vibrational frequencies and redox properties of the actinyl coordination complexes ($[AnO_2(L)_n]^m$; An = U, Pu, Np; L = H_2O, Cl^-, CO_3^{2-}, CH_3CO^{2-}, OH^-) in aqueous solution, studied by density functional theory methods. *Dalton Transactions*, 5902-5909.

Bard, A.J. and Faulkner, L.R. (2001) Electrochemical Methods, 2nd ed. John Wiley & Sons, USA.

Becker, U., Shuller, L., Renock, D. and Ewing, R. (2012) Comparison of computational and electrochemical approaches to determine redox reaction mechanisms of actinide complexes on mineral surfaces. *J. Am. Chem. Soc.* **243**.

Boyanov, M.I., Fletcher, K.E., Kwon, M.J., Rui, X., O'Loughlin, E.J., Loffler, F.E. and Kemner, K.M. (2011) Solution and microbial controls on the formation of reduced U(IV) species. *Environmental Science & Technology* **45**, 8336-8344.

Bratsch, S.G. (1989) Standard electrode-potentials and temperature coefficients in water at 298.15K. *J. Phys. Chem. Ref. Data* **18**, 1-21.

Bryantsev, V.S., de Jong, W.A., Cossel, K.C., Diallo, M.S., Goddard, W.A., Groenewold, G.S., Chien, W. and Van Stipdonk, M.J. (2008) Two-electron three-centered bond in side-on (η^2) uranyl(V) superoxo complexes. *J. Phys. Chem. A* **112**, 5777-5780.

Buhl, M. and Kabrede, H. (2006) Mechanism of water exchange in aqueous uranyl(VI) ion. A density functional molecular dynamics study. *Inorg. Chem.* **45**, 3834-3836.

Buhl, M., Kabrede, H., Diss, R. and Wipff, G. (2006) Effect of hydration on coordination properties of uranyl(VI) complexes. A first-principles molecular dynamics study. *J. Am. Chem. Soc.* **128**, 6357-6368.

Burns, P.C. (2005) U^{6+} minerals and inorganic compounds: Insights into an expanded structural hierarchy of crystal structures. *Can. Mineral.* **43**, 1839-1894.

Burns, P.C. (2011) Nanoscale uranium-based cage clusters inspired by uranium mineralogy. *Mineralogical Magazine* **75**, 1-25.

Burns, P.C., Ewing, R.C. and Miller, M.L. (1997) Incorporation mechanisms of actinide elements into the structures of U^{6+} phases formed during the oxidation of spent nuclear fuel. *J. Nucl. Mater.* **245**, 1-9.

Burns, P.C., Ewing, R.C. and Navrotsky, A. (2012) Nuclear fuel in a reactor accident. *Science* **335**, 1184-1188.

Burns, P.C., Kubatko, K.A., Sigmon, G., Fryer, B.J., Gagnon, J.E., Antonio, M.R. and Soderholm, L. (2005) Actinyl peroxide nanospheres. *Angewandte Chemie-International Edition* **44**, 2135-2139.

Cachet-Vivier, C., Vivier, V., Cha, C.S., Nedelec, J.Y. and Yu, L.T. (2001) Electrochemistry of powder material studied by means of the cavity microelectrode (CME). *Electrochim. Acta* **47**, 181-189.

Cha, C.S., Li, C.M., Yang, H.X. and Liu, P.F. (1994) Powder Microelectrodes. *J. Electroanal. Chem.* **368**, 47-54.

Choppin, G.R. (2007) Actinide speciation in the environment. *J. Radioanal. Nucl. Chem.* **273**, 695-703.

Debets, P.C. (1963) X-ray diffraction data on hydrated uranium peroxide. *Journal of Inorganic & Nuclear Chemistry* **25**, 727-730.

Delley, B. (1990) An all-electron numerical method for solving the local density functional for polyatomic molecules. *J. Chem. Phys.* **92**, 508-517.

Dickman, M.H. and Pope, M.T. (1994) Peroxo and superoxo complexes of chromium, molybdenum, and tungsten. *Chem. Rev.* **94**, 569-584.

Dolg, M., Wedig, U., Stoll, H. and Preuss, H. (1987) Energy-adjusted ab initio pseudopotentials for the first row transition elements. *J. Chem. Phys.*, 866-872.

Finch, R.J. and Ewing, R.C. (1992) The corrosion of uraninite under oxidizing conditions. *J. Nucl. Mater.* **190**, 133-156.

Flynn, S.L., Szymanowski, J.E.S., Gao, Y.Y., Liu, T.B., Burns, P.C. and Fein, J.B. (2015) Experimental measurements of U_{60} nanocluster stability in aqueous solution. *Geochim. Cosmochim. Acta* **156**, 94-105.

Furuya, Y., Mashio, T., Ohma, A., Tian, M., Kaveh, F., Beauchemin, D. and Jerkiewicz, G. (2015) Influence of electrolyte composition and pH on platinum electrochemical and/or chemical dissolution in aqueous acidic media. *Acs Catalysis* **5**, 2605-2614.

Gagliardi, L., Vlaisavljevich, B., Ramirez, P.M., Cramer, C.J. and Burns, P.C. (2013) Ab initio and classical simulations modeling of uranyl peroxide nanoclusters. *J. Am. Chem. Soc.* **246**.

Gil, A., Karhanek, D., Miro, P., Antonio, M.R., Nyman, M. and Bo, C. (2012) A journey inside the U_{28} nanocapsule. *Chemistry-a European Journal* **18**, 8340-8346.

Giridhar, P., Venkatesan, K.A., Srinivasan, T.G. and Rao, P.R.V. (2007) Electrochemical behavior of uranium(VI) in 1-butyl-3-methylimidazolium chloride and thermal characterization of uranium oxide deposit. *Electrochim. Acta* **52**, 3006-3012.

Giridhar, P., Venkatesan, K.A., Subramaniam, S., Srinivasan, T.G. and Rao, R.R.V. (2006) Electrochemical behavior of uranium(VI) in 1-butyl-3-methylimidazolium chloride and in 0.05 M aliquat-336/chloroform. *Radiochimica Acta* **94**, 415-420.

Goldik, J.S., Noel, J.J. and Shoesmith, D.W. (2005) The electrochemical reduction of hydrogen peroxide on uranium dioxide electrodes in alkaline solution. *J. Electroanal. Chem.* **582**, 241-248.

Gutowski, K.E. and Dixon, D.A. (2006) Predicting the energy of the water exchange reaction and free energy of solvation for the uranyl ion in aqueous solution. *J. Phys. Chem. A* **110**, 8840-8856.

Hardwick, H.C., Royal, D.S., Helliwell, M., Pope, S.J.A., Ashton, L., Goodacre, R. and Sharrad, C.A. (2011) Structural, spectroscopic and redox properties of uranyl complexes with a maleonitrile containing ligand. *Dalton Transactions* **40**, 5939-5952.

Hay, P.J., Martin, R.L. and Schreckenbach, G. (2000) Theoretical studies of the properties and solution chemistry of AnO_2^{2+} and AnO_2^{+} aquo complexes for An = U, Np, and Pu. *J. Phys. Chem. A* **104**, 6259-6270.

Hill, D.L., Perano, J. and Osteryoung, R.A. (1960) An electrochemical study of uranium in fused chlorides. *J. Electrochem. Soc.* **107**, 698-705.

Hixon, A.E., Arai, Y. and Powell, B.A. (2013) Examination of the effect of alpha radiolysis on plutonium(V) sorption to quartz using multiple plutonium isotopes. *J. Colloid Interface Sci.* **403**, 105-112.

Jegou, C., Gennisson, M., Peuget, S., Desgranges, L., Guimbretiere, G., Magnin, M., Talip, Z. and Simon, P. (2015) Raman micro-spectroscopy of UOX and MOX spent nuclear fuel characterization and oxidation resistance of the high burn-up structure. *J. Nucl. Mater.* **458**, 343-349.

Jeon, B.H., Dempsey, B.A., Burgos, W.D., Barnett, M.O. and Roden, E.E. (2005) Chemical reduction of U(VI) by Fe(II) at the solid-water interface using natural and synthetic Fe(III) oxides. *Environmental Science & Technology* **39**, 5642-5649.

Klamt, A. and Schuurmann, G. (1993) Cosmo - a new approach to dielectric screening in solvents with explicit expressions for the screening energy and its gradient. *Journal of the Chemical Society-Perkin Transactions 2*, 799-805.

Kong, X.J., Long, L.S., Zheng, Z.P., Huang, R.B. and Zheng, L.S. (2010) Keeping the Ball Rolling: Fullerene-like Molecular Clusters. *Acc. Chem. Res.* **43**, 201-209.

Langmuir, D. (1978) Uranium solution-mineral equilibria at low temperatures with applications to sedimentary ore deposits. *Geochim. Cosmochim. Acta* **42**, 547-569.

Li, C.M. and Cha, C.S. (1988) Powder microelectrodes I. Reversible systems. *Acta Physico-Chimica Sinica* **4**, 167-171.

Ling, J., Qiu, J. and Burns, P.C. (2012) Uranyl peroxide oxalate cage and core-shell clusters containing 50 and 120 uranyl ions. *Inorg. Chem.* **51**, 2403-2408.

Ling, J., Qiu, J., Sigmon, G.E., Ward, M., Szymanowski, J.E.S. and Burns, P.C. (2010) Uranium Pyrophosphate/Methylenediphosphonate Polyoxometalate Cage Clusters. *J. Am. Chem. Soc.* **132**, 13395-13402.

Liu, C.X., Gorby, Y.A., Zachara, J.M., Fredrickson, J.K. and Brown, C.F. (2002) Reduction kinetics of Fe(III), Co(III), U(VI) Cr(VI) and Tc(VII) in cultures of dissimilatory metal-reducing bacteria. *Biotechnol. Bioeng.* **80**, 637-649.

Locatelli, C., Minguzzi, A., Vertova, A., Cava, P. and Rondinini, S. (2011) Quantitative studies on electrode material properties by means of the cavity microelectrode. *Anal. Chem.* **83**, 2819-2823.

Lutze, W. and Ewing, R.C. (1988) Radioactive waste forms for the future. North-Holland ;Sole distributors for the USA and Canada, Elsevier Science Pub. Co., Amsterdam ; New York, N.Y., U.S.A.

Mallon, C., Walshe, A., Forster, R.J., Keyes, T.E. and Baker, R.J. (2012) Physical characterization and reactivity of the uranyl peroxide $UO_2(\eta^2\text{-}O_2)(H_2O)_2 \cdot 2H_2O$: Implications for storage of spent nuclear fuels. *Inorg. Chem.* **51**, 8509-8515.

Manfredi, C., Caruso, V., Vasca, E., Vero, S., Ventimiglia, E., Palladino, G. and Ferri, D. (2006) On the hydrolysis of the tetravalent uranium ion U^{4+}. *J. Solution Chem.* **35**, 927-937.

Martinot, L., Laeckmann, D., Lopes, L., Materne, T. and Muller, V. (1992) Contribution to the knowledge of the electrochemical properties of actinides in nonaqueous media 2: The reduction of hexavalent uranium in various organic-solvents. *J. Alloys Compd.* **185**, 151-162.

Morris, D.E. (2002) Redox energetics and kinetics of uranyl coordination complexes in aqueous solution. *Inorg. Chem.* **41**, 3542-3547.

Murakami, T., Ohnuki, T., Isobe, H. and Sato, T. (1997) Mobility of uranium during weathering. *Am. Mineral.* **82**, 888-899.

Nicholson, R.S. (1965) Theory and application of cyclic voltammetry for measurement of electrode reaction kinetics. *Anal. Chem.* **37**, 1351+.

Nurmi, J.T. and Tratnyek, P.G. (2011) Electrochemistry of natural organic matter. *Aquatic Redox Chemistry* **1071**, 129-151.

Nyman, M. and Burns, P.C. (2012) A comprehensive comparison of transition-metal and actinyl polyoxometalates. *Chem. Soc. Rev.* **41**, 7354-7367.

Qiu, J. and Burns, P.C. (2013) Clusters of actinides with oxide, peroxide, or hydroxide bridges. *Chem. Rev.* **113**, 1097-1120.

Renock, D., Mueller, M., Yuan, K., Ewing, R.C. and Becker, U. (2013) The energetics and kinetics of uranyl reduction on pyrite, hematite, and magnetite surfaces: A powder microelectrode study. *Geochim. Cosmochim. Acta* **118**, 56-71.

Savitzky, A. and Golay, M.J.E. (1964) Smoothing & differentiation of data by simplified least squares procedures. *Anal. Chem.* **36**, 1627-&.

Scott, T.B., Allen, G.C., Heard, P.J. and Randell, M.G. (2005) Reduction of U(VI) to U(IV) on the surface of magnetite. *Geochim. Cosmochim. Acta* **69**, 5639-5646.

Shuller, L., Renock, D., Rak, Z., Fernando, S., Dzulkifli, I., Ewing, R. and Becker, U. (2011) Actinide adsorption onto mineral surfaces: A quantum-mechanical investigation. *J. Am. Chem. Soc.* **242**.

Shuller, L.C., Ewing, R.C. and Becker, U. (2010) Quantum-mechanical evaluation of Np-incorporation into studtite. *Am. Mineral.* **95**, 1151-1160.

Sigmon, G.E., Ling, J., Unruh, D.K., Moore-Shay, L., Ward, M., Weaver, B. and Burns, P.C. (2009a) Uranyl-peroxide interactions favor nanocluster self-assembly. *J. Am. Chem. Soc.* **131**, 16648.

Sigmon, G.E., Unruh, D.K., Ling, J., Weaver, B., Ward, M., Pressprich, L., Simonetti, A. and Burns, P.C. (2009b) Symmetry versus minimal pentagonal adjacencies in uranium-based polyoxometalate fullerene topologies. *Angewandte Chemie-International Edition* **48**, 2737-2740.

Springell, R., Rennie, S., Costelle, L., Darnbrough, J., Stitt, C., Cocklin, E., Lucas, C., Burrows, R., Sims, H., Wermeille, D., Rawle, J., Nicklin, C., Nuttall, W., Scott, T. and Lander, G. (2015) Water corrosion of spent nuclear fuel: radiolysis driven dissolution at the UO_2/water interface. *Faraday Discuss.* **180**, 301-311.

Steele, H. and Taylor, R.J. (2007) A theoretical study of the inner-sphere disproportionation reaction mechanism of the pentavalent actinyl ions. *Inorg. Chem.* **46**, 6311-6318.

Stefanovsky, S.V., Myasoedov, B.F., Remizov, M.B. and Belanova, E.A. (2014) IR and Raman spectroscopy of sodium-aluminophosphate glasses for immobilizing high-level wastes from spent nuclear fuel reprocessing. *J. Appl. Spectrosc.* **81**, 618-623.

Topin, S. and Aupiais, J. (2016) The pentavalent actinide solution chemistry in the environment. *Journal of Environmental Radioactivity* **153**, 237-244.

Vivier, V., Cachet-Vivier, C., Wu, B.L., Cha, C.S., Nedelec, J.Y. and Yu, L.T. (1999) Cavity microelectrode for studying powder materials at a high potential scan rate. *Electrochemical and Solid State Letters* **2**, 385-387.

Vlaisavljevich, B., Gagliardi, L. and Burns, P.C. (2010) Understanding the structure and formation of uranyl peroxide nanoclusters by quantum chemical calculations. *J. Am. Chem. Soc.* **132**, 14503-14508.

Wang, Q., Cha, C.S., Lu, J.T. and Zhuang, L. (2009) The electrochemistry of "solid/water" interfaces involved in PEM-H_2O reactors Part I. The "Pt/water" interfaces. *PCCP* **11**, 679-687.

Wang, Z.Q., Tada, E. and Nishikata, A. (2016) Communication-platinum dissolution in alkaline electrolytes. *J. Electrochem. Soc.* **163**, C853-C855.

Wylie, E.M., Peruski, K.M., Weidman, J.L., Phillip, W.A. and Burns, P.C. (2014) Ultrafiltration of uranyl peroxide nanoclusters for the separation of uranium from aqueous solution. *ACS Applied Materials & Interfaces* **6**, 473-479.

Xu, L.C., Wang, Y.X., Lu, J.W., Lu, X.S., Liu, Y.C. and Liu, X.Y. (2002) Radioactive contamination of the environment as a result of uranium production: a case study at the abandoned Lincang uranium mine, Yunnan Province, China. *Science in China Series B-Chemistry* **45**, 11-19.

Yuan, K., Ilton, E.S., Antonio, M.R., Li, Z.R., Cook, P.J. and Becker, U. (2015a) Electrochemical and spectroscopic evidence on the one-electron reduction of U(VI) to U(V) on magnetite. *Environmental Science & Technology* **49**, 6206-6213.

Yuan, K., Renock, D., Ewing, R.C. and Becker, U. (2015b) Uranium reduction on magnetite: Probing for pentavalent uranium using electrochemical methods. *Geochim. Cosmochim. Acta* **156**, 194-206.

CHAPTER 3

Surface-Mediated Reactions of Uranyl Peroxide Materials U_{60} and Studtite at the Mineral-Electrolyte Interface

- Ben Gebarski and Udo Becker -

Department of Earth and Environmental Sciences, University of Michigan, 2534 C.C. Little Building, 1100 North University Avenue, Ann Arbor, MI 48109-1005, USA

3.1 Abstract

The synthetic uranyl peroxide U_{60} ($Li_{40}K_{20}[UO_2(O_2)(OH)]_{60}(H_2O)_{214}$) and its natural analog, the mineral studtite $(UO_2)O_2(H_2O)_2{\cdot}(H_2O)_2$, are composed of hexavalent uranium molecular building blocks. These U(VI) bearing phases are highly toxic and readily mobile contaminants that can enter the environment through the spent nuclear fuel cycle, spills, or reactor accidents. In reducing conditions, U(VI) can be reduced to its less toxic and less mobile insoluble form, U(IV). However, the redox behavior, stability, and the influence of surface catalysis and their effect on uranyl peroxide mobility within the environment are unknown. In this study, we investigate the interaction, reduction, and adsorption behavior of hexavalent uranyl peroxide materials on substrate surfaces using electrochemical atomic force microscopy (EC-AFM). This method allows for the control of redox potential at the substrate surface, and U adsorption is imaged over time as a function of both potential and solution pH. Analysis of surface adsorbates is carried out using high-resolution scanning electron microscopy (SEM) and auger electron spectroscopy (AES). Results suggest the growth of U_{60} nanoparticles both as a crystalline solid (FCC structure) and as composite clusters, which likely serve as nucleation sites for crystalline

growth. AES analysis provides direct evidence of U_{60} sorbates at the substrate surface through the derivation of a sensitivity factor based on a crystalline U_{60} standard. Using this factor in tandem with the U/K relative ratio from AES spectra, any sorbate containing U_{60} fullerenes can be identified. The growth of ~10 nm uranium oxide needles suggests that some of the U_{60} clusters are dissociating into their constituent monomeric aqueous species. These sorbates exhibit Ostwald ripening, observed as an increase in sorbate volume and decrease in sorbate number over time. Highly oxidizing (+1000 mV) potentials yield few sorbates and highly reducing (-1000 mV) potentials destroy sample surfaces. U_{60} sorbate formation is favored in weakly (-500 mV) reducing conditions.

3.2 Introduction

Since its first synthesis in 2005, the physicochemical properties of the uranium-60 nanocluster (U_{60}), such as its redox behavior compared to the reduction of dissolved uranyl, the stability under different pe-pH conditions, or the adsorption/reduction of the clusters on different mineral surfaces and environmental conditions, have yet to be characterized (Burns, 2005). U_{60} nanoclusters ($Li_{40}K_{20}[UO_2(O_2)(OH)]_{60}(H_2O)_{214}$) consist of a network of U atoms adopting the same topology as C_{60} Buckminster fullerenes ("buckyballs"); they contain 60 linear $(UO_2)_2^+$ uranyl ion units with the two uranyl O atoms pointing radially towards and away from the center of the cluster and with peroxide bonds connecting two adjacent uranium atoms along the surface of the buckyball (Kroto et al., 1985). Clusters contain hexagonal rings of O atoms with uranyl groups in the center and peroxide groups at the "seam" between two hexagons. In addition, there are pentagonal rings and the "seam" between a hexagon and pentagon is formed by two hydroxyl groups. The U-O_2-U dihedral angles are bent the same way, *i.e.*, about the center of the cluster. This topology results in clusters built entirely from uranyl hexagonal bipyramids, each connected

to three others, with a net negative charge balanced by the presence of Li^+ and K^+ counter cations (Sigmon et al., 2009b).

Peroxide bonds connecting metal cations are only observed in one naturally-occurring mineral, studtite (here, consecutive peroxide bonds are bent back and forth, resulting in an overall linear "corrugated" array of uranyl building blocks). Studtite, $(UO_2)O_2(H_2O)_2 \cdot 2(H_2O)$, the hydrate of metastudtite, $(UO_2)O_2(H_2O)_2$, is found primarily as a phase alteration product in the presence of uranium, either in mines or nuclear waste repositories; the peroxide is formed via the α-radiolysis of water during formation (Hixon et al., 2013; Ling et al., 2012; Mallon et al., 2012; Sigmon et al., 2009a; Sigmon et al., 2009b). Computational investigations into the structure and bonding of studtite attest to the bent peroxide bonds which aid in the self-assembly of large cage clusters in similar conditions (Gagliardi et al., 2013; Vlaisavljevich et al., 2010).

The behavior of such novel actinide compounds is of particular interest due to their unique molecular configuration and the numerous environmental and health hazards they pose. Uranyl peroxide materials are primarily composed of U(VI) building blocks, which pose a threat not only due to their radioactivity, but also due to their high solubility (Flynn et al., 2013; Flynn et al., 2015). In aqueous environments, the more soluble compounds are the most likely to remain in solution the longest, therefore transporting any potential hazards far from their point of origin. However, if U(VI) compounds can be reduced to a lower oxidation state, such as U(IV), their solubility and therefore relative mobility within the environment can be greatly diminished (Arumugam and Becker, 2014; Becker et al., 2012; Finch and Ewing, 1992; Lutze and Ewing, 1988; Murakami et al., 1997; Shuller et al., 2011; Xu et al., 2002; Yuan et al., 2015b). However, it remains unknown whether reduction is a viable method for uranyl peroxide immobilization within the environment.

In spite of their scarcity, the source for such potential contamination is not limited to laboratories that utilize uranyl peroxide materials. It has been found that studtite has the potential to form wherever radioactive material and water are present, such as uranium ore deposits, mines, and waste casks (Mallon et al., 2012; Sigmon et al., 2009a). Despite the fact that no uranyl peroxide cage-like structure has ever been found in nature, it has been postulated that they are likely to self-assemble under certain conditions, such as the introduction of seawater to exposed nuclear fuel rods during the Fukushima reactor accident (Armstrong et al., 2012; Burns et al., 2012).

Thus, for the remediation and sequestration of such uranium compounds, an understanding of the redox transformations between U(VI) and U(IV) is essential. Despite the abundance of electron donors in natural aqueous systems, such as compounds containing the Fe(II) ion, the interaction with a substrate surface is often essential for reduction to occur. Minerals commonly present in aqueous environments, like sulfides and oxides have been shown to be vital to these redox processes through surface-mediated reduction. Such surfaces can assist redox reactions in a number of ways: they can accept or donate electrons, serve as a catalyst through the shuttling of electrons, or provide adsorption or nucleation sites thereby lowering the activation energy (Becker et al., 2001; Rosso and Becker, 2003; Tessis et al., 1999; Vorlicek and Helz, 2002).

Despite numerous studies demonstrating the catalysis of uranium reduction via the interaction with substrate surfaces, little is known about the nanoscale processes occurring at the mineral-fluid interface (Elsner et al., 2004; Gheju, 2011; Hyland and Bancroft, 1990; Taylor et al., 2015). Still less is known about the solution characteristics and redox behavior of uranyl peroxide clusters both in solution and adsorbed to substrate surfaces. Such information is vital to

predicting cluster mobility within the environment. Thus we find that high-resolution surface-sensitive microscopy and spectroscopy is required to probe these nanoscale processes.

This study utilizes a combination of atomic force microscopy (AFM) with electrochemical methods (EC-AFM) to observe the formation of reduction products on substrate surfaces as a function of solution chemistry and redox potential. Solution chemistry is controlled via pH, background electrolyte, and concentration of U_{60} clusters in solution. Solution redox potential is controlled by means of a potentiostat applying a set voltage to the working electrode (substrate surface) for a given duration of time. This methodology allows for *in situ* observations of reactions at a given Eh and pH such that can be mapped by an Eh-pH (Pourbaix) diagram (Fig. 3.1). This technique has been utilized successfully to analyze epitaxial mineral growth, mineral dissolution, reaction kinetics, precipitation, adsorption, thin film formation, and electron transfer (Etienne et al., 2004; Higgins and Hamers, 1995, 1996; Higgins et al., 1996; Stack, 2008; Stack et al., 2004a; Stack et al., 2004b; Wigginton et al., 2009).

Utilizing EC-AFM techniques, this research is a feasibility study to determine if the adsorption, precipitation, and reduction of U_{60} *in situ* can be observed as the substrate surface is electrochemically polarized. In order to provide the best possible conditions for the formation of sorbates, the surface chosen was steel. Steel is an alloy of Fe and several other elements in low concentrations (< 1%) that forms a Body-Centered Cubic (BCC) crystalline structure at standard temperatures and pressures. The interactions between uranium and steel are of the first importance due to its presence in the nuclear fuel cycle in piping, containment vessels, and storage. As a catalytically-active metal and conductor, steel surfaces are both highly conductive and redox active, forming passivation layers even in the absence of electrochemically-driven reduction or oxidation. As such, we find that steel surfaces provide ideal substrates for the

extensive adsorption of uranyl peroxide clusters, generating greater quantities of sorbates for later spectroscopic analysis. Furthermore, it has been shown that Fe oxide substrates are an effective catalyst for the reduction of U(VI) in comparison to other surfaces such as micas (Ilton et al., 2004; Renock and Becker, 2010; Taylor et al., 2017; Taylor et al., 2015; Yuan et al., 2015a).

The objective of this research is to determine the qualitative and quantitative behavior of U_{60} cluster reduction and adsorption onto crystalline surfaces at specific Eh and pH conditions. To do this, a crystalline surface (steel) is inserted into an EC-AFM cell and electrochemically polarized at varied potentials in a U_{60} cluster-containing solution. Adsorption behavior and kinetic information are measured via growth of adsorbates over time and the number of adsorbates or adsorbate coverage per unit area in relation to time. Eh-pH diagrams (Fig. 3.1) are used to help characterize the species present at particular pH and Eh. Through AFM imaging, we identified growth features over time (volume, symmetry, height, growth face, etc.) and interpreted the reaction process. This morphological and kinetic information is combined with findings from surface sensitive spectroscopic methods SEM and AES to view the resultant mineral surfaces with greater resolution *ex situ* and determine the composition and oxidation state of adsorbates. These findings will help to further knowledge of the behavior of uranyl peroxide clusters in environmental conditions.

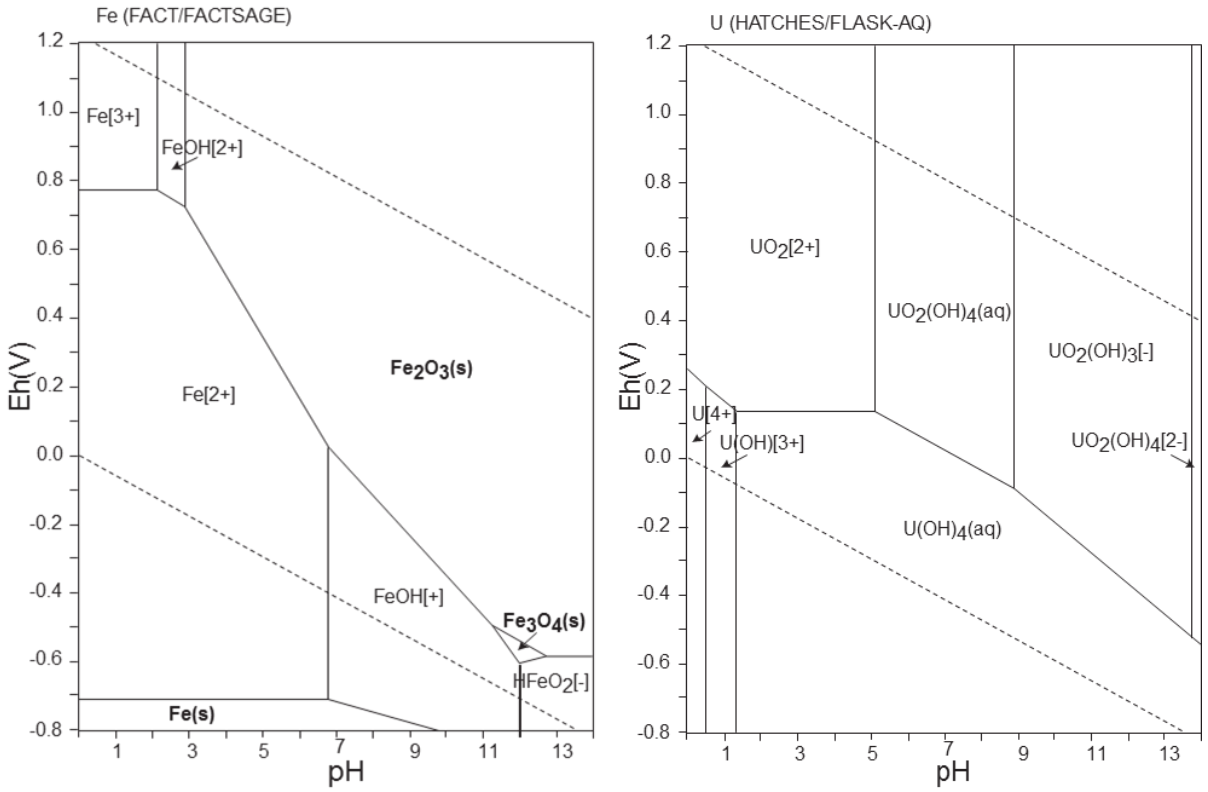

Figure 3.1: Eh-pH (speciation) diagrams predict the species and oxidation state present as a function of redox potential and pH in reference to both environmentally-relevant and repository conditions (Choppin, 2007). Eh-pH diagram for Fe (left) shows $FeOH^+$ (green rust) phase is expected for reducing conditions at pH 10.8. This is confirmed by observation of green rust at the steel surface. Eh-pH diagram for U (right) predicts a U(IV) phase at similar conditions. This is confirmed by observation of U_{60} clusters at the substrate surface.

3.3 Materials and Methods

3.3.1 Electrochemical Atomic Force Microscopy (AFM)

Surfaces used in this study are all cut from the same contiguous plate of 3/32 inch (2.4 mm) mild steel. Cut samples were then polished with increasingly fine silicon carbide sandpaper from 180-4000 grit. Samples were then further polished with 0.3 µm and 0.05 µm alumina powders, then rinsed and sonicated to remove polishing contaminants. All surfaces were prepared to approximate dimensions of 10×10×2.5 mm.

Experimentation was performed with a three-electrode electrochemical cell, with the mineral surface serving as the working electrode, a platinum wire as the counter electrode, and a silver

wire as the reference electrode (+250 mV vs. the standard hydrogen electrode, SHE). Mineral surfaces were glued to etched Teflon® discs using Torr Seal® low vapor pressure epoxy and loaded into the base of the AFM fluid cell described in Appendix A. Redox potential was controlled using a CHI 760D potentiostat integrated with a Bruker Dimension Icon Atomic Force Microscope. All solutions were prepared using Milli-Q® ultra-pure water and reagents available from Fisher-Scientific. U_{60} nanoclusters and studtite were prepared according to the literature (Debets, 1963; Mallon et al., 2012; Sigmon et al., 2009b) and crystallized from solution. Natural U^{238} was used in preparation of these samples and throughout the course of this study. U^{238} is an α-emitter and all experiments were carried out in laboratories designed for the use of radioactive materials. Initial pH of uranyl solutions was 10.6 and was adjusted using 0.01 M HCl and 0.01 M KOH.

AFM experiments were performed in Contact and Peak Force Tapping (PFT) modes, both in and out of fluid. PFT is an exclusive Bruker AFM operation mode much like a conventional Tapping mode wherein the probe tip makes oscillatory contact with the sample. However, PFT mode has the advantage of cantilever oscillations well below their resonant frequency, thereby removing many artifacts related to resonation. AFM probes used were Bruker ScanAsyst-Fluid+ (nominal frequency: 150 kHz, nominal spring constant: 0.7 N/m) with silicon tips. Scan rates of about 1.0 Hz with resolutions of 512 samples per line were used for all image captures. An open circuit potential (OCP) of 0-100 mV was observed for each experiment and allowed to stabilize for 300 seconds prior to electrochemical potential holds. All images were processed using Bruker NanoScope Analysis® software version 1.4. After AFM experimentation, mineral surfaces were removed from the EC-AFM cell, and dried in a Coy® vinyl glove box containing an atmosphere of 95% N_2 and 5% H_2 with O_2 levels less than 1 ppm using a desiccant with a palladium catalyst

and an O_2 trap (Taylor et al., 2015). All AFM and spectroscopic experiments were carried out at a temperature of 22 ± 2 °C in-house at the University of Michigan.

3.3.2 Scanning Electron Microscopy (SEM)

SEM and energy dispersive spectroscopy (EDS) was utilized to evaluate reaction products and/or changes in morphology on the sample surfaces. Steel surface electrodes were first polarized, sorbates were given time to form, then surfaces were removed from solution and washed with deoxygenated Milli-Q water to remove any soluble species existing on the sample surface. These samples were then dried in a Coy® vinyl glove box containing an atmosphere of 95% N_2 and 5% H_2 with O_2 levels less than 1 ppm using a desiccant with a palladium catalyst and an O_2 trap (Taylor et al., 2015). SEM and EDS was performed using a JEOL-7800FLV Field Emission SEM and a FEI Helios 650 Nanolab SEM. EDS data was collected with an integrated Oxford Instruments X-Max detector and the AztecEnergy software package (Version 3.1) was used for analysis and processing.

3.3.3 Auger Electron Spectroscopy (AES)

AES, a surface sensitive technique for measuring atomic composition with high resolution, was performed using a Physical Electronics Auger Nanoprobe 680. The electron beam used to initiate the Auger process was an integrated Schottky thermal field emission gun run at a beam voltage of between 5 and 10 keV and a current of 5 to 20 nA. Under these conditions, the analysis depth (or excitation depth) is 1 to 2 Å and the spatial resolution is between 100 and 1000 Å. The electron energy analyzer used includes a full cylindrical mirror analyzer with a capture angle 42° ± 6° for 360° about the analyzer axis. Analysis was performed under ultra-high vacuum (ca. $2.0 \cdot 10^{-9}$ Torr) conditions. More insulating samples were affixed to 30°-tilt sample mounts (Physical Electronics) to counteract incident electron beam charge accumulation on the

surface causing shifts in electron kinetic energy. By tilting the sample, fewer electrons from the incident beam interact with the surface resulting in a smaller number of Auger electrons striking the detector. The Multipak software package (version 9.6.0 ULVAC-PHI 2014) was used to analyze, smooth, and differentiate collected spectra.

3.4 Results

3.4.1 Electrochemical AFM

In order to investigate the feasibility of U_{60} sorption on substrate surfaces, a solution pH must be chosen that is representative of the expected uranium redox behavior as predicted by the Eh-pH diagram in Figure 3.1. Furthermore, the pH chosen must be within the stability range of the analyte, as sorbates must remain for an extended period of time and not dissolve before or during imaging. U_{60} nanoclusters have been shown to be stable over a broad pH range, even when undersaturated, but they are most stable from pH 9-11 (Flynn et al., 2013; Flynn et al., 2015). At the solution pH chosen for this study, pH 11, the predominant oxidized phase of U(VI) expected is $UO_2(OH)_3^-$ (Figure 3.1). The phase expected at reducing potentials is $U(OH)_{4(aq)}$ at all pH levels above pH 1. These solution conditions were chosen to best elucidate the dependency of observed sorbates and/or reduction products to the most likely pH, Eh, and phase.

In order to provide a background image of the substrate prior to the application of an electrochemical potential, steel surfaces were first imaged in air and then in fluid at open circuit potential (OCP, Figure 3.2A & B). Background images are then compared with any observed growth features as a function of time, potential, and solution chemistry. Images in Figure 3.2 show parallel scratch marks that form as a result of the polishing process or surface irregularity and serve as reference points for comparison. The steel surface electrodes were then polarized at specific electrochemical potentials (-1000, -500, +500, and +1000 mV) for periods of

1000 seconds or more, and then the surface was imaged extensively. Images were analyzed and quantified for any changes, including the number and size of adsorbates and/or precipitates (referred to in this study as sorbates). Although our analysis provides quantitative values, *e.g.*, adsorbate volumes, less than 10% of our surfaces were imaged for any given sample and an assumption is made that the scanned surface areas are representative of the entire sample. As such, overall trends and relative differences between potentials and solution chemistries are emphasized rather than that of absolute values.

In air, steel surfaces exhibit no sorbates and no change with repeated scanning, demonstrating the robustness of the sample (Figure 3.2A). For experiments in fluids, a 1 M KCl solution was used first, in order to provide a comparison fluid scan for the later use of uranyl peroxide (U_{60}) solutions. At OCP, small (~10 nm) sorbates begin to appear with the characteristic isometric cubic structure of sylvite (KCl) (Figure 3.2B). To verify that sorbate shape was not due to AFM tip convolution/artifacts, the scan angle was rotated by 45° for every image obtained. Observed shape was found to maintain its original orientation despite a change in scan angle, thus the shape reflects the true morphology of the sorbate. After 28 min, sorbates had grown as large as 0.018 μm^2 with diameters of ~150 nm. As expected from the Eh-pH diagram for a 1 M KCl system (Fig. 3.3), highly oxidizing and reducing potentials (+1000/-1000 mV) result in the dissolution of sylvite sorbates. In the case of highly reducing potentials, dissolution of sorbates was followed by the breakdown of the uppermost layers of the surface as shown in the development of 2.3 µm diameter, 80 nm deep pits in the sample surface, an increase in relative height of analysis area, loss of surface features, and observation of green oxidized iron particulates in the formerly colorless solution immediately following polarization (Figure 3.2C). Weakly oxidizing or reducing potentials (+500/-500 mV) appear to have a

negligible effect on the growth of these crystals vs. growth at OCP, but minute changes in sorbate behavior is difficult to measure given the slow erosion of sorbed species due to physical contact with the AFM tip. Such destructive analysis by the tip is evidenced by successive rastered images decreasing in overall height over time.

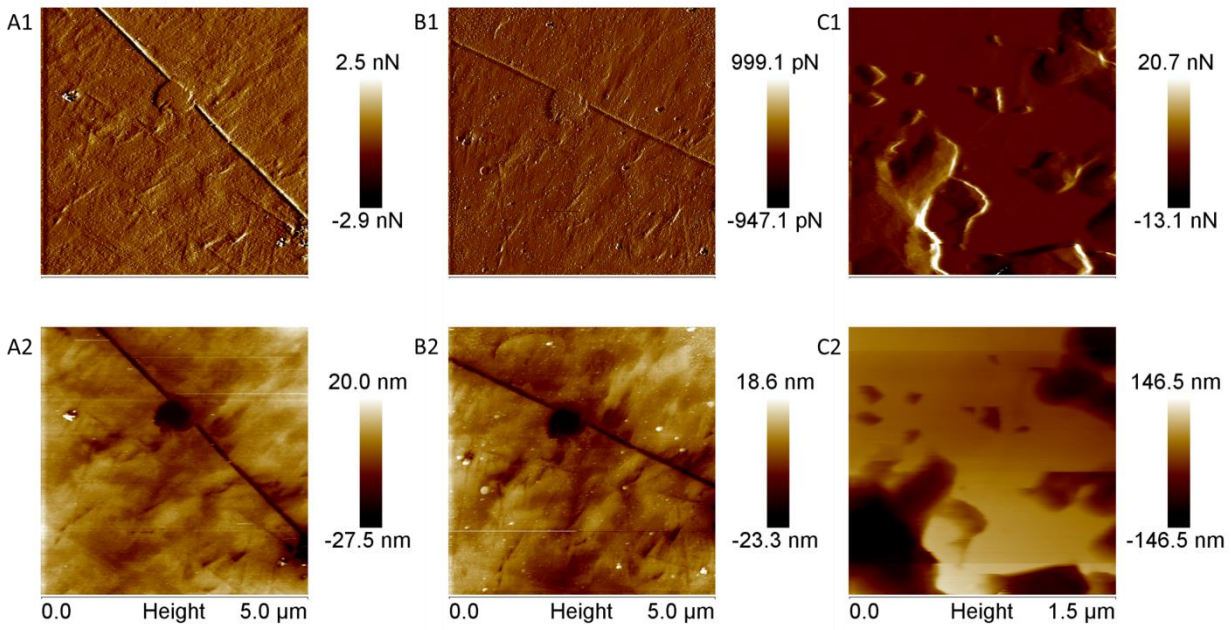

Figure 3.2: AFM image of a steel surface in 1 M KCl solution at pH 10.8 **(1)** EC-AFM peak force error (PFE). **(2)** EC-AFM height image. **A:** Steel surface in air demonstrates the baseline surface. **B:** Steel surface in 1 M KCl solution at open circuit potential (OCP) exhibits growth of small KCl precipitates. **C:** Steel surface in 1 M KCl solution at reducing potential (-1000 mV) results in the breakdown of both the precipitated material as well as the uppermost layers of the steel surface.

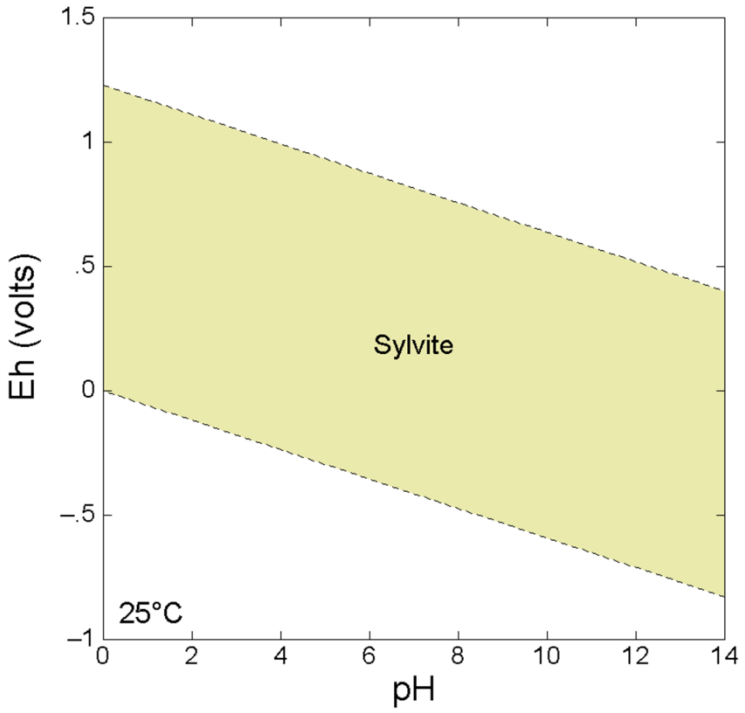

Figure 3.3: Eh-pH diagram for a 1 M KCl solution.

A 1.6 mM U_{60} solution was used for the remainder of the experiments. At OCP, sorbates ~10 nm in diameter appear after the first 14 min of immersion in solution (Figure 3.4B). Sorbate structures appear both as convex quadrilateral polygons (Figure 3.4C) and as distinct, roughly circular growths (Figure 3.5). The polygonal sorbates dominate in both number and size after 170 min of immersion, appearing to grow out of the roughly circular sorbates, but can be found as early as 16 min after solution injection. Circular sorbates dominate for the first 170 min of immersion, but are far less numerous afterwards, due to their eventual evolution into polygonal sorbates. Additionally, the presence of polygonal sorbates as tall as 238 nm and as wide as 800 nm, are likely to obstruct observation of these smaller surface features. After 62 min, circular sorbates had increased to 80 nm in diameter and smaller sorbates cover ~45% of the

sample surface. At the 152-min mark, circular sorbates are observed as large as 164 nm in diameter, 52 nm in height, and 0.021 μm^2 in area (Figure 3.5). At 252 min, polygonal sorbates were measured with a mean diameter of 469 nm, 52 nm height, and area of 0.31 μm^2.

The observation of the polygonal sorbates is linked to the growth of crystalline U_{60}, as it has been shown that individual U_{60} spheres typically form into a crystalline face-centered-cubic (FCC) configuration (Sigmon et al., 2009b). As such, it is likely that the polygonal sorbates observed in Figure 3.4 are the beginning stages in the formation of these U_{60} crystals. It is also known that carbon fullerenes, or C_{60}, the topological twin of U_{60}, form in FCC configurations of C_{60} spheres at room temperatures (David et al., 1991). C_{60} spheres have been shown to form composite clusters (non-crystalline conglomeration of individual spherical clusters via the injection of a poor solvent, like acetonitrile, into a C_{60} solution in a good solvent (effective at dissolving the solute), like toluene (Umeyama and Imahori, 2008). U_{60} clusters can form similar composite clusters (aggregates known as "blackberries"), accounting for the presence of the spherical sorbates in Figure 3.5 (Turner et al., 2017).

Island growth and overlapping was observed with both types of sorbates, possibly indicating an epitaxial relationship. No apparent trend was found between location and sorbate growth, with particle distribution roughly homogeneous throughout the sample surface. This is further demonstrated by the fact that total sorbate surface coverage stays roughly constant at 0.15% and 0.43% over 500 min of sorbate growth. Plotting of these observations reveals the decrease of the total number of sorbates and sorbate distribution density; while the mean sorbate height, area, diameter and volume all increase, indicating particle convalescence or Ostwald ripening (Fig. 3.6). Such behavior is consistent with the growth of U_{60} crystals that self-assemble to form cubic solids.

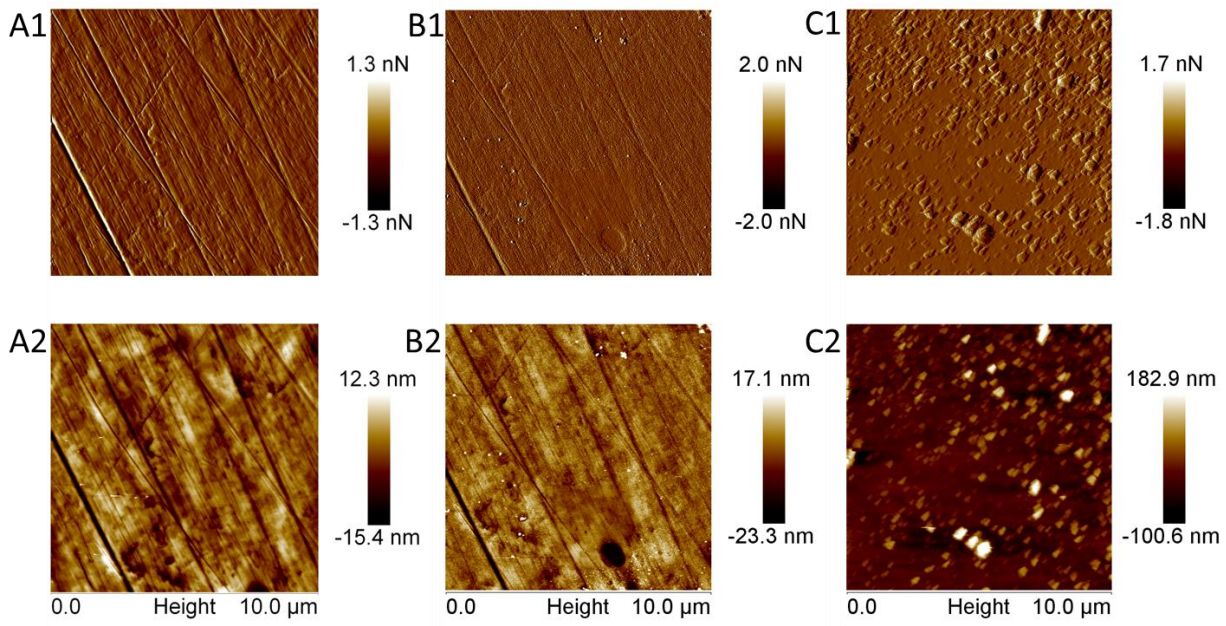

Figure 3.4: AFM image of Steel surface in 1.6 mM U_{60} solution at pH 10.6 **(1)** EC-AFM peak force error (PFE) image. **(2)** EC-AFM height image. **A:** Steel surface in air demonstrates the baseline surface. **B:** Steel surface in U_{60} solution at open circuit potential (OCP) exhibits growth of small precipitates. **C:** Steel surface in U_{60} solution at reducing potential (-0.5 V vs. SHE) results in accelerated growth of precipitates shown here with polygonal sorbates (crystalline U_{60}).

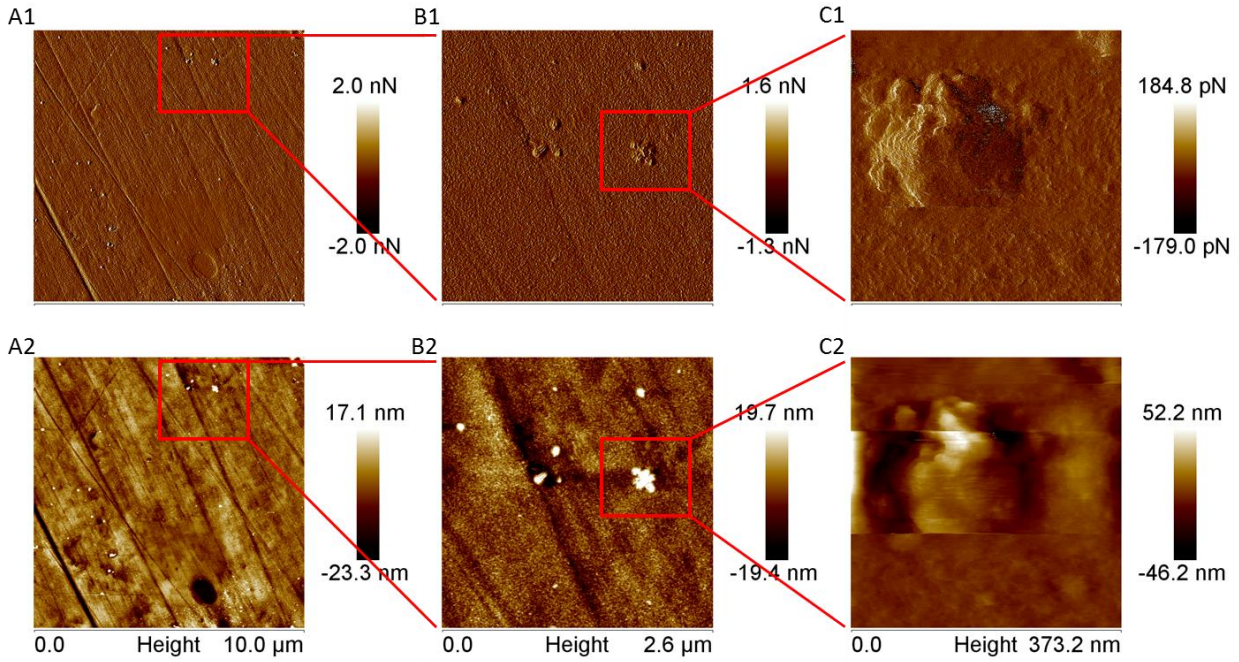

Figure 3.5: AFM image of steel surface in 1.6 mM U_{60} solution at pH 10.6 **(1)** EC-AFM peak force error (PFE) image. **(2)** EC-AFM height image. **A:** Steel surface in U_{60} solution at open circuit potential (OCP) exhibits growth of small precipitates. **B:** Magnified steel surface in U_{60} solution at OCP exhibits the formation of U_{60} composite clusters. **C:** Magnified steel surface in U_{60} solution at OCP shows single composite cluster.

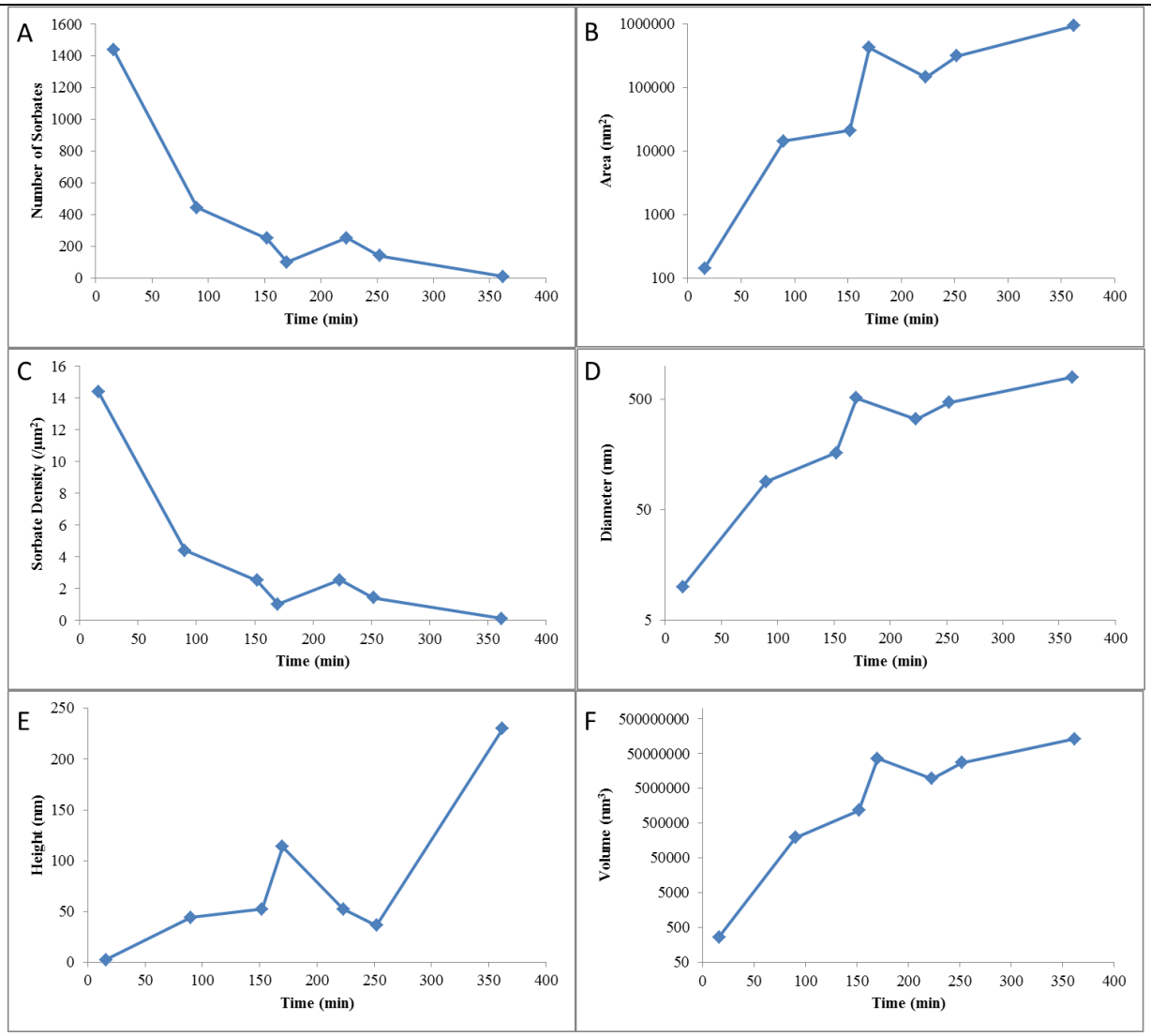

Figure 3.6: Sorbate quantification from EC-AFM imagery processing. Sorbate metrics in 1.6 mM U_{60} solution at pH 11 at OCP. **A**: Number of sorbates versus time. **B**: Mean sorbate area. **C**: Mean sorbate density. **D**: Mean sorbate diameter. **E**: Mean sorbate height. **F**: Mean sorbate volume.

As expected from the Eh-pH diagram for the UO_2 speciation (Figure 3.1), highly oxidizing and reducing potentials (+1000/-1000 mV) result in the dissolution of sorbates. Similar to observations in KCl solution, at highly reducing potentials, dissolution of sorbates is followed by the breakdown of the uppermost layers of the surface and the formation of green oxidized iron

particulates in the formerly colorless solution immediately following polarization as shown in (Figure 3.2C).

After approximately 520 min of deposition at OCP, the number of sorbates decreases and the mean size (height, area, diameter, and volume) of sorbates increases (Fig. 3.6). At weakly reducing potentials (-500 mV), an immediate increase in the deposition of small (>10 nm) spherical sorbates was observed, the number of sorbates quickly jumps by a factor of 10 or more while the mean height, area, diameter, and volume fall due to the drastic increase in the number of small sorbates now depositing on the substrate surface. Weakly oxidizing potentials (+500 mV) appear to have a negligible effect on the growth of these sorbates vs. growth at OCP, but small changes in sorbate characteristics (especially height) is difficult to measure given the slow erosion of sorbed species due to physical contact with the AFM tip. This destructive analysis by the tip is evidenced by successive images (without changing location) decreasing overall sorbate height over time.

3.4.2 Scanning Electron Microscopy

Scanning electron microscopy (SEM) was used to image sample surfaces before and after EC-AFM polarization experiments. Steel surfaces were immersed in 1.6 mM U_{60} solutions at pH 10.6 and polarized at reducing potentials (below -0.25 V to sufficiently reduce U(VI) on the surface) for 1000 seconds. Figure 3.7 shows a micrograph of a steel surface after polarization, at what is termed in this study as Site 1. Site 1 demonstrates the growth of small needle-shaped particles that appear lighter in color than the surrounding grains (indicative of a heavier elemental composition). Energy-dispersive spectroscopy (EDS) shows U peaks (Mα) that correspond to the lighter colored regions of the sample surface containing these needle-like particles (Figure 3.8, region 2). As shown in Figure 3.7, the coverage of these grains is not

uniform, and is estimated at a total surface coverage of 10%. The majority of the sample surface consists of the surrounding dark grey material free of needles seen in Figure 3.7A. EDS of this region indicates the overwhelming presence of Fe, corresponding to the raw steel sample surface, composed of ~99% Fe (Figure 3.8, region 1). Studies by Renock et al. (2013) and Wersin et al. (1994) report similar needles adsorbed to pyrite (FeS_2) and galena (PbS) surfaces in uranyl solutions suggesting that these needles are not associated with uranyl peroxides, but rather are a U-oxide or an Fe-containing solid associated with U.

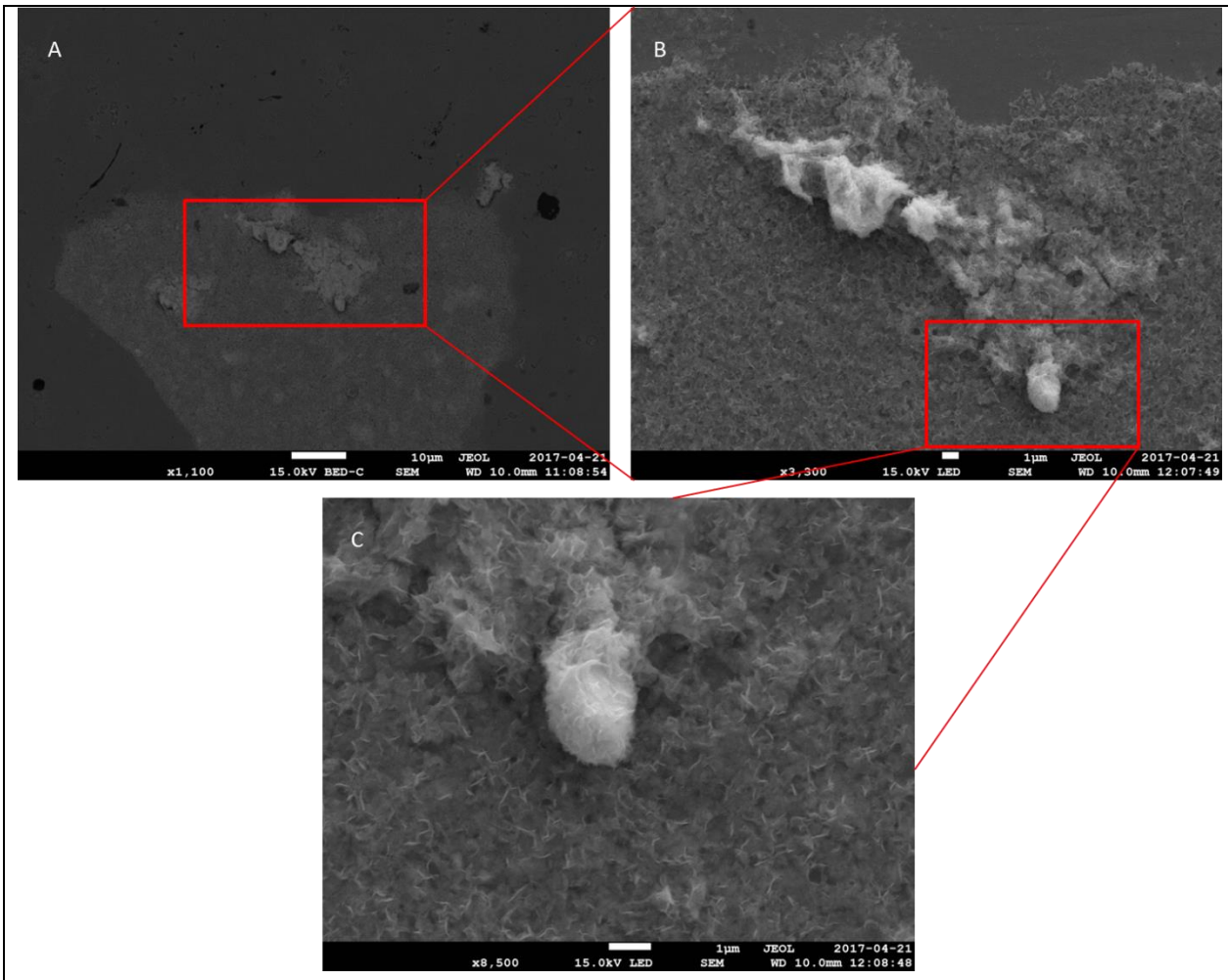

Figure 3.7: SEM backscattered electron images of U adsorbate (Site 1). The 10-50 nm needlelike structures observed are composed of uranium oxide.

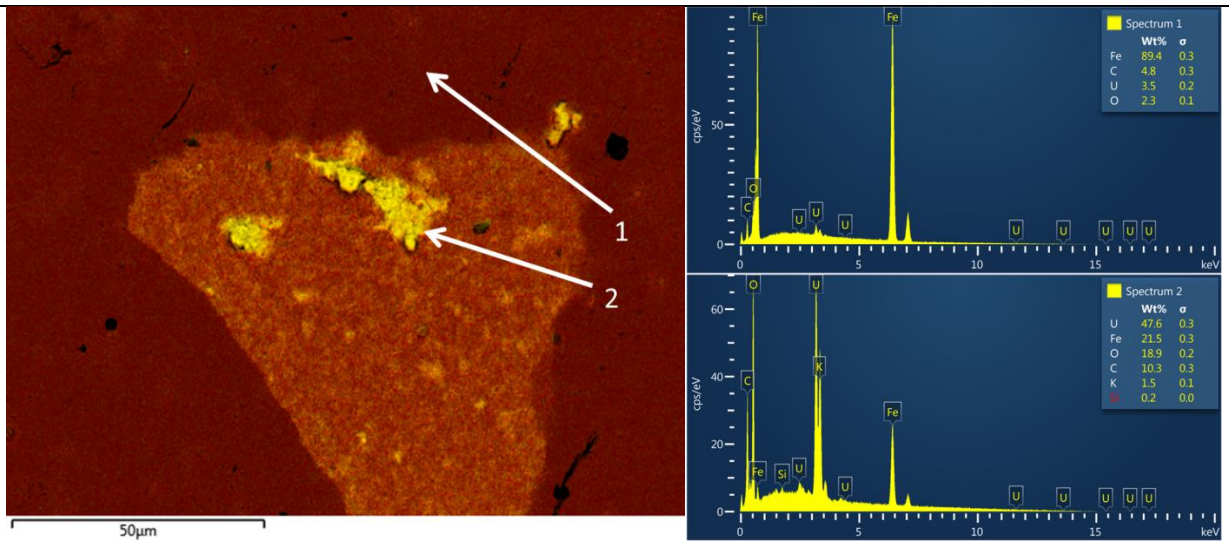

Figure 3.8: SEM-EDS Site 1. SEM-EDS composite image (left) showing steel surface (red, Spectrum 1) and uranium-bearing adsorbates (yellow, Spectrum 2). EDS **Spectrum 1** (right) shows the high Fe and C concentrations characteristic of steel. Minor U concentrations result from a thin layer of small adsorbates coating the majority of the surface. EDS **Spectrum 2** (right) demonstrates composition of adsorbates. High U and O concentrations are characteristic of the needlelike sorbates. Spectrum 2 continues to return a Fe signal due to the steel substrate beneath coupled with the sampling depth and excitation volume of our instruments.

Figure 3.9 and Figure 3.10 exhibit Site 2, distinct from Site 1 in that the needle-like sorbates are absent, replaced by light colored, roughly spherical particles. The observed spheres are unlikely to represent single uranium nanoclusters, as the diameter of U_{60} has been determined as 2.7 nm (Ling et al., 2012; Qiu and Burns, 2013; Sigmon et al., 2009b), and the spherical sorbates observed in SEM vary from about 10-30 nm in diameter. However, individual U_{60} clusters, like C_{60} clusters, are known to assemble and form crystalline structures (cubic space group $Fm\bar{3}$) and single crystals (with octahedral symmetry) of up to 3 mm in diameter have been produced using procedures from the literature (David et al., 1991; Sigmon et al., 2009b). Therefore, it is possible that the irregular spheres observed in Figure 3.9 and Figure 3.10 represent the initial growth of these cubic structures (larger crystals taking days to grow), a process that has never been imaged before. It is also possible that U_{60} fullerenes are forming what is known as composite clusters, a process by which some fullerene materials will deposit as amorphous aggregates of clusters

forming larger roughly spherical conglomerate shapes, which is explored further in Section 3.4.3. Analysis by EDS again shows the background dark colored material as primarily Fe, and the light colored particles as primarily U (Figure 3.10).

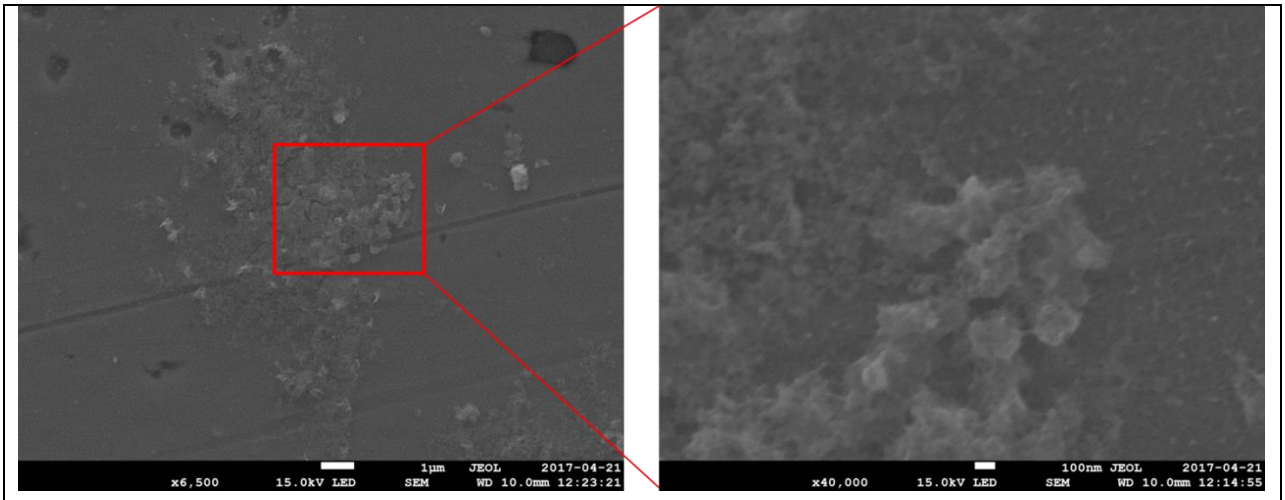

Figure 3.9: SEM Backscattered Electron images of U adsorbate (Site 2). Site 2 has a structure that appears as composite clusters of U_{60}. Representative images are difficult to obtain as the maximum resolution for the JEOL Instrument is 10 nm (roughly 4 times the diameter of U_{60}).

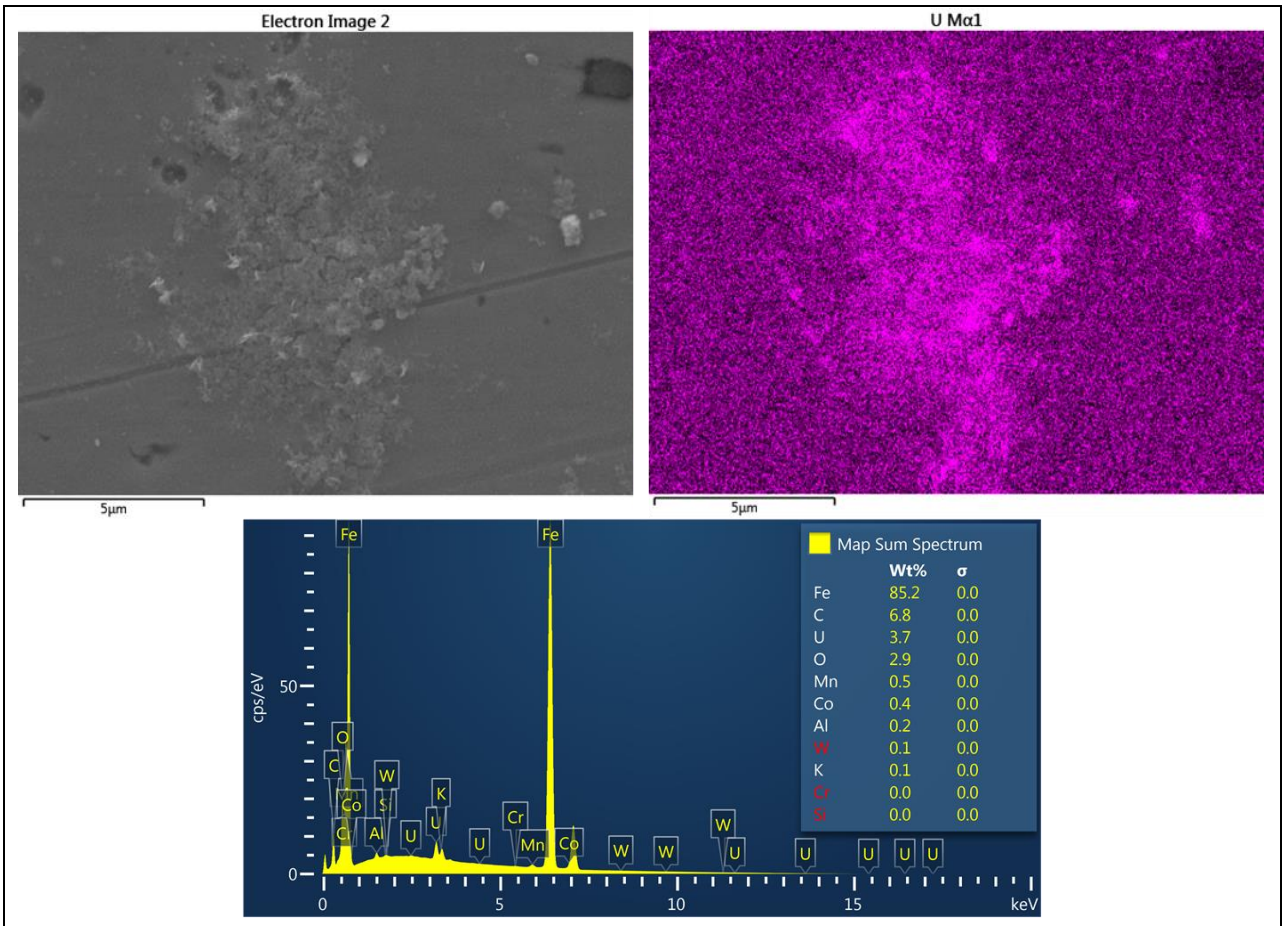

Figure 3.10: SEM-EDS Site 2. SEM-EDS map (top) showing distribution of U-containing material. SEM-EDS spectrum (bottom) showing U and K composition characteristic of U_{60}.

Uranium-dense regions containing spherical nanoparticles (like Site 2) are sometimes found to co-occur with the needle-like particles found in Site 1. Figure 3.11 (SEM Site 3) shows just such a region, where the lighter-colored area, Site 3A, corresponds to far more U-rich area containing nanoparticles with spherical shape. Site 3B corresponds to the darker-colored area indicative of the needle-like particles from Site 1. When imaged together, Site 3 shows the distinct differences in sorbates from Site 1 vs. from Site 2. EDS results, coupled with the lighter color and the spherical shape support that Site 2 and Site 3A suggest the growth of uranyl peroxide nanoclusters. Such clusters contain anywhere from 20-120 coordinated uranyl groups, or in the case of U_{60}, 60 coordinated uranyl hexagonal bipyramids, the tight spacing of which

would account for the brighter color and greater U content when compared with the U-containing needles from Site 1 and Site 3B.

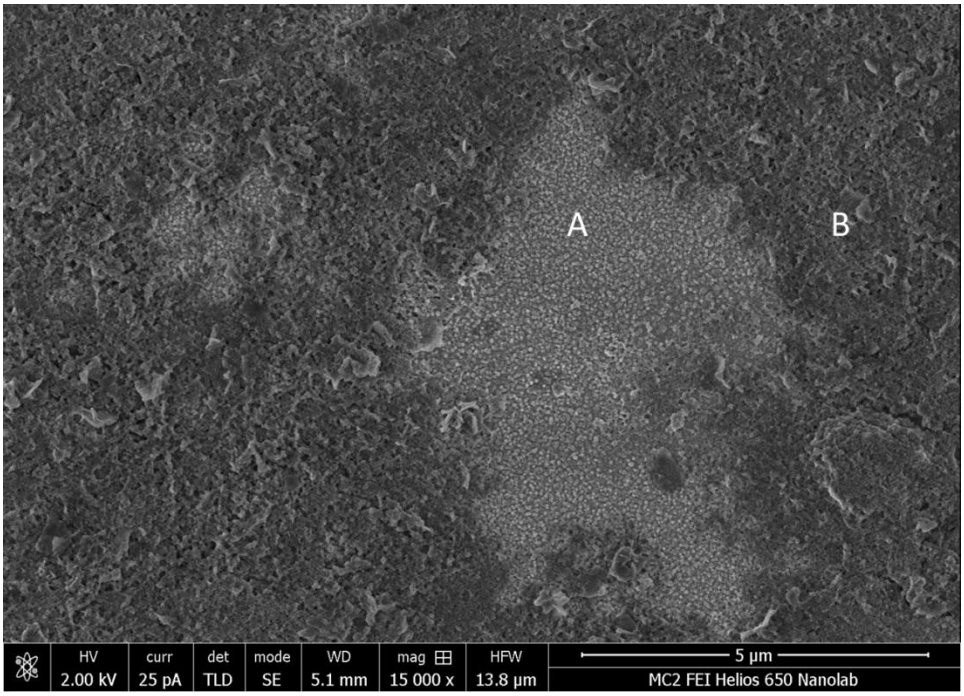

Figure 3.11: SEM Site 3. **A)** U-dense regions (lighter color) correspond with patches of the observed spherical nanoparticles attributed to uranyl peroxide cluster formation. **B)** Less U-dense regions (darker color) correspond with the U-associated needle-like particles observed in Site 1.

Despite clear structural evidence provided by SEM coupled with chemical analysis via EDS, it remains unclear whether the spherical sorbates observed are in fact U_{60} clusters. To establish this, a U_{60} crystal must be used as a standard for spectroscopic analysis. Furthermore, a far more surface-sensitive technique than EDS is needed given the nanometer-level heights of some of the smaller sorbates imaged, for which purpose Auger electron analysis (AES) was chosen.

3.4.3 Auger Electron Spectroscopy

In order to identify the phases observed to grow under ambient and reducing conditions, AES spectra were collected from sample surfaces at OCP and -500 mV. Compositional and spatial data were obtained down to a lateral resolution of 500 Å for elements comprising approximately the top 10 Å of the surface. High-resolution surface-sensitive AES spectra were collected from U_{60} crystals prepared according to the literature as a reference compound for comparison with the sorbates that appear at steel surfaces (Fig. 3.12). Assigning oxidation state with AES is complicated by the high background signature observed with such small volumes, the broad nature of Auger peaks, and the peak overlap inherent in shallow atomic level Auger transitions. AES analysis confirms our earlier findings with SEM, indicating an inhomogeneous distribution of sorbed uranium at the surface.

Sorbates observed in U_{60} solution were compared with a solid, crystalline sample of U_{60} prepared according to the literature. Using this U_{60} crystal as a reference compound, sensitivity factors were derived at each kinetic energy level, allowing the calculation of a relative ratio of Auger peaks. The Fe signal in the particle spectra of Figure 3.14 is likely due to the forward scattering of the electron beam onto the steel substrate from small and (in the case of the U-needles) narrow sorbates. These three types of sorbates observed are unlikely to contain any Fe. Thus, the relative ratio was calculated using elements that are characteristic to U_{60} (K and U) and using only the most prominent Auger transitions (U MNN at 77 eV, U MNN at 284 eV, U MNN at 2764 eV, and K LMM at 252 eV) (Fig. 3.14). Comparing this relative ratio to our observed sorbates serves as an indication of whether sorbates produce the same Auger spectral distribution as our U_{60} crystalline standard. The results in Table 3.1 demonstrate that the observed crystalline sorbates and composite cluster sorbates have U/K ratios closely matching those of the U_{60}

standard, therefore are most likely composed of U_{60} clusters. Table 3.1 also demonstrates that the U-related needle-like sorbates are not composed of U_{60}, as their Auger spectra lack two of the three characteristic U transitions and of the single U transition visible, the U/K ratio does not resemble that of the U_{60} standard. Thus it is likely that these U-needles are the same as those of similar shape observed by Renock et al. (2013) and Wersin et al. (1994) considered to be an inhomogeneously-distributed uranium oxide compound.

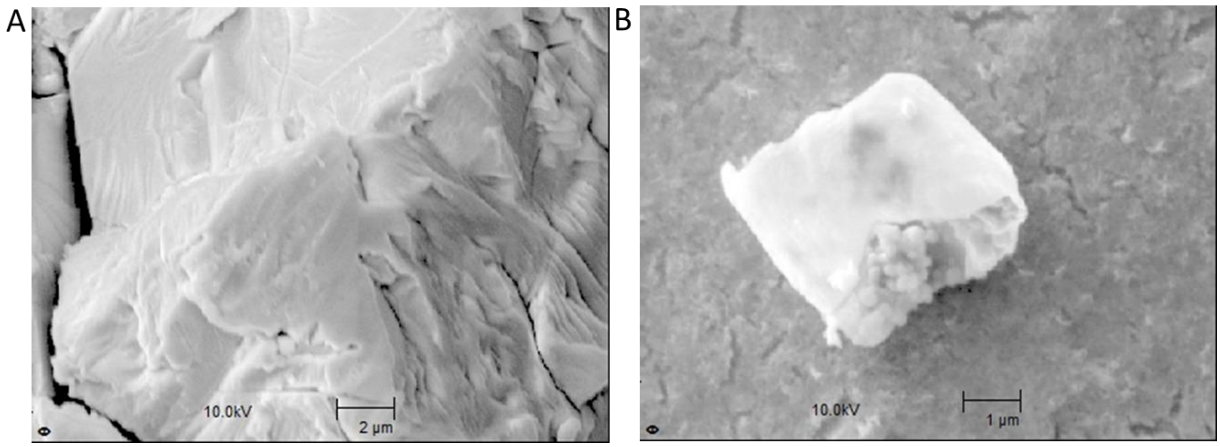

Figure 3.12: AES/SEM backscatter image of crystalline sorbates. (A.) U_{60} crystal grown according to the literature. (B.) U_{60} sorbate from EC-AFM experiments.

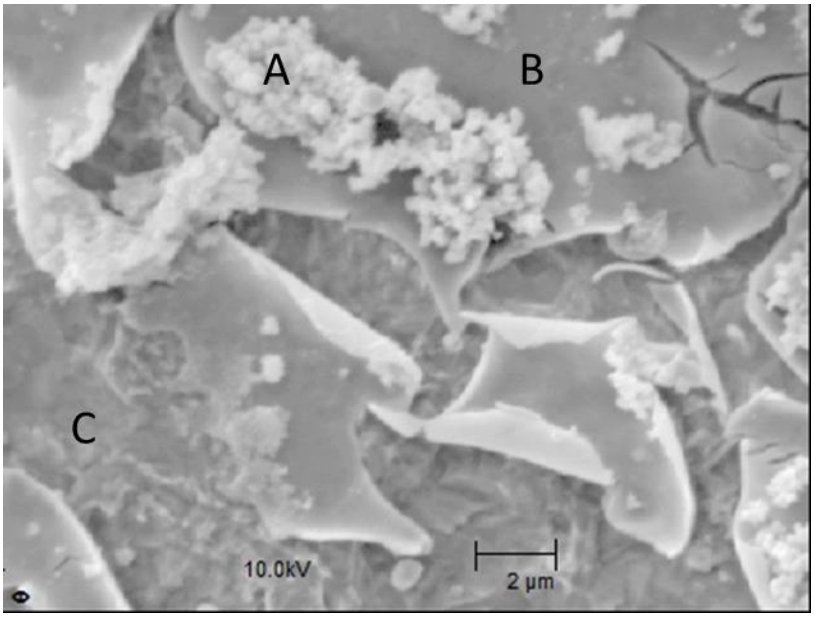

Figure 3.13: AES/SEM backscatter image of U_{60} composite cluster sorbates. **(A)** U-containing composite cluster sorbates. **(B)** Unaltered substrate surface (steel). **(C)** Steel surface corrosion. Exposure of steel surface and U_{60} solution to reducing potentials also forms green rust [$Fe(OH)_2$].

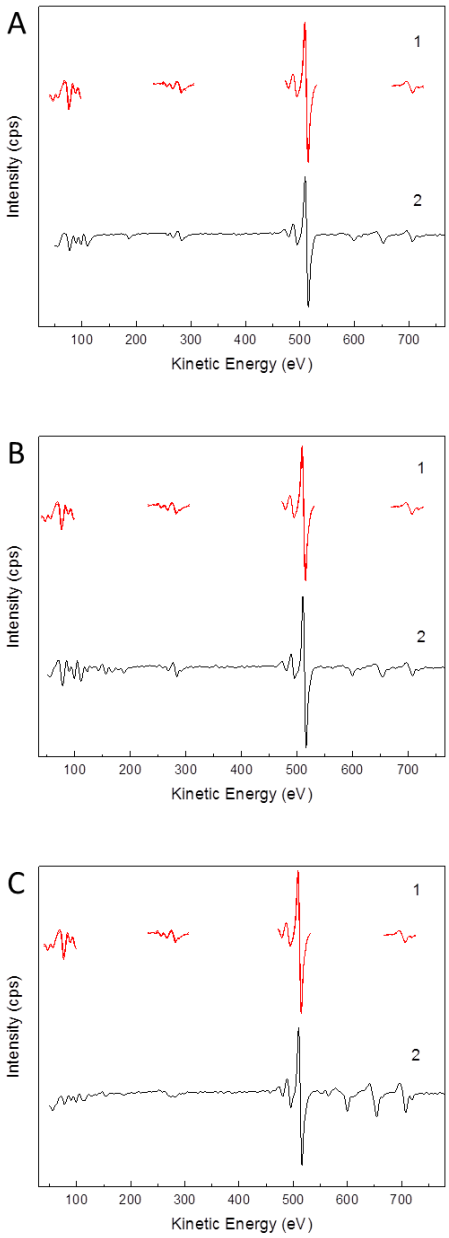

Figure 3.14: Differentiated AES spectra. (1) **A**, **B**, and **C**: Auger spectra of crystalline U_{60} standard illustrated in Fig. 3.12A. Point compositional spectra for U adsorbate shows the presence of U, O, Fe, and K. Auger transitions shown from left to right: U L1, K L1, O L1, O L1, and Fe L3 (U L3 omitted for clarity). (2) **A**: Spectra of crystalline sorbate illustrated in Fig. 3.12B. **B**: Spectra of composite cluster sorbate illustrated in Fig. 3.13A. **C**: Spectra of unaltered steel surface background.

	U/K Relative Ratio		
	U (77 eV)	**U (284 eV)**	**U (2764 eV)**
U_{60} Standard	1.80	0.76	0.14
Crystalline Sorbates	1.28	0.74	0.22
Composite Cluster Sorbates	1.34	0.72	0.15
Needle-like Sorbates	0.41	No Significant U Peaks Found	No Significant U Peaks Found

Table 3.1: Uranium/potassium relative ratio based on characteristic Auger peak heights.

3.5 Discussion

The results in this study demonstrate the ability of combined EC-AFM and spectroscopic methods to explore and image the precipitation and reduction processes at the substrate surface *in situ* as solution chemistry and redox potential are controlled. First, we have shown that a significant amount of sorbate growth is observed despite the (less favorable) flat surfaces required for accurate AFM analysis. Furthermore, sorbates at the substrate surface are both identifiable and can be charted to Eh-pH diagrams. Figure 3.1 and 3.3 demonstrate the ability of these diagrams to roughly predict the dominant phase present both with the well-categorized sylvite system (Figure 3.3) and the more complex uranyl system (Figure 3.1). The fit for the sylvite system is apparent as sylvite deposition is observed at -500 mV, +500 mV, and OCP; and deposition is not observed at -1000 mV and +1000 mV. The uranyl system proves more challenging due to the unknowns associated with the solution behavior of uranyl peroxide clusters. Furthermore, some clusters in solution are inevitably broken apart (especially when undersaturated) to UO_2^{2+}, H_2O_2, Li^+, and K^+, which can form multiple distinct phases deposited on the substrate surface, complicating identification.

Secondly, SEM-EDS and AES confirm the presence of uranyl peroxide nanocluster sorption onto steel surfaces through the use of U_{60} crystals (grown according to the literature) as standards. Figures 3.7, 3.8, and 3.11 indicate the presence of UO_2 needles likely formed as a result of the breakdown of U_{60} clusters into UO_2^{2+}. However, two individual types of sites related to intact U_{60} clusters are visible due to their features distinct from these UO_2 needles. Composite clusters of uranyl peroxide nanospheres are visible in AFM (Figure 3.5) and SEM (Figures 3.9, 3.10, 3.11, 3.13, and 3.15) as roughly spherical sorbates. In addition to their visual and structural differences, nanocluster sorbates are also chemically distinct due to the heightened density of U and K present in EDS and AES spectra. These spherical sorbates continue to grow and then form the second type uranyl nanocluster feature observed, crystalline nanospheres. These crystalline features appear in AFM images (Figure 3.4) as roughly polygonal sorbates and in SEM (Figure 3.12B) as the more distinct cubic structures characteristic of U_{60} crystals. The scarcity of the crystalline features observed in this study is expected due to the short timescales (hours) of surface deposition versus the longer timescales (days) of macroscopic U_{60} crystal growth.

Thirdly, comparison of U_{60} sorbates with their topological twin, the carbon-60 fullerene C_{60}, also forming cubic space group $Fm\overline{3}$ (Figure 3.15A), suggests the presence of a unique nanoparticle. As C_{60} and U_{60} share a common topology, space group, surface area, and size it is likely they will appear similar in SEM. The differences observed in U_{60} (Figure 3.15B) as compared with C_{60} could be reflective of the greater diameter of U_{60} (2.7 nm vs. 0.7 nm for C_{60}), the charge stabilizing Li^+ and K^+ content, or the island growth of isometric crystals. As shown, the U_{60} sorbates appear as rough irregular spheres, very similar in shape to the C_{60} sorbates. In C_{60} (Figure 3.15A), this shape is due to the formation of composite clusters (non-crystalline) of fullerenes 100-1000 nm in diameter containing cylindrical nanostructures called carbon

nanotubes, derived from the fullerene structure. The two main types of nanotubes that have high structural perfection are single-walled nanotubes (SWNT), those that consist of a single molecular sheet wrapped into a cylindrical tube, and multiwalled-nanotubes (MWNT), that describe an array of nanotubes nested in concentric rings. These nanotubes often present as fibers interconnecting various growths of C_{60} fullerenes in SEM, most commonly as MWNTs (Baughman et al., 2002). Figure 3.15A, however, shows the rarer formation of SWNTs (Umeyama and Imahori, 2008). The similarities observed in U_{60} (Figure 3.15B) could indicate the formation of composite clusters of U_{60} fullerenes and possibly a U_{60}-based single- or multi-walled nanotube structure. Comparing the fibrous growth characteristic of carbon nanotubes we observe similar growths in U_{60} adsorbed to steel surfaces. Carbon nanotube growths in concentrated growth solutions can easily exceed 500 nm in length; however our solutions at 1.6 mM U_{60} cluster concentration have not yielded any cohesive fibrous growth exceeding 50 nm. Further investigations are in progress with the intent of characterizing our observations which could result in the addition of uranyl peroxides to the list of carbon, boron, silicon, titanium, and gallium-based nanotube frameworks.

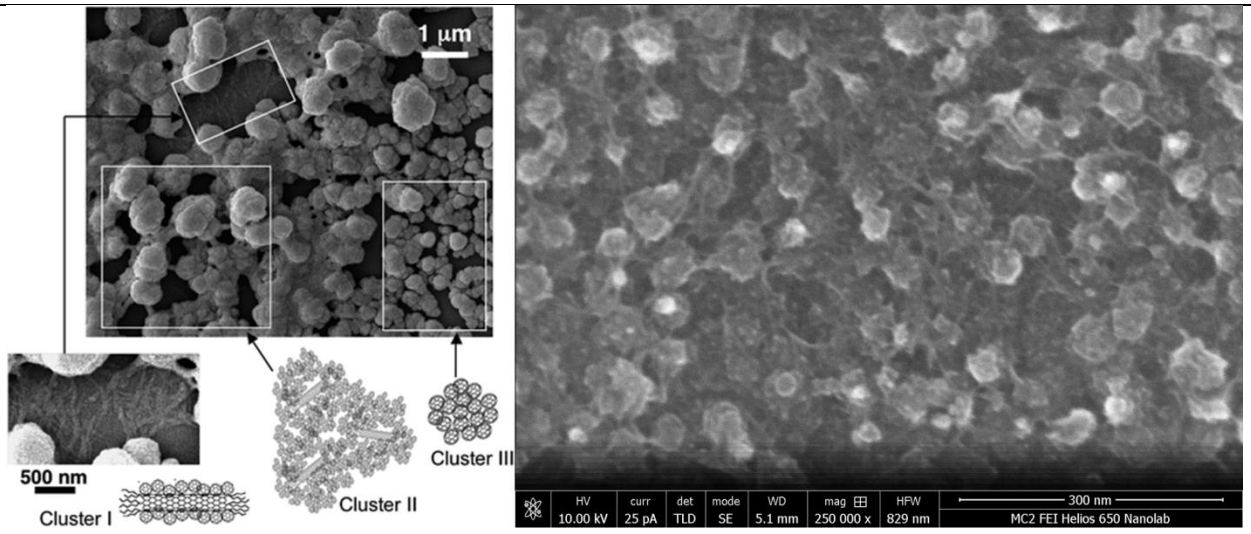

Figure 3.15: C_{60} Fullerenes vs. SEM Site 3. **A)** C_{60} fullerenes with fibrous interconnecting carbon nanotubes from (Umeyama and Imahori, 2008). **B)** SEM Site 3, note the fibrous interconnection between U nanoparticles. These fibers are reminiscent of carbon nanotubes found on C_{60} buckyballs. This could suggest the existence of a uranyl peroxide nanotube.

3.6 Conclusions

This study has demonstrated the feasibility of a combined EC-AFM and spectroscopic approach to image and characterize the solution characteristics and redox behavior of uranyl peroxide clusters both in solution and adsorbed to substrate surfaces. The use of EC-AFM allows for direct observation of U_{60} sorbates from solution at different electrochemical conditions. In this system, quantitative analysis of AFM imagery suggests that more U sorption occurs at reducing potentials (-500 mV) versus highly reducing potentials (-1000 mV), oxidizing potentials (+500 and +1000 mV), and at OCP. Growth observed under these conditions is dominated by three types of U-sorbates, (i) the formation and growth of composite clusters of U_{60} fullerenes, (ii) formation of FCC crystalline U_{60}, which possibly uses the composite cluster sorbates as nucleation sites for their formation, (iii) small 10-50 nm needles of a uranium oxide material likely formed by the dissolution of U_{60} fullerenes into UO_2^{2+}. In both cases, AFM analysis brings us the only imagery of U_{60} growth known to date.

The combined use of spectroscopic methods also provides additional, more quantitative evidence of the composition and structure of the sorbates observed. The use of SEM provides higher-resolution imagery than AFM (in this study), while AFM allows observation of the growth *in situ*, both aiding in the characterization of sorbates and revealing the possible presence of a new nanoparticle, a uranium fullerene based nanotube. Combined with EDS, the SEM imagery is supported with elemental analysis. However, such compositional analysis is complicated by the thinness of these sorbates, as the Fe signal from the steel substrate surface interferes with results. This shortcoming is averted through the use of AES, a highly surface-sensitive technique that obtains compositional data from even the smallest of sorbates, the beam interacting with only the top 10 Å of the surface. AES analysis also provides direct evidence of U_{60} sorbates at the substrate surface through the derivation of a sensitivity factor based on a crystalline U_{60} standard. Using this factor in tandem with the U/K relative ratio from AES spectra, any sorbate could be easily identified as containing (or not containing) U_{60} fullerenes.

As the mobility of uranyl is strongly affected by its interaction with substrate surfaces, so too is the mobility of uranyl peroxide clusters. Through a multi-method EC-AFM and spectroscopic approach, this study presents a new way to study the effects of U mobility via direct control of redox and pH conditions. With this combined approach, further analysis could be performed to image and characterize the entire Eh-pH range of uranyl peroxides *in situ*. With further refinement, this approach could be utilized to study the nanoscale sorption/desorption reactions of any redox-active material on any substrate surface.

3.7 Acknowledgements

This study was funded by the Department of Energy, Office of Basic Energy Sciences, Heavy Element Chemistry Program under Grant: DE-FG02-06ER15783. The authors would like

to thank Dr. Zhongrui (Jerry) Li for his assistance with AES analysis, Dr. Maria C. Marcano for her guidance concerning AFM analysis, and Dr. Robert Kerns for his help with SEM analysis.

3.8 Appendix

A. Electrochemical AFM Cell

Figure 3.16 displays a schematic diagram of the Bruker AFM cell used in these experiments. Figure 3.17 shows a picture of this cell rigged to a Bruker Dimension Icon AFM.

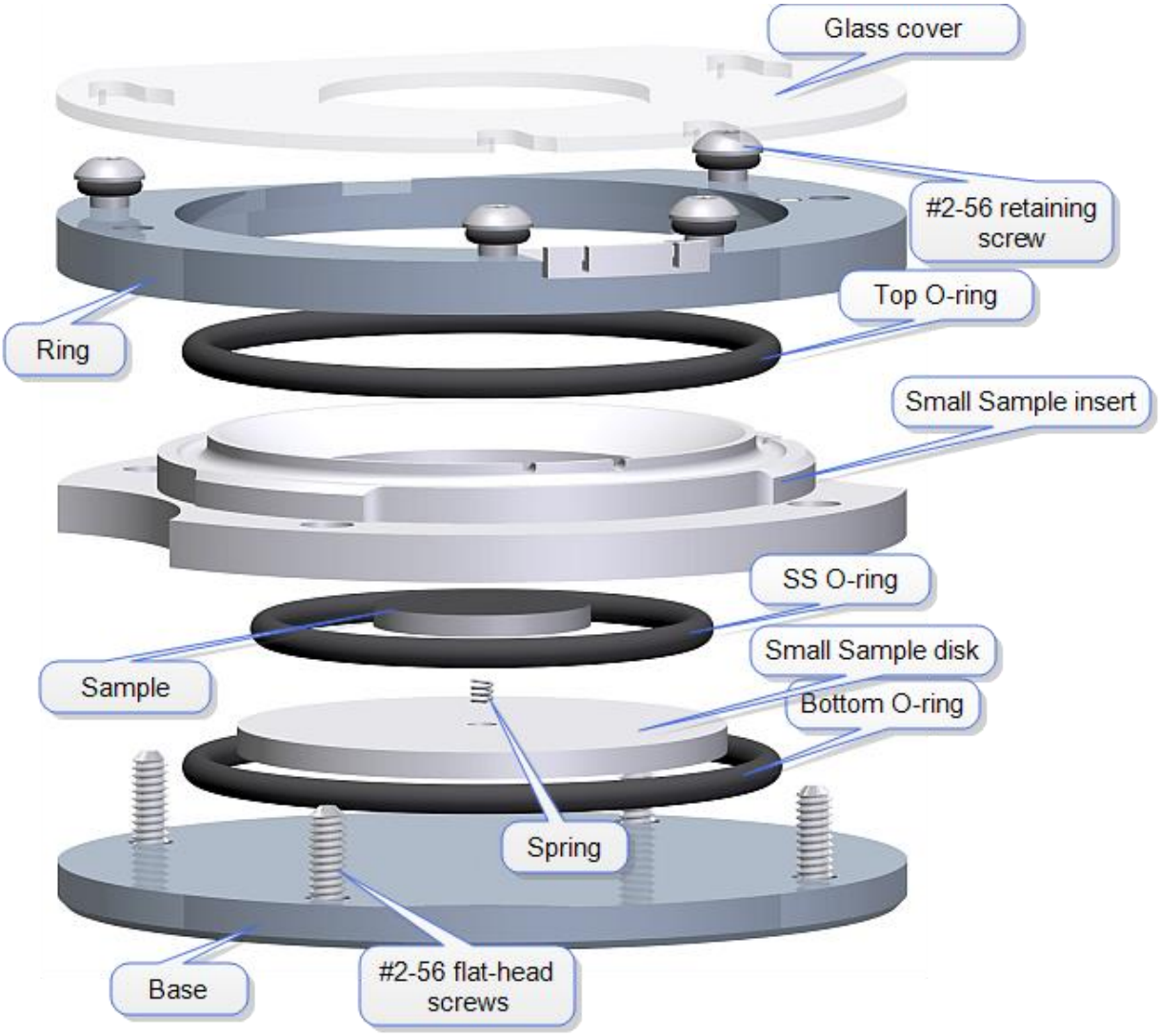

Figure 3.16 - Appendix: Schematic of EC-AFM cell from Bruker Inc.

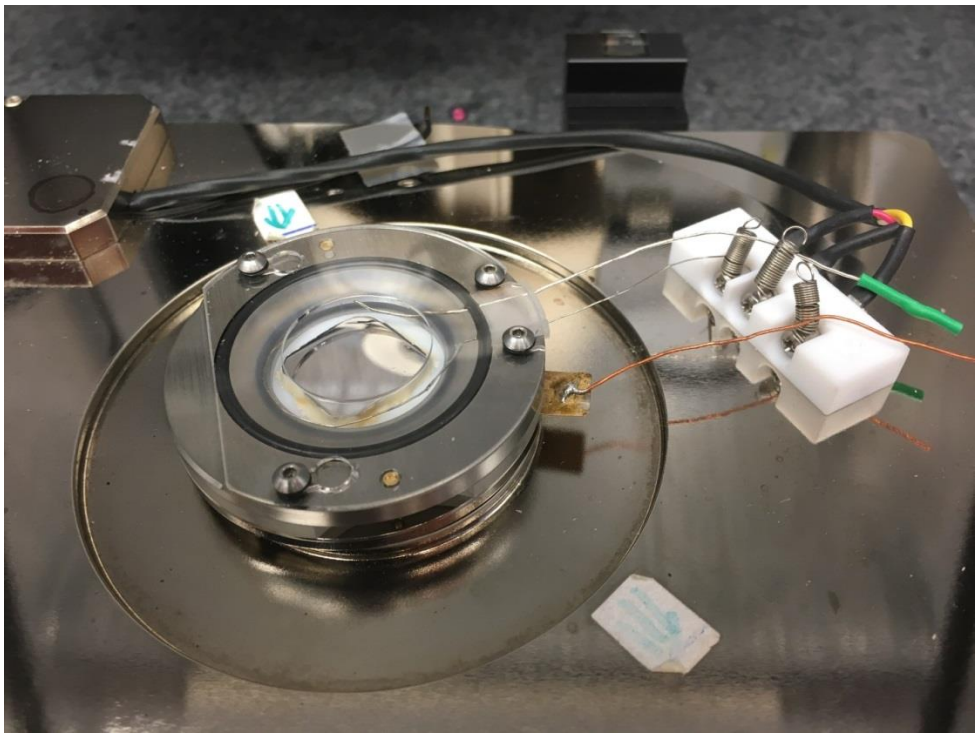

Figure 3.17 - Appendix: Rigged EC-AFM cell ready to receive solution.

3.9 Works Cited

Armstrong, C.R., Nyman, M., Shvareva, T., Sigmon, G.E., Burns, P.C. and Navrotsky, A. (2012) Uranyl peroxide enhanced nuclear fuel corrosion in seawater. *Proceedings of the National Academy of Sciences of the United States of America* **109**, 1874-1877.

Arumugam, K. and Becker, U. (2014) Computational redox potential predictions: Applications to inorganic and organic aqueous complexes, and complexes adsorbed to mineral surfaces. *Minerals* **4**, 345-387.

Baughman, R.H., Zakhidov, A.A. and de Heer, W.A. (2002) Carbon nanotubes - the route toward applications. *Science* **297**, 787-792.

Becker, U., Rosso, K.M. and Hochella, M.F. (2001) The proximity effect on semiconducting mineral surfaces: A new aspect of mineral surface reactivity and surface complexation theory? *Geochim. Cosmochim. Acta* **65**, 2641-2649.

Becker, U., Shuller, L., Renock, D. and Ewing, R. (2012) Comparison of computational and electrochemical approaches to determine redox reaction mechanisms of actinide complexes on mineral surfaces. *J. Am. Chem. Soc.* **243**.

Burns, P.C. (2005) U^{6+} minerals and inorganic compounds: Insights into an expanded structural hierarchy of crystal structures. *Can. Mineral.* **43**, 1839-1894.

Burns, P.C., Ewing, R.C. and Navrotsky, A. (2012) Nuclear fuel in a reactor accident. *Science* **335**, 1184-1188.

Choppin, G.R. (2007) Actinide speciation in the environment. *J. Radioanal. Nucl. Chem.* **273**, 695-703.

David, W.I.F., Ibberson, R.M., Matthewman, J.C., Prassides, K., Dennis, T.J.S., Hare, J.P., Kroto, H.W., Taylor, R. and Walton, D.R.M. (1991) Crystal-structure and bonding of ordered C_{60}. *Nature* **353**, 147-149.

Debets, P.C. (1963) X-ray diffraction data on hydrated uranium peroxide. *Journal of Inorganic & Nuclear Chemistry* **25**, 727-730.

Elsner, M., Haderlein, S.B., Kellerhals, T., Luzi, S., Zwank, L., Angst, W. and Schwarzenbach, R.P. (2004) Mechanisms and products of surface-mediated reductive dehalogenation of carbon tetrachloride by Fe(II) on goethite. *Environmental Science & Technology* **38**, 2058-2066.

Etienne, M., Schulte, A., Mann, S., Jordan, G., Dietzel, L.D. and Schuhmann, W. (2004) Constant-distance mode scanning potentiometry. 1. Visualization of calcium carbonate dissolution in aqueous solution. *Anal. Chem.* **76**, 3682-3688.

Finch, R.J. and Ewing, R.C. (1992) The corrosion of uraninite under oxidizing conditions. *J. Nucl. Mater.* **190**, 133-156.

Flynn, S.L., Szymanowski, J.E.S., Burns, P.C. and Fein, J.B. (2013) Experimental measurements of the effect of size on uranyl nanocluster stability in aqueous solution. *Abstr Pap Am Chem S* **246**.

Flynn, S.L., Szymanowski, J.E.S., Gao, Y.Y., Liu, T.B., Burns, P.C. and Fein, J.B. (2015) Experimental measurements of U_{60} nanocluster stability in aqueous solution. *Geochim. Cosmochim. Acta* **156**, 94-105.

Gagliardi, L., Vlaisavljevich, B., Ramirez, P.M., Cramer, C.J. and Burns, P.C. (2013) Ab initio and classical simulations modeling of uranyl peroxide nanoclusters. *J. Am. Chem. Soc.* **246**.

Gheju, M. (2011) Hexavalent chromium reduction with zero-valent iron (ZVI) in aquatic systems. *Water Air and Soil Pollution* **222**, 103-148.

Higgins, S.R. and Hamers, R.J. (1995) Spatially-resolved electrochemistry of the lead sulfide (galena) (001) surface by electrochemical scanning-tunneling-microscopy. *Surf. Sci.* **324**, 263-281.

Higgins, S.R. and Hamers, R.J. (1996) Chemical dissolution of the galena (001) surface observed using electrochemical scanning tunneling microscopy. *Geochim. Cosmochim. Acta* **60**, 3067-3073.

Higgins, S.R., Hamers, R.J. and Banfield, J.F. (1996) In-situ real-time imaging of the surface reactions of metal sulfide minerals with electrochemical STM. *Abstr Pap Am Chem S* **211**, 70-COLL.

Hixon, A.E., Arai, Y. and Powell, B.A. (2013) Examination of the effect of alpha radiolysis on plutonium(V) sorption to quartz using multiple plutonium isotopes. *J. Colloid Interface Sci.* **403**, 105-112.

Hyland, M.M. and Bancroft, G.M. (1990) Palladium sorption and reduction on sulfide mineral surfaces - an XPS and AES study. *Geochim. Cosmochim. Acta* **54**, 117-130.

Ilton, E.S., Haiduc, A., Moses, C.O., Heald, S.M., Elbert, D.C. and Veblen, D.R. (2004) Heterogeneous reduction of uranyl by micas: Crystal chemical and solution controls. *Geochim. Cosmochim. Acta* **68**, 2417-2435.

Kroto, H.W., Heath, J.R., Obrien, S.C., Curl, R.F. and Smalley, R.E. (1985) C_{60}: Buckminsterfullerene. *Nature* **318**, 162-163.

Ling, J., Qiu, J. and Burns, P.C. (2012) Uranyl peroxide oxalate cage and core-shell clusters containing 50 and 120 uranyl ions. *Inorg. Chem.* **51**, 2403-2408.

Lutze, W. and Ewing, R.C. (1988) Radioactive waste forms for the future. North-Holland ;Sole distributors for the USA and Canada, Elsevier Science Pub. Co., Amsterdam ; New York, N.Y., U.S.A.

Mallon, C., Walshe, A., Forster, R.J., Keyes, T.E. and Baker, R.J. (2012) Physical characterization and reactivity of the uranyl peroxide $UO_2(\eta^2\text{-}O_2)(H_2O)_2 \cdot 2H_2O$: Implications for storage of spent nuclear fuels. *Inorg. Chem.* **51**, 8509-8515.

Murakami, T., Ohnuki, T., Isobe, H. and Sato, T. (1997) Mobility of uranium during weathering. *Am. Mineral.* **82**, 888-899.

Qiu, J. and Burns, P.C. (2013) Clusters of actinides with oxide, peroxide, or hydroxide bridges. *Chem. Rev.* **113**, 1097-1120.

Renock, D. and Becker, U. (2010) A first principles study of the oxidation energetics and kinetics of realgar. *Geochim. Cosmochim. Acta* **74**, 4266-4284.

Renock, D., Mueller, M., Yuan, K., Ewing, R.C. and Becker, U. (2013) The energetics and kinetics of uranyl reduction on pyrite, hematite, and magnetite surfaces: A powder microelectrode study. *Geochim. Cosmochim. Acta* **118**, 56-71.

Rosso, K.M. and Becker, U. (2003) Proximity effects on semiconducting mineral surfaces II: Distance dependence of indirect interactions. *Geochim. Cosmochim. Acta* **67**, 941-953.

Shuller, L., Renock, D., Rak, Z., Fernando, S., Dzulkifli, I., Ewing, R. and Becker, U. (2011) Actinide adsorption onto mineral surfaces: A quantum-mechanical investigation. *J. Am. Chem. Soc.* **242**.

Sigmon, G.E., Ling, J., Unruh, D.K., Moore-Shay, L., Ward, M., Weaver, B. and Burns, P.C. (2009a) Uranyl-peroxide interactions favor nanocluster self-assembly. *J. Am. Chem. Soc.* **131**, 16648.

Sigmon, G.E., Unruh, D.K., Ling, J., Weaver, B., Ward, M., Pressprich, L., Simonetti, A. and Burns, P.C. (2009b) Symmetry versus minimal pentagonal adjacencies in uranium-based polyoxometalate fullerene topologies. *Angewandte Chemie-International Edition* **48**, 2737-2740.

Stack, A.G. (2008) Applications of electrochemical scanning tunneling microscopy to adsorption and thin films in geochemical systems. *Abstr Pap Am Chem S* **235**.

Stack, A.G., Eggleston, C.M. and Engelhard, M.H. (2004a) Reaction of hydroquinone with hematite I. Study of adsorption by electrochemical-scanning tunneling microscopy and x-ray photoelectron spectroscopy. *J. Colloid Interface Sci.* **274**, 433-441.

Stack, A.G., Erni, R., Browning, N.D. and Casey, W.H. (2004b) Pyromorphite growth on lead-sulfide surfaces. *Environmental Science & Technology* **38**, 5529-5534.

Taylor, S.D., Becker, U. and Rosso, K.M. (2017) Electron Transfer Pathways Facilitating U(VI) Reduction by Fe(II) on Al- vs Fe-Oxides. *Journal of Physical Chemistry C* **121**, 19887-19903.

Taylor, S.D., Marcano, M.C., Rosso, K.M. and Becker, U. (2015) An experimental and ab initio study on the abiotic reduction of uranyl by ferrous iron. *Geochim. Cosmochim. Acta* **156**, 154-172.

Tessis, A.C., Penteado-Fava, A., Pontes-Buarque, M., de Amorim, H.S., Bonapace, J.A.P., De Souza-Barros, F. and Vieyra, A. (1999) Pyrite suspended in artificial sea water catalyzes hydrolysis of adsorbed ATP: Enhancing effect of acetate. *Origins Life Evol. Biosphere* **29**, 361-374.

Turner, K.M., Szymanowski, J.E.S., Zhang, F.X., Lin, Y., McGrail, B.T., Mao, W.L., Burns, P.C. and Ewing, R.C. (2017) Uranyl peroxide nanoclusters at high-pressure. *J. Mater. Res.* **32**, 3679-3688.

Umeyama, T. and Imahori, H. (2008) Carbon nanotube-modified electrodes for solar energy conversion. *Energ Environ Sci* **1**, 120-133.

Vlaisavljevich, B., Gagliardi, L. and Burns, P.C. (2010) Understanding the structure and formation of uranyl peroxide nanoclusters by quantum chemical calculations. *J. Am. Chem. Soc.* **132**, 14503-14508.

Vorlicek, T.P. and Helz, G.R. (2002) Catalysis by mineral surfaces: Implications for Mo geochemistry in anoxic environments. *Geochim. Cosmochim. Acta* **66**, 3679-3692.

Wersin, P., Hochella, M.F., Persson, P., Redden, G., Leckie, J.O. and Harris, D.W. (1994) Interaction between aqueous uranium(VI) and sulfide minerals - spectroscopic evidence for sorption and reduction. *Geochim. Cosmochim. Acta* **58**, 2829-2843.

Wigginton, N.S., Rosso, K.M., Stack, A.G. and Hochella, M.F. (2009) Long-range electron transfer across cytochrome-hematite (αFe_2O_3) interfaces. *Journal of Physical Chemistry C* **113**, 2096-2103.

Xu, L.C., Wang, Y.X., Lu, J.W., Lu, X.S., Liu, Y.C. and Liu, X.Y. (2002) Radioactive contamination of the environment as a result of uranium production: a case study at the abandoned Lincang uranium mine, Yunnan Province, China. *Science in China Series B-Chemistry* **45**, 11-19.

Yuan, K., Ilton, E.S., Antonio, M.R., Li, Z.R., Cook, P.J. and Becker, U. (2015a) Electrochemical and spectroscopic evidence on the one-electron reduction of U(VI) to U(V) on magnetite. *Environmental Science & Technology* **49**, 6206-6213.

Yuan, K., Renock, D., Ewing, R.C. and Becker, U. (2015b) Uranium reduction on magnetite: Probing for pentavalent uranium using electrochemical methods. *Geochim. Cosmochim. Acta* **156**, 194-206.

CHAPTER 4

Quantum Mechanical Determination of the Incorporation of Pentavalent Plutonium into Carbonate and Sulfate Minerals

Benjamin B. Gebarski and Udo Becker

Department of Earth and Environmental Sciences, University of Michigan, 2534 C.C. Little Building, 1100 North University Avenue, Ann Arbor, MI 48109-1005, USA

4.1 Abstract

Pentavalent plutonium is the most abundant form of soluble, mobile, and oxidized Pu in natural systems. The incorporation of Pu into environmentally abundant mineral hosts can strongly influence the transport and concentration of contaminants in both aqueous environments and the subsurface. This study concerns the adsorption of Pu in the pentavalent state onto carbonate and sulfate surfaces, and its subsequent incorporation into the uppermost surface layer and bulk structures using *ab initio* computational methods. Through analysis of solid source and sink reaction energies on cleaved surface structures,

$(XCO_3)_4 + ½(Pu_2O_5) + (H_2CO_3) \rightleftharpoons ½(H_2O) + (XCO_3)_3(PuO_2)(HCO_3) + (XCO_3)$

for carbonate structures and

$(XSO_4)_4 + ½(Pu_2O_5) + (H_2SO_4) \rightleftharpoons ½(H_2O) + (XSO_4)_3(PuO_2)(HSO_4) + (XSO_4)$

for sulfate structures, where "X" denotes an alkaline earth cation.

When solid sources for Pu and solid sink phases for the alkaline earth elements (and Pb) are used, it was found that barite group and aragonite ($CaCO_3$) bulk and surface mineral structures

with (2/m 2/m 2/m) symmetry and a ΔE_{rxn} between +0.46 eV and +3.1 eV, are more favorable for PuO_2^+ incorporation than other host minerals such as calcite ($CaCO_3$) with (3 2/m) symmetry and a ΔE_{rxn} of +5.6 eV. Analysis of incorporation energies when using aqueous sources for Pu and aqueous sinks for the alkaline earth cations, utilizing a unique method for ion hydration, further supports our findings that structures with orthorhombic (2/m 2/m 2/m) crystal symmetry and larger coordination number and ionic cavities are more favorable for PuO_2^+ incorporation. Our data show that the [barite] $BaSO_4$ crystal structure is the most favorable for plutonyl incorporation into the bulk with a ΔE_{rxn} of +0.1 eV, followed by [anglesite] $PbSO_4$ (+0.1 eV), [celestine] $SrSO_4$ (+0.7 eV), [anhydrite] $CaSO_4$ (+0.9 eV), [aragonite] $CaCO_3$ (+1.0 eV), and [calcite] $CaCO_3$ (+2.65 eV). Additionally, we find that increasing size of cation site for PuO_2^+ incorporation [Ba^{2+} (1.35 Å) Pb^{2+} (1.19 Å), Sr^{2+} (1.18 Å), Ca^{2+} (0.99 Å)] correlates directly with a decrease in ΔE_{rxn} and therefore facilitates incorporation. This factor was found to be less significant than that of crystal symmetry, accounting for a maximum ΔE_{rxn} change of 1.2 eV.

While previous studies have used a similar methodology for calculating the thermodynamics of incorporation, what is new in this study is that the method was extended to observe the rate-controlling steps from a species in solution (*e.g.*, PuO_2^+ and HSO_4^- or HCO_3^-), to their co-adsorbed state on their respective carbonate or sulfate surface, followed by their co-incorporation (by replacing divalent cations and anions from the surface of the host mineral), and finally being incorporated into the bulk, mimicking the stability of co-precipitated or overgrown plutonyl defects. In general, thermodynamic trends of adsorption and surface incorporation are consistent in that the adsorption is an exothermic process and the highest endothermic step is the incorporation into the surface layer, while relatively insignificant gains or losses are observed when going from surface to bulk incorporation. Considering adsorption, carbonate minerals were

found to be more favorable for incorporation than sulfates due to their flexible CO_3^{2-} hybridization, but the effect is not great enough to offset the large symmetry contributions to final energies. The surface adsorption energies of all species are approximately the same at -2 eV, favoring the adsorption of the plutonyl ion. Surface incorporation energies are less energetically downhill, with aragonite (-2.0 eV) being the least unfavorable by 3.3 eV and calcite (+1.28 eV) being the least favorable. These findings, with their improved environmentally-relevant approach, considering both hydration and mineral surfaces, narrow the list of minerals favorable for the incorporation of actinides for future experimental study.

4.2 Introduction

The chemistry and behavior of actinides as they interact with minerals is integral to the understanding of the migration and sequestration of radionuclide contaminants within the environment. Actinides are found in natural systems in the trivalent (An^{3+}), tetravalent (An^{4+}), pentavalent (AnO_2^{+}), and hexavalent (AnO_2^{2+}) states. Pentavalent actinides are of particular interest due to their stability in a variety of aqueous environmental conditions, chiefly those in oxidizing conditions such as rain, rivers, and oceans – those close to human dwelling.

This is especially the case for one of the main products of uranium nuclear fuel, plutonium. The chemistry of the plutonyl ion (PuO_2^{+}) with pentavalent Pu in the center is of particular importance in the aging processes and possible unintentional release of stored Pu in weapons, fuel, wastes, and that used for scientific purposes (Ewing, 2015; Kaplan et al., 2014; Lantzos et al., 2015; Orlandini et al., 1986; Paviet-Hartmann, 2012; Powell, 2012; Steele and Taylor, 2007; Wiss et al., 2014). A major concern regarding these repositories is the ease with which they can contaminate the environment via an aqueous system. Actinyl compounds such as plutonium are highly mobile in aqueous systems, as they can dissolve and form linear dioxo-cations in the

pentavalent state under oxidizing conditions (Burns et al., 1997). The PuO_2^+ monocation is the least reactive form of the Pu aqua ion, resulting in a high solubility and mobility. Although Pu(V) is unstable towards disproportionation to Pu(IV) and Pu(VI), disproportionation equilibrium dictates that Pu(V) will be stable at trace concentrations (at pH > 3) and oxidizing conditions, easily found in contaminated surface waters, rain, and rivers (Topin and Aupiais, 2016). However, if mobile actinyl ions are adsorbed to mineral surfaces (without oxidation state change), they tend not to remobilize unless there is a drastic change in pH. If mobile actinyl ions in solution are incorporated into the crystal structure of a precipitating host mineral (coprecipitation), then such ions will remain insoluble barring dissolution of the entire host mineral (Bruno and Ewing, 2006; Burns et al., 1997). The studies by Orlandini et al. (1986) and later by Choppin (2007) provide analytical evidence supporting that Pu(V) is the predominant form of oxidized plutonium in natural waters. Therefore, this study investigates the feasibility of removing mobile Pu(V) contaminants from an aqueous system onto and into different host minerals by evaluating the thermodynamics of incorporation using computational models of surface and bulk incorporation reactions involving carbonate and sulfate minerals. Should such incorporation prove favorable, requiring only a small amount of energy input, these findings could prove valuable to sequestration efforts concerning mobile actinide contaminants.

There have been few experimental studies in which pentavalent plutonium has been incorporated in carbonate and sulfate structures (Choppin, 2007; Keeney-Kennicutt and Morse, 1985; Orlandini et al., 1986). Even fewer theoretical studies model the energy input required to incorporate Pu(V) ions into host minerals (Steele and Taylor, 2007). Our study uses an *ab initio* quantum-mechanical approach to calculate the structure, energetics, and thermodynamics of pentavalent plutonyl incorporation onto the surface and into the bulk of carbonate and sulfate

minerals. We furthermore apply a method developed by Shuller et al. (2013) to combine periodic, cluster, and aqueous models to simulate the incorporation of an aqueous ion into a solid mineral phase independent of empirical parameters. The resulting incorporation thermodynamics of the linear cation PuO_2^+ in different host minerals, structure types, and surfaces can be ultimately converted into the maximum amount of incorporation at equilibrium conditions (incorporation limits). Such limits can give an indication of the ability of host minerals to uptake PuO_2^+ and potentially identify optimal mineral candidates for the sequestration of mobile contaminants.

This study represents a further development of the approach by Shuller et al. (2013) wherein incorporation of actinides is modelled by first evaluating solid source and sink phases, then including the transition to aqueous source and sink phases (Figure 4.1a), and then finally solid and aqueous phases incorporated into the bulk of the host mineral (Figure 4.1d). This study adds two intermediate steps to the process used by Shuller et al. (2013). While prior studies have only compared the energetics of a species dissolved in bulk solution and incorporated into a bulk solid, this study investigates the structure and energetics in, on, and within the surface layer to better understand the reaction sequence of incorporation (Becker et al., 2011; Rak et al., 2011, 2013; Saha and Becker, 2015; Shuller-Nickles et al., 2014; Shuller et al., 2010; Walker and Becker, 2015). In order to do this, redox species are evaluated independent of one another (Figure 4.1a). Then, PuO_2^+ is adsorbed to a cleaved surface layer of the host mineral (Figure 4.1b). Subsequently, PuO_2^+ is incorporated into a vacancy on the host mineral surface (Figure 4.1c) and then finally PuO_2^+ is incorporated into the bulk of the mineral host (Figure 4.1d). This new methodology allows us to assess the favorability of incorporation of

actinides onto the surface of host minerals alongside analogous calculations into the bulk of host minerals.

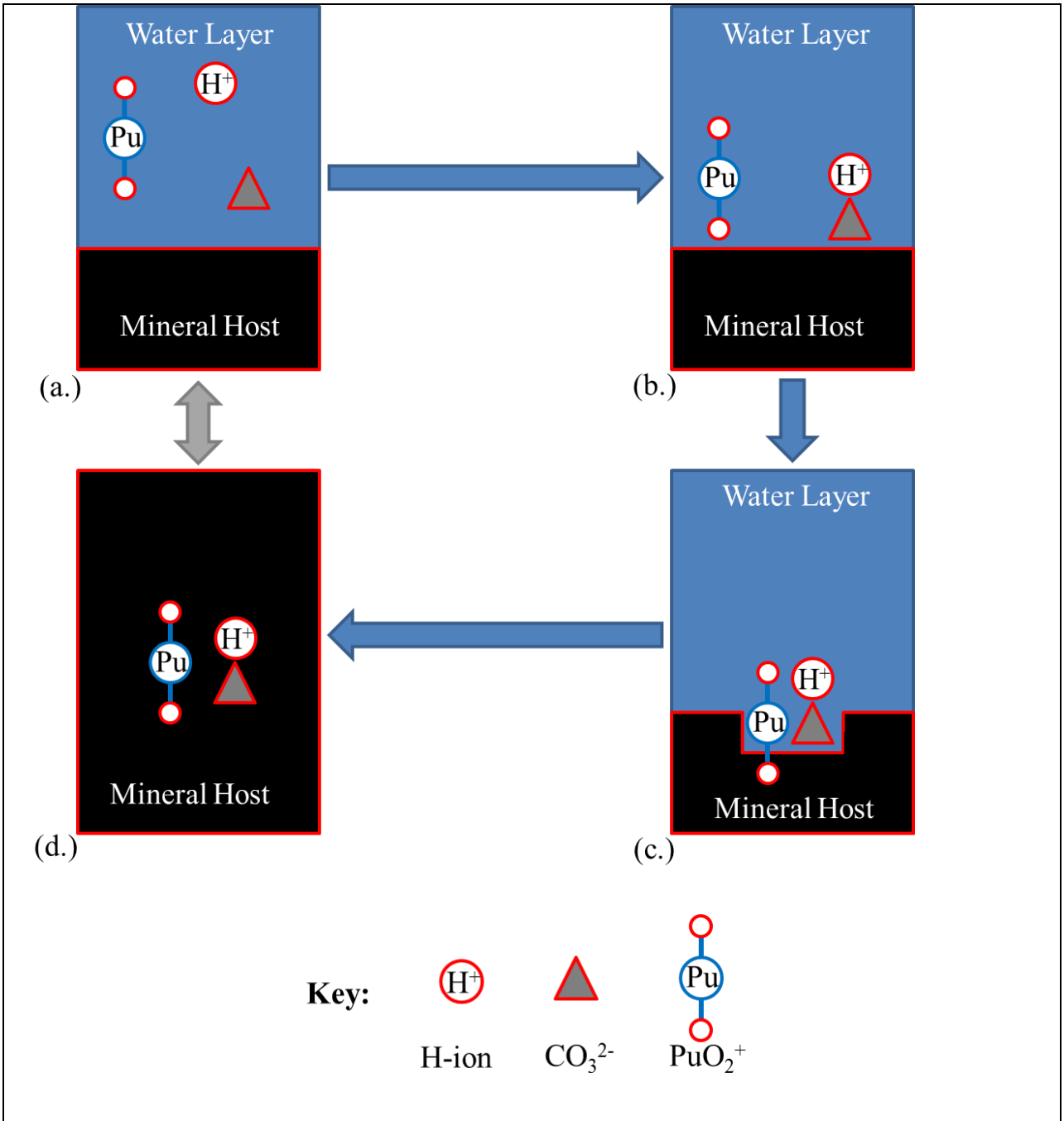

Figure 4.1: Simplified diagram of incorporation pathways for (an example) calcite ($CaCO_3$) host mineral. (a.) Host and incorporated species calculated separately. (b.) Adsorption of PuO_2^+ onto host surface. (c.) Incorporation of PuO_2^+ into the host surface layer. (d.) Incorporation of PuO_2^+ into the host bulk.

4.3 Materials and Methods

4.3.1 Solid Source and Sink

Calculations were performed using an *ab initio* approach; thereby the thermodynamic and structural properties of the system could be calculated independent of empirical factors as they often exist in classical force-field models. The Cambridge Serial Total Energy Package (CASTEP) module in Materials Studio 6.1.2 was used to calculate optimal geometry and total energy of periodic carbonate and sulfate species (Segall et al., 2002). Using Density Functional Theory (DFT) to approximate solutions to the wavefunctions (using planewaves as basis functions) of valence electrons, the approach chosen to approximate exchange-correlation effects was the Generalized Gradient Approximation (GGA) using the Perdew Burke Ernzerhof (PBE) functional (Perdew et al., 1996). For geometry optimizations, the convergence tolerance applied was $2.0 \cdot 10^{-5}$ eV/atom, using the Broyden-Fletcher-Goldfarb-Shanno (BFGS) algorithm. The cell was optimized for every structure except surface-incorporated Pu(V) structures and cluster molecules (molecule in a box). A spin-polarized approach was selected so that the three unpaired electron spins in the Pu(V) 5f orbitals would settle to their lowest energy configurations. Planewave expansion kinetic energy cutoff was set to 500 eV. Self-Consistent Field (SCF) cycles were set to a convergence tolerance of $2.0 \cdot 10^{-4}$ eV/atom or better and a convergence window of 3 or more. A k-point separation of 0.05 1/Å was used for sampling of the Brillouin zone. The ultrasoft pseudopotential scheme in the reciprocal space representation was used to describe core-electron interaction with 16 electrons in the valence band in the case of Pu. All settings, reaction calculations, and system configurations were kept consistent for each reaction in order to minimize systematic calculation errors.

As an example for sulfate structures, plutonyl incorporation onto the surface of celestine (Fig. 4.1b), $SrSO_4$ was first cleaved along the (001) growth face and a 10 Å vacuum region was added so that optimization calculations could be run in both CASTEP and DMol^3, and work function calculations could be implemented. A Sr^{2+} cation was then replaced by PuO_2^+ in the $SrSO_4$ structure. Charge balance was maintained by the addition of a hydrogen (H^+) ion in between the SO_4^{2-} and plutonyl ion such that geometry optimization could find the most energetically favorable position, *i.e.*, the highest affinity to what ion. This method was applied to the entire sulfate mineral group. Geometry optimization calculations were run before and after incorporation to refine structure and obtain final incorporation energy.

For the carbonate structures, plutonyl incorporation onto the surface of calcite and aragonite (Fig. 4.1b,c), calcite ($CaCO_3$) was first cleaved along its (104) growth face and aragonite along its (001) face. 10 Å vacuum regions were added and a single Ca^{2+} cation was replaced by PuO_2^+ in each respective $CaCO_3$ structure. Charge balance was maintained by the addition of a hydrogen atom to the CO_3^{2-} ion in the form of bicarbonate (HCO_3^-). Geometry optimization calculations were run before and after incorporation to refine the structures and obtain final configurations.

4.3.2 Aqueous Source and Sink

Calculations for the transition from solid source and sink phases to aqueous source and sink phases were performed with the Local Density Functional Calculations on *MOL*ecules (DMol^3) software package (Delley, 1990). This software was chosen due to it being one of the rare software packages that can perform cluster and periodic calculations (in contrast to CASTEP) while retaining almost identical settings (basis set, pseudopotentials, density functionals, COSMO approach of modeling surrounding water as a dielectric fluid). Computational

parameters were kept consistent by either using the DMol^3 and CASTEP software packages for evaluating the energies of all species in chemical equations. This is necessary because energies of individual species using different species cannot be compared; however, energies of reaction, each internally consistent but using different approaches from one another, can be combined in order to obtain an overall equation that contains (for example) charged hydrated molecular species and neutral infinite periodic crystals. The GGA scheme and PBE functional were used in conjunction with effective core potentials to account for core electrons (Dolg et al., 1987). To describe the atomic orbitals, Double Numerical plus D-functions (DND) were used as the basis set. All phases containing Pu(V) include a spin-polarized approach in order for the three unpaired electron spins in the 5f orbitals to adopt their lowest energy configuration. These actinide phases also include a Hubbard U correction of 4.0 eV chosen from literature to best match empirical findings and address Coulomb repulsion among the Pu 5f electrons (Ao et al., 2016; Chen et al., 2016; Hernandez and Holby, 2016; Jomard et al., 2008; Zhang et al., 2010). Hydration energies were evaluated using the Conductor-like Screening Model (COSMO), a dielectric continuum model to simulate ions imbedded in a dielectric fluid (Klamt and Schuurmann, 1993). Water with a dielectric constant of 78.54 was used as the solvent.

The reactions for Pu(V) incorporation calculated in this study concern the barite group [$BaSO_4$ (barite), $SrSO_4$ (celestine), $PbSO_4$ (anglesite), $CaSO_4$ (anhydrite)] and the $CaCO_3$ polymorphs calcite and aragonite.

4.4 Results and Discussion

4.4.1 Solid Source and Sink Reactions

To assess the favorability of Pu(V) incorporation into the bulk and onto the surface of each mineral investigated, reaction energies were calculated and compared. A stoichiometric chemical

equation that describes the replacement process was created using total-energy calculations for each species (Table 4.1). The sum of product energies subtracted from the sum of reactant energies gives the overall reaction energy. The overall reaction energy (incorporation energy) is the energy required to replace a Ca^{2+}, Sr^{2+}, Ba^{2+}, or Pb^{2+} cation with a PuO_2^{+} linear cation structure.

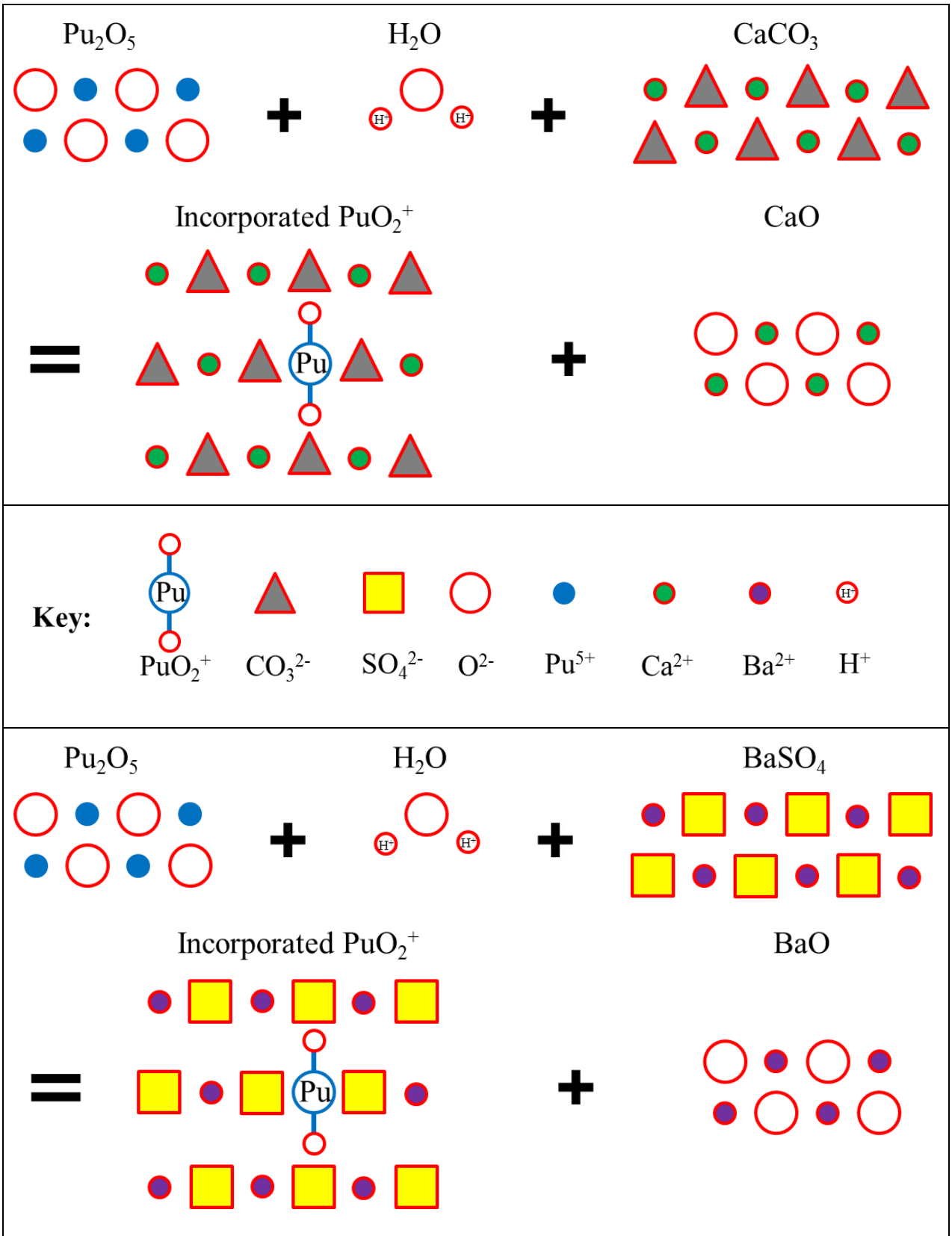

Figure 4.2: Simplified diagram of an example incorporation reaction. Host mineral ($CaCO_3$/$BaSO_4$) + Pu Source (Pu_2O_5) ⇌ Pu-Incorporated Host Mineral + Cation Sink (CaO/BaO)

Host mineral + Pu Source ⇌ Pu-Incorporated Mineral + Cation Sink

A standard approach for choosing sources and sinks is using metal oxides for the metals being replaced, ideally oxides in which the metals are in the same oxidation state as used in the replacement reactions. Given these criteria, the solid source for Pu is Pu_2O_5 and the sink phase for Ba^{2+} (in barite) would be BaO. One reason for the lack of a 1:1 replacement reaction is that the monovalent PuO_2^+ replaces a divalent cation (X^{2+}) and charge balancing is achieved by the addition of an H^+ or an H atom given up by water to the reactant side. A typical resulting equation is shown in Eqns. 1 & 2.

$$(XCO_3)_4 + ½(Pu_2O_5) + ½(H_2O) \rightleftharpoons (XCO_3)_3(PuO_2)(HCO_3) + (XO) \quad (1)$$

$$(XSO_4)_4 + ½(Pu_2O_5) + ½(H_2O) \rightleftharpoons (XSO_4)_3(PuO_2)(HSO_4) + (XO) \quad (2)$$

This approach yields the most meaningful results if all the phases in the equation are common materials in the environment and are all of the same type (*e.g.*, they are all solid, liquid, or gaseous species). However, as cation sinks, the alkaline earth oxides BaO, CaO, and SrO (and for anglesite PbO) are uncommon and chemically unstable. To address this, these oxides were converted into more environmentally-relevant and stable carbonates and sulfates (see Appendix Table 4.8 for the effect this has on ΔE_{rxn}).

$$(XCO_3)_4 + ½(Pu_2O_5) + ½(H_2O) + (CO_2) \rightleftharpoons (XCO_3)_3(PuO_2)(HCO_3) + (XCO_3) \quad (3)$$

$$(XSO_4)_4 + ½(Pu_2O_5) + ½(H_2O) + (SO_3) \rightleftharpoons (XSO_4)_3(PuO_2)(HSO_4) + (XSO_4) \quad (4)$$

To account for the Sr^{2+} and Ca^{2+} cations replaced by the plutonyl ion, SrO, CaO, PbO, and BaO species were added as the solid oxide sink phase. However, as these species are unstable and react with water or carbon dioxide to form stable complexes (*i.e.*, $Ca(OH)_2$ or $CaCO_3$), an additional reaction was applied to remove them from the final reactions (Roth et al., 1989). The

SrO, BaO, PbO, and CaO species were reacted with SO_3 or CO_2 to produce $SrSO_4$, $BaSO_4$, $PbSO_4$, $CaSO_4$ and $CaCO_3$ respectively, resulting in Equations 3 and 4. The SrO, CaO, PbO, and BaO unstable species could then be cancelled out and the reaction energies were lowered in each reaction by the respective values listed in Appendix Table 4.8 (on average -3.0 eV), resulting in the reactions below (examples: calcite and barite).

$$(CaCO_3)_4 + ½(Pu_2O_5) + ½(H_2O) + (CO_2) \rightleftharpoons (CaCO_3)_3(PuO_2)(HCO_3) + (CaCO_3) \quad (5)$$

$$(BaSO_4)_4 + ½(Pu_2O_5) + ½(H_2O) + (SO_3) \rightleftharpoons (BaSO_4)_3(PuO_2)(HSO_4) + (BaSO_4) \quad (6)$$

While Equations 1 & 2 tend to favor the left hand side because of the relative instability of alkaline earth oxides, Equations 3-6 are unfavorable on the left hand side because of the occurrence of gaseous species (CO_2 and SO_3). Equations 1-6 applied to both bulk and surface structures final reaction (incorporation) energies are shown in Appendix Table 4.9.

However, although CO_2 and SO_3 are more environmentally-relevant species, they do not apply to the conditions this study intends to describe. In aqueous environments (where PuO_2^+ is the dominant form of oxidized Pu in natural waters), CO_2 and SO_3 will react with H_2O to form H_2CO_3 and H_2SO_4. As such, this is taken into account in our calculations, resulting in the final reactions below (examples: calcite and barite).

$$(CaCO_3)_4 + ½(Pu_2O_5) + (H_2CO_3) \rightleftharpoons ½(H_2O) + (CaCO_3)_3(PuO_2)(HCO_3) + (CaCO_3) \quad (7)$$

$$(BaSO_4)_4 + ½(Pu_2O_5) + (H_2SO_4) \rightleftharpoons ½(H_2O) + (BaSO_4)_3(PuO_2)(HSO_4) + (BaSO_4) \quad (8)$$

Reactions 7 and 8 are applied to both bulk and surface structures and the final reaction (incorporation) energies are shown in Table 4.1.

For plutonyl incorporation into bulk periodic structures, each species in the carbonate and barite group was calculated before and after incorporation using identical settings as the cleaved

calculations, but because the bulk incorporations are fully periodic, the crystal unit cell was optimized in each run. The overall results show a higher favorability of PuO_2^+ incorporation into the bulk periodic lattice compared to incorporation onto the surface. Bulk incorporation is theoretically less favorable due to the highly ordered and rigid structure of the surrounding bulk unless there is a preexisting defect or vacancy. In addition, incorporation into the bulk would typically involve more reaction and therefore kinetic barriers. To address this juxtaposition and ascertain the true favorability in environmental conditions, we would have to evaluate different reaction pathways for different processes (*e.g.*, diffusion based, coprecipitation based), each with multiple activation barriers and that for different minerals. A true kinetic approach would therefore identify all activated complexes (intermediate structures) within the incorporation reaction path. Such calculations are beyond the scope of this study. Thus we replace this full kinetic approach by a stepwise thermodynamic approach, with the addition of aqueous molecular species in Section 4.4.2 that identifies the rate-controlling steps.

Two separate approaches were used in our calculations to provide the source of Pu for our incorporated Pu(V) species. The first method involved adding a pentavalent plutonyl periodic molecule, PuO_2^+ and gaseous O_2 as reactants. When applied, this approach produced highly negative (-3.6 to -7.2 eV) reaction energies for all structures. The more negative the reaction energy, the more favorable the incorporation reaction is to proceed. However, these highly favorable reactions seem unrealistic as such negative energies only occur for the most stable of molecular products (Shuller et al., 2010). The incorporation energies resulting from the use of a PuO_2^+ ion and gaseous O_2 and CO_2 reactants are only so negative due to the artifacts from putting charged ions in periodic calculations. Previous studies have used PuO_2 in the fluorite structure with an additional O atom in the octahedral interstitial position (a more stable

configuration) in order to obtain results comparable to PuO_2^+ experimental data (Petit et al., 2003). A second, more successful method involved the addition of a single, more stable Pu_2O_5 species (a possible solid phase for environmental plutonium) in lieu of these reactants (Paviet-Hartmann, 2012). Since to the authors' knowledge no structure for Pu_2O_5 is established in the literature, the initial structure for Pu_2O_5 was adapted from an Np_2O_5 crystal structure optimized for the high-spin state (Forbes et al., 2007; Shuller et al., 2010, 2013). Since Np(V) and Pu(V) species have similar properties and behave similarly in adsorption experiments, pentavalent neptunium can be used as an analog in such calculations (Keeney-Kennicutt and Morse, 1985). Applying this more environmentally-relevant approach (Pu_2O_5 source) to all structures resulted in a change of +9.6 eV to ΔE_{rxn} as calculated in Appendix Table 4.9.

Water is essential to the modeling of incorporation in aqueous systems. Thus H_2O was first calculated as a periodic molecule in the gaseous state, and then in order to add the intermolecular interactions in liquid water, the enthalpy of condensation of water (-0.41 eV per water molecule) was added. Applied to our reaction equations (½ H_2O) all final energies are increased by 0.205 eV as a result (Bryant, 1996). Similarly, with the addition of H_2SO_4 and H_2CO_3 in Equations 7 and 8, the enthalpy of formation (liquid) is applied for each, increasing final energies by 0.18 eV and 0.37 eV respectively.

Host Mineral	Bulk Incorporation	Surface Incorporation
barite	+0.46	+1.78
anglesite	+0.59	+2.48
celestine	+0.83	+3.06
anhydrite	+1.09	+2.75
aragonite	+0.95	+1.38
calcite	+0.64	+5.57

Table 4.1: Incorporation energies for PuO_2^+ incorporation into selected sulfate and carbonate host minerals using solid oxide sources and sinks. The reaction energy is calculated utilizing CASTEP with an assigned Hubbard U parameter of 4 eV using Eqns. 7 for carbonates and 8 for sulfates.

The final incorporation energy results for reactions utilizing Eqns. 7 and 8 for plutonyl (with the application of a Hubbard U parameter) is presented in Table 4.1. Based on these results, we find that the difference in incorporation energy between host minerals can be attributed to structural variation and ionic radius of the cation being replaced.

Based on the relative difference in reaction energies of anhydrite and aragonite as compared with calcite, we find that structural variation in host minerals is an important factor in incorporation energy and therefore favorability of incorporation. Though finding a trend between host mineral and incorporation energy is more straightforward in the simpler calculations in this study (see Appendix Table 4.9 and 4.10); the data presented in Table 4.1 utilizing all the transformations of equations listed above are nonetheless more accurate when one considers aqueous phases (see Section 4.4.2). Celestine, barite, anglesite, anhydrite, and aragonite all have (2/m 2/m 2/m) orthorhombic crystal symmetry, and as such, their incorporation energies are quite similar. They do however, differ in space group but more data is needed to assess the impact symmetry may have on incorporation energies. Calcite, on the other hand, has (3 2/m) trigonal crystal symmetry and as such the relative difference between it and anhydrite (0.45, 2.82 eV) is greater than that of aragonite and anhydrite (0.14, 1.37 eV). An alternative way to interpret the difference in calcite vs. aragonite incorporation energy for plutonyl is that aragonite is known to host larger cations (radius ≥ 1 Å) due to the higher coordination number (9 vs. 6 for calcite) which creates a longer cation-O distance. Conversely, smaller cations (radius < 1 Å) are known experimentally to be more enriched in calcite (Yoshimura et al., 2017). This finding is confirmed in Table 4.1 when considering surface incorporations, as aragonite has the lower, and therefore more favorable, incorporation energy. This, however, runs contrary to expectations

when considering bulk incorporation, as Table 4.1 shows that calcite has a lower incorporation energy than aragonite. This anomalous behavior is likely due to differences in structure, as the aragonite structure can support both surface and bulk incorporation without significant energy input, whereas the calcite structure can only support bulk incorporation. Furthermore, such observations in literature do not account for the replacement of a single cation site with an actinyl molecule. As shown in greater detail in Section 4.4.2, without surface incorporation, there is unlikely to be any great amount of bulk incorporation. Calcite and aragonite are also unique due to the flat nature of their trigonal CO_3^{2-} anion and its resulting sp^2 hybridization, which is capable of great distortion with little energy input as compared to the tetrahedral SO_4^{2-} anion and its more spherical sp^3 hybridization, for which any distortion requires a large energy input.

The local environment of the incorporation site is also an important factor for the stability of incorporated actinide species. PuO_2^+ can accommodate 6 coordinating ligands in the equatorial plane. Analysis of our bulk structures reveals that when incorporated into a barite ($BaSO_4$) host mineral, PuO_2^+ has a coordination number (CN) of 4, wherein the four surrounding SO_4^{2-} anions are monodentate with respect to PuO_2^+ (Figure 4.4c). Within a celestine ($SrSO_4$) host, PuO_2^+ has a coordination number of 5, wherein one of the original three surrounding bidentate SO_4^{2-} anions has rotated such that it has become monodentate with respect to PuO_2^+ - O (Figure 4.4a). Within an anhydrite host, before incorporation, the coordination number about the cation site for PuO_2^+ replacement was 6 with two bidentate SO_4^{2-} groups and two monodentate groups, and upon incorporation, the PuO_2^+ now has a coordination number of 4 with each of the surrounding four SO_4^{2-} groups in monodentate configuration (Figure 4.4d). With an aragonite host ($CaCO_3$), our data show CN = 6 (Ca^{2+}) prior to incorporation with three bidentate CO_3^{2-} anions. Upon replacement with PuO_2^+, one CO_3^{2-} anion has rotated slightly such that one Pu(V)-O distance is

~2.9 Å which is slightly beyond of what is expected for a coordinated anion (Figure 4.4b). The configuration for calcite ($CaCO_3$) is similar to that of aragonite except two of the three bidentate CO_3^{2-} anions have rotated so much that they are now monodentate (Figure 4.4e). Such significant local restructuring helps explain the large increase in incorporation energy from aragonite to calcite (especially at the surface).

The effect that cation ionic radius has on incorporation energies is far less pronounced than that of structural variation. However, the data show that reactions that incorporate PuO_2^+ into the Ba^{2+} (ionic radius of 1.35 Å) and Sr^{2+} (ionic radius of 1.18 Å) cation site have lower incorporation energies than reactions that replace a Ca^{2+} cation site (ionic radius of 0.99 Å) (Roth et al., 1989). The reason for this favorability into larger cation sites is likely due to the increase in available space within the crystal lattice and the decrease in the amount of lattice distortion necessary to accommodate the large PuO_2^+ linear cation structure (Pu(V) ionic radius of 0.74 Å; O^{2-} ionic radius of 1.4 Å) (Ankudinov et al., 1998). This trend is even more pronounced in calculations that do not include the Hubbard U parameter (see Appendix Table 4.10).

The surface incorporated species in Figure 4.3 display the distortion of the host mineral after incorporation of PuO_2^+ and geometry optimization to the lowest energy configuration. In celestine, all sulfate molecules rotate slightly. In aragonite, all carbonate groups rotate away from the PuO_2^+ and the bicarbonate molecule rotates almost perpendicular to its original orientation. In calcite, there is slight rotation in the surface region, especially in the carbonate anion opposite the bicarbonate. Relative lack of movement of the anion in the calcite structure vs. aragonite and celestine structure could account for the change in incorporation energies as a more rigid structure is less accommodating to the incorporation of a large linear oxo-cation group.

The solid oxide source and sink phase reactions in Equations 5 and 6 were also tested to a limited extent using the DMol^3 program, which exhibits largely the same trends as seen using CASTEP (see Appendix Table 4.11). The next section describes this conversion using Equations 7 and 8. This was performed in order to demonstrate the similarities between the two modules in anticipation of adding aqueous sources and sinks and solvation effects into our quantum chemical equations, rendering them more environmentally-relevant.

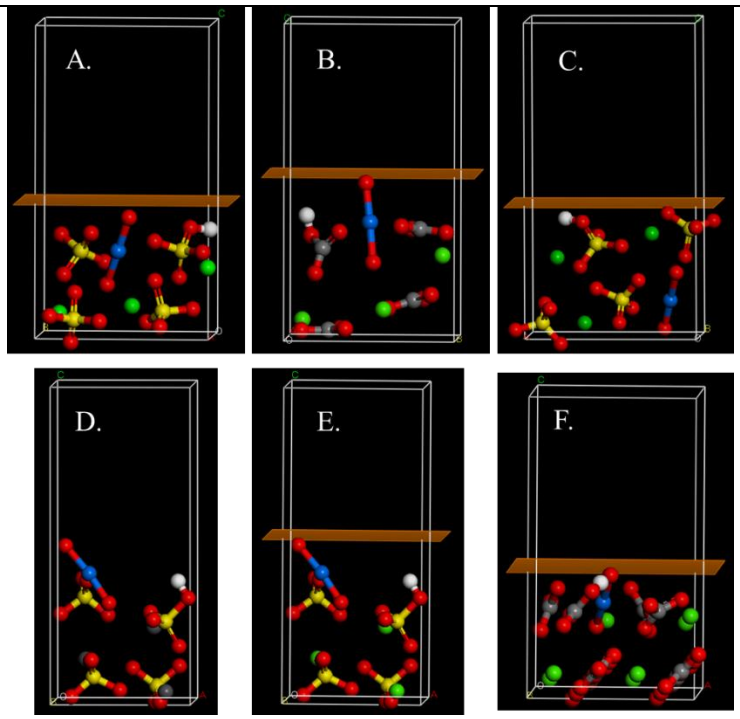

Figure 4.3: Plutonyl incorporated into the surface of A.) celestine ($SrSO_4$), B.) aragonite ($CaCO_3$), C.) barite ($BaSO_4$), D.) anglesite ($PbSO_4$), E.) anhydrite ($CaSO_4$), and F.) calcite ($CaCO_3$). In each cell, one divalent cation is replaced by a PuO_2^+ and H^+ for charge compensation. H: white, O: red, S: yellow, Ca, Sr, Ba: green, Pb: grey, Pu: blue.

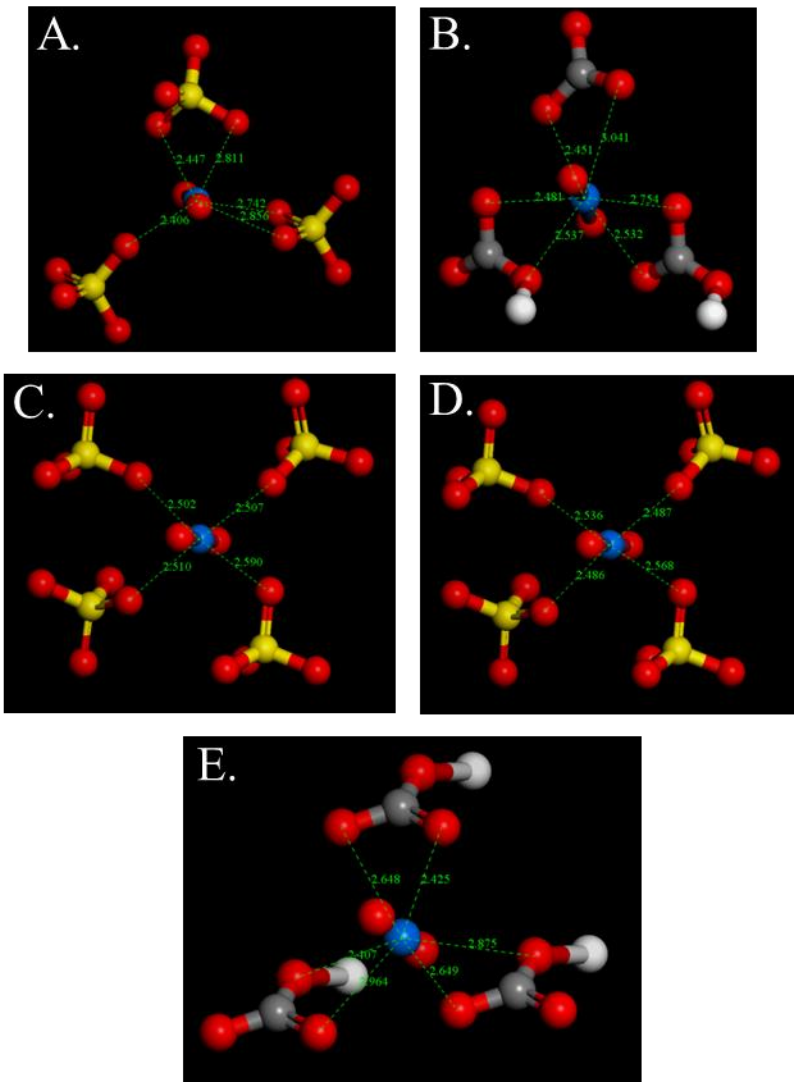

Figure 4.4: Coordination environment in the bulk of A.) celestine ($SrSO_4$), B.) aragonite ($CaCO_3$), C.) barite ($BaSO_4$), D.) anhydrite ($CaSO_4$), and E.) calcite ($CaCO_3$). H: white, O: red, S: yellow, Ca, Sr, Ba: green, Pu: blue.

4.4.2 Aqueous Source and Sink Reactions

The reactions described in Table 4.1 reflect the incorporation of plutonyl (V) onto carbonate and sulfate bulk and surface species using solid source and sink phases. As this study concerns the removal of Pu(V) from aqueous systems, a model of plutonium incorporation from an aqueous source requires the conversion of solid sources and sinks to aqueous complexes (Shuller et al., 2013). This conversion proves challenging due to the fact that the energy of reaction for a

given atomistic calculation can only be evaluated if all computational parameters are identical. This stipulation includes the configuration of all reaction species being evaluated. Thus, one can only obtain the overall reaction energy if the configurations of all species share the same periodicity (all clusters, all periodic, all aqueous, etc.) To account for this stipulation, we employ the method used by Shuller et al. (2013) wherein a series of chemical equations are employed, sharing the same configuration in each respective equation. Final energies for all reactions were then evaluated using the same quantum-mechanical approach, DMol^3 with GGA/PBE functional and the COSMO solvation model where applicable. These equations and their final reaction energies are then evaluated together, like terms are cancelled, and we can compute the overall reaction energy for the incorporation of aqueous ions (using cluster models) into periodic structures (using periodic models). Tables 4.2 and 4.3 demonstrate how this series of equations was implemented for incorporation of PuO_2^+ into sulfate and carbonate host minerals with barite and calcite as examples.

Table 4.2: Plutonyl (PuO_2^+) incorporation into barite ($BaSO_4$). Transformation from solid oxide to charged aqueous source and sink.

Solid Oxide Source and Sink Phase Reaction	**Δ*E* (eV)**
$(BaSO_4)_{4(s)} + ½Pu_2O_{5(s)} + ½H_2O_{(pbc\ m)} \rightarrow (BaSO_4)_3PuO_2(HSO_4)_{(s)} + BaO_{(s)}$	+5.24
Solid and Sink Conversion to Gas-Phase Periodic Molecules	
$PuO_2(OH)_{(pbc\ m)} \rightarrow ½Pu_2O_{5(s)} + ½H_2O_{(pbc\ m)}$	−3.47
$BaO_{(s)} + H_2O_{(pbc\ m)} \rightarrow Ba(OH)_{2(pbc\ m)}$	+1.52
Transition from Periodic Molecules to Gas-Phase Clusters	
$PuO_2(OH)_{(clus)} \rightarrow PuO_2(OH)_{(pbc\ m)}$	−0.14
$Ba(OH)_{2(pbc\ m)} + H_2O_{(clus)} \rightarrow Ba(OH)_{2(clus)} + H_2O_{(pbc\ m)}$	+0.09
Dissociation and Ionization of Clusters	
$PuO_2^+{}_{(clus)} + OH^-{}_{(clus)} \rightarrow PuO_2(OH)_{(clus)}$	−11.05
$Ba(OH)_{2(clus)} \rightarrow Ba^{2+}{}_{(clus)} + 2OH^-{}_{(clus)}$	+23.52
$H_3O^+{}_{(clus)} + OH^-{}_{(clus)} \rightarrow 2H_2O_{(clus)}$	−10.83
Hydration	
$PuO_2^+{}_{(aq)} \rightarrow PuO_2^+{}_{(clus)}$	+3.52
$Ba^{2+}{}_{(clus)} \rightarrow Ba^{2+}{}_{(aq)}$ (calculation)	−11.73
$Ba^{2+}{}_{(clus)} \rightarrow Ba^{2+}{}_{(aq)}$ (experiment [a])	−14 [a]
$H_3O^+{}_{(aq)} \rightarrow H_3O^+{}_{(clus)}$ (calculation)	+3.91
$H_3O^+{}_{(aq)} \rightarrow H_3O^+{}_{(clus)}$ (experiment [b])	+4.7 [b]
$H_2O_{(clus)} \rightarrow H_2O_{(aq)}$ (calculation)	−0.32
$H_2O_{(clus)} \rightarrow H_2O_{(aq)}$ (experiment [c])	−0.41 [c]
Overall Reaction	
$(BaSO_4)_{4(s)} + PuO_2^+{}_{(aq)} + H_3O^+{}_{(aq)} \rightarrow (BaSO_4)_3PuO_2(HSO_4)_{(s)} + Ba^{2+}{}_{(aq)} + H_2O_{(aq)}$	**+0.069**

Note: (pbc m) = molecule/cluster with periodic boundary conditions, "molecule in a box" (clus) = cluster/molecule in vacuum (gas phase); (*aq)* = hydrated (non-periodic) cluster, aqueous ion ([a]) experimental value from (Marcus, 1991) which has not been used for the sum in the overall equation; ([b]) from (Shuller et al., 2013), Δ*G* value; ([c]) enthalpy of condensation for water.

Table 4.3: Plutonyl (PuO_2^+) incorporation into calcite ($CaCO_3$). Transformation from solid oxide to charged aqueous source and sink.

Solid Oxide Source and Sink Phase Reaction	**ΔE (eV)**
$(CaCO_3)_{4(s)} + ½Pu_2O_{5(s)} + ½H_2O_{(pbc\ m)} \rightarrow (CaCO_3)_3PuO_2(HCO_3)_{(s)} + CaO_{(s)}$	+6.50
Solid and Sink Conversion to Gas-Phase Periodic Molecules	
$PuO_2(OH)_{(pbc\ m)} \rightarrow ½Pu_2O_{5(s)} + ½H_2O_{(pbc\ m)}$	−3.47
$CaO_{(s)} + H_2O_{(pbc\ m)} \rightarrow Ca(OH)_{2(pbc\ m)}$	+2.87
Transition from Periodic Molecules to Gas-Phase Clusters	
$PuO_2(OH)_{(clus)} \rightarrow PuO_2(OH)_{(pbc\ m)}$	−0.14
$Ca(OH)_{2(pbc\ m)} + H_2O_{(clus)} \rightarrow Ca(OH)_{2(clus)} + H_2O_{(pbc\ m)}$	+0.11
Dissociation and Ionization of Clusters	
$PuO_2^+{}_{(clus)} + OH^-{}_{(clus)} \rightarrow PuO_2(OH)_{(clus)}$	−11.05
$Ca(OH)_{2(clus)} \rightarrow Ca^{2+}{}_{(clus)} + 2OH^-{}_{(clus)}$	+24.51
$H_3O^+{}_{(clus)} + OH^-{}_{(clus)} \rightarrow 2H_2O_{(clus)}$	−10.83
Hydration	
$PuO_2^+{}_{(aq)} \rightarrow PuO_2^+{}_{(clus)}$	+3.52
$Ca^{2+}{}_{(clus)} \rightarrow Ca^{2+}{}_{(aq)}$ (calculation)	−12.73
$Ca^{2+}{}_{(clus)} \rightarrow Ca^{2+}{}_{(aq)}$ (experiment [a])	−14 [a]
$H_3O^+{}_{(aq)} \rightarrow H_3O^+{}_{(clus)}$ (calculation)	+3.91
$H_3O^+{}_{(aq)} \rightarrow H_3O^+{}_{(clus)}$ (experiment [b])	+4.7 [b]
$H_2O_{(clus)} \rightarrow H_2O_{(aq)}$ (calculation)	−0.32
$H_2O_{(clus)} \rightarrow H_2O_{(aq)}$ (experiment [c])	−0.41 [c]
Overall Reaction	
$(CaCO_3)_{4(s)} + PuO_2^+{}_{(aq)} + H_3O^+{}_{(aq)} \rightarrow (CaCO_3)_3PuO_2(HCO_3)_{(s)} + Ca^{2+}{}_{(aq)} + H_2O_{(aq)}$	**+2.65**

Note: (pbc m) = molecule/cluster with periodic boundary conditions, "molecule in a box" (clus) = cluster/molecule in vacuum (gas phase); (*aq)* = hydrated (non-periodic) cluster, aqueous ion ([a]) experimental value from (Marcus, 1991) which has not been used for the sum in the overall equation; ([b]) from (Shuller et al., 2013), ΔG value; ([c]) enthalpy of condensation for water.

The stepwise transition from solid source and sink phases to aqueous source and sink phases is as follows: 1) Solid source and sink phases are re-evaluated using the DMol^3 software package (previously done using CASTEP), the results of which can be found in Appendix Table 4.12. 2) Sources and sinks (Pu^{5+}) in the solid-state are substituted for neutral molecules constrained by periodic boundary conditions. These neutral molecules are essentially gas-phase molecules evaluated within the constraints of a 10×10×10 $Å^3$ unit cell. The comparatively large unit cell minimizes the interaction between molecules in adjacent unit cells. 3) The next step removes the periodic boundary conditions from the neutral molecular species, converting them into non-periodic cluster molecules. The low reaction energies at this step are due entirely to molecular dipole-dipole interactions between periodic molecules. 4) Neutral cluster molecules are then dissociated and ionized into charged gas-phase clusters. 5) Ion hydration energies are then evaluated by embedding ions in a dielectric continuum (COSMO model). The COSMO dielectric continuum model consistently underestimates the hydration energy of small ionic species such as Ca^{2+}, Ba^{2+}, Sr^{2+}, and Pb^{2+}. Because of this, various hydration energies were taken from literature and compared with our calculated values as shown in Table 4.4 (Marcus, 1994; Rashin and Honig, 1985; Shuller et al., 2013).

Species	COSMO (eV)	ΔH_{hyd} (eV)
Ba^{2+}	-11.73	-13.78 / -13.63
Pb^{2+}	-11.78	-16.27
Sr^{2+}	-12.29	-15.24 / -15.10
Ca^{2+}	-12.73	-16.58 / -16.63
OH^-	-4.19	-5.40 / -4.72

Table 4.4: Calculated hydration energies for small ionic species as compared with literature values (Marcus, 1994; Rashin and Honig, 1985; Shuller et al., 2013). The reaction energy is calculated utilizing DMol3 with the COSMO solvation model.

Host Mineral	Bulk Incorporation	Surface Incorporation
barite	+0.07	-1.65
anglesite	+0.09	-0.90
celestine	+0.66	-0.93
anhydrite	+0.92	-0.67
aragonite	+1.00	-0.59
calcite	+2.65	+1.07

Table 4.5: Incorporation energies for PuO_2^+ incorporation into selected sulfate and carbonate host minerals using aqueous sources and sinks as described in Tables 4.2 and 4.3. The reaction energy is calculated utilizing DMol^3 with the COSMO solvation model using Table 4.3 for carbonates and Table 4.2 for sulfates.

The final incorporation energies for PuO_2^+ incorporation into carbonate and sulfate host minerals using aqueous source and sink phases are listed in Table 4.5. The results have a similar trend as those of the solid source and sink phase calculations in Table 4.1. The most favorable host mineral for PuO_2^+ incorporation is barite, followed by anglesite, celestine, anhydrite, aragonite, and finally calcite as the least favorable. Only the relative favorability of aragonite and anhydrite has switched places and is within less than 1 eV for either solid or aqueous calculations.

Again, we find that structural variation in host minerals is an important factor in incorporation energy and therefore favorability. Our earlier findings demonstrating the favorability of minerals with (2/m 2/m 2/m) orthorhombic crystal symmetry with solid source and sink phase reactions are further supported by an even greater margin of incorporation energy difference in aqueous calculations. We find that the incorporation energy of calcite, with (3 2/m)

trigonal crystal symmetry, is 1.65 eV greater than that of aragonite with identical chemical formula but with (2/m 2/m 2/m) orthorhombic crystal symmetry.

The effect of cation ionic radius on incorporation energy is still less pronounced than that of crystal symmetry, but has an influence of up to 0.93 eV on E_{inc}. As cation ionic radius decreases ($Ba^{2+} > Pb^{2+} > Sr^{2+} > Ca^{2+}$) so too does overall E_{inc} (barite > anglesite > celestine > anhydrite > aragonite > calcite). These results again support our findings that the favorability of larger cation sites (*i.e.* ionic radii) are due to the increase in available interatomic distances in the crystal structure to lessen the amount of lattice displacement required to accommodate the large PuO_2^+ linear cation structure.

With the solid source and sink calculations, bulk incorporation was found to be less energy uphill than surface incorporation. With aqueous sources and sinks, this trend is reversed, with surface incorporation being more favorable than bulk incorporation. This inversion is expected as the inclusion of a dielectric fluid allows the contribution of surface energy (as a result of hanging surface bonds) to be realized in our results, which is discussed in greater depth in the next section.

4.4.2.1 Simulating Aqueous Adsorption

The use of a solvation model also allows for the consideration of plutonyl adsorption energy as shown in Figure 4.1b. Adsorption of PuO_2^+ was not attempted using solid sources and sinks as any energies obtained would of little use when applied to natural aqueous systems. Figure 4.5 demonstrates the step-by-step incorporation of PuO_2^+ into the bulk starting with free PuO_2^+ in solution using the host mineral barite as an example. Table 4.6 presents the results of these calculations in terms of the energy difference between the aqueous, adsorbed, surface incorporated, and bulk incorporated structures of each mineral host as exemplified by the arrows

in Figure 4.5. As the differences in the formation energies of each of the species illustrated in Figure 4.5 and Table 4.6 are primarily negative, Figure 4.6 represents the net change in energy between each structure simulated in order to better visualize which steps are endothermic (energy uphill) or exothermic (energy downhill).

Figure 4.5A represents the overall energy of a barite slab $(BaSO_4)_8$ with the addition of the energy of hydration of an individual plutonyl (PuO_2^+) and hydrogen sulfate (HSO_4^-). With the COSMO program, the best comparison between calculation and experiment is typically found by combining explicit water molecules with a dielectric fluid surrounding the first hydration sphere. This, compounded with the knowledge that COSMO consistently underestimates the hydration energies of smaller ionic species underscores the need for inclusion of the explicit waters using hydration energies from literature as shown in Tables 4.2 and 4.3 (Marcus, 1987, 1991, 1994; Renock et al., 2013). The energy E_1 in Figure 4.5 represents the change in energy from free PuO_2^+ and HSO_4^- in solution (Fig. 4.5A) to adsorbed to a barite surface (Fig. 4.5B), thus calculating the adsorption energy. This reaction is energetically downhill (Fig. 4.6) for every host mineral tested, indicating that it is energetically favorable for a plutonyl to adsorb to the mineral surface. This is likely the result of the electrostatic attraction the plutonyl species experiences when in proximity to the hanging bonds of a cleaved surface. Although this finding is encouraging for the removal of actinide materials from aqueous environments, desorption of the plutonyl could occur with a relatively minor input in energy (*e.g.* a slight change in solution chemistry).

Figure 4.5B represents the adsorbed species, wherein PuO_2^+ and HSO_4^- are close enough to interact with the surface and satisfy the hanging bonds. Energy E_2 indicates the energy required for the adsorbed species (Fig. 4.5B) to both replace a Ba^{2+} and SO_4^{2-} in a host mineral and release

them into solution. As a result of this two-step process, E_2 is positive (Fig. 4.6) for all mineral hosts, requiring a large energy input for surface incorporation (Fig. 4.5C).

Figure 4.5C displays the surface incorporated species, wherein a plutonyl and hydrogen sulfide have replaced a Ba^{2+} and SO_4^{2-}. As shown, the large rod-like PuO_2^+ has difficulty fitting into the ordered host mineral structure, and is most stable with half the linear dioxo structure sticking out of the surface vacancy. As seen with energy E_2, the energy E_3 represents the (relative) uphill energy input (Fig. 4.6) required for the aqueous species (Fig. 4.5A) to incorporate directly into the surface (Fig. 4.5C), or, the surface incorporation energy. Again, the reason E_2 and E_3 are positive in Fig. 4.6 for all mineral hosts in this study is due to the distortion that comes with incorporating a large molecule in the site formerly occupied by a single divalent cation. This trend is exaggerated in Fig. 4.5D, which demonstrates plutonyl incorporation into the bulk of the mineral host.

The bulk of a host mineral is even more highly ordered and resistant to deformation due to the rigid arrangement of the crystalline structure and the lack of an open-ended surface in which to relax. Thus, the energy E_4 is for the most part endothermic (Fig. 4.6) from mineral surface to mineral bulk incorporation. The exceptions found in Table 4.6 (barite and anglesite), consist of very small energy gains (-0.06 and -0.01 eV respectively). The reason for these two exceptions is likely a result of the inability of our calculations to fully account for the surface energy contribution from the surface incorporation structures due to the hanging surface bonds. The surface energy could only be approximated in this study by calculating the energy difference between mineral host surface and bulk structures. However, by accounting for the contributions due to surface energy, we have closed the gap between our opposing results using solid sources

and sinks vs. using aqueous sources and sinks, wherein E_4 was entirely negative or positive respectively.

The energy E_5 is representative of the entire incorporation process, starting with surface adsorption, then surface incorporation, followed by growth of the host mineral around the incorporated plutonyl, finally resulting in bulk incorporation (Fig. 4.5D), the bulk incorporation energy. E_5 is negative for all mineral hosts except calcite in this study, indicating that such incorporation does not require the net input of energy in order to occur, and thus is favorable for incorporation. However, as shown in Figure 4.6, bulk incorporation is energetically less favorable than adsorption, meaning that the input of energy will be necessary for adsorbed species to undergo bulk incorporation.

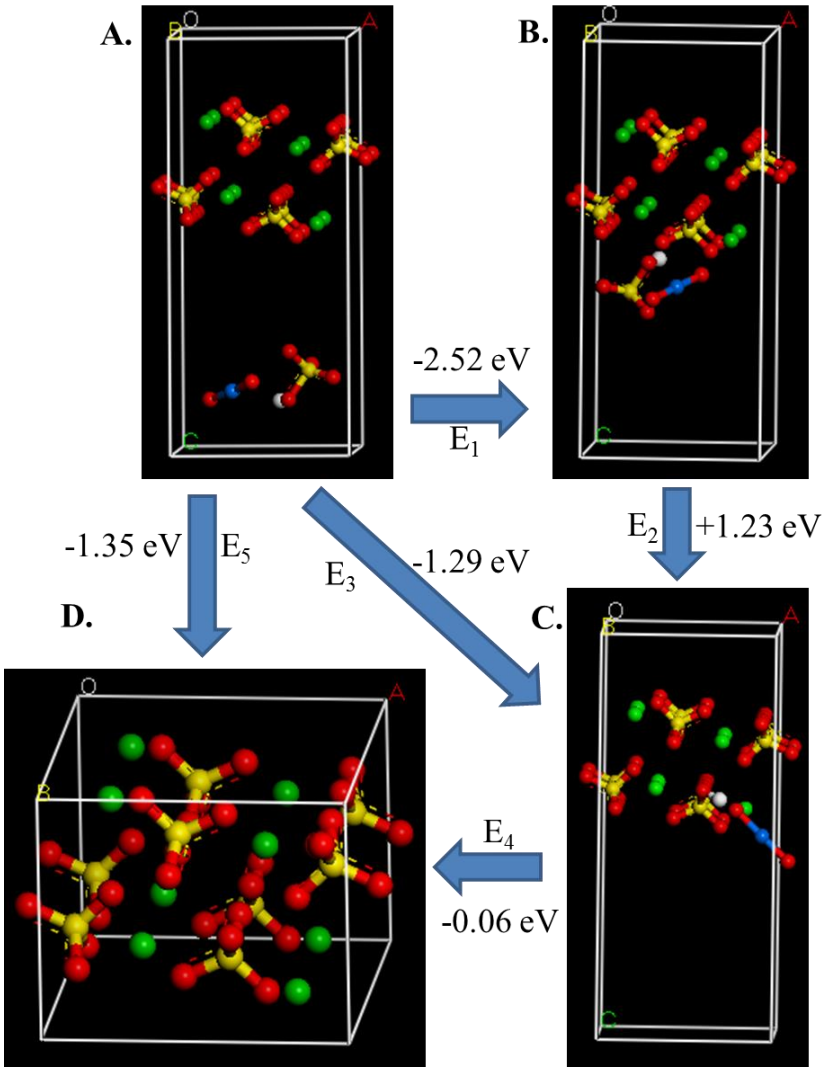

Figure 4.5: Example incorporation cycle for the barite mineral host. A.) aqueous PuO_2^+ and HSO_4^- with a host mineral surface. B.) PuO_2^+ and HSO_4^- adsorbed to a mineral surface. C.) PuO_2^+ and SO_4^{2-} incorporated into the surface of the host mineral, with a Ba^{2+} and SO_4^{2-} released into solution. D.) PuO_2^+ and HSO_4^- incorporated into the bulk mineral structure. E_1) the change in incorporation energy (E_{inc}) between structure (A) and (B). E_2) the change in E_{inc} between (B) and (C). E_3) the change in E_{inc} between (A) and (C). E_4) the change in E_{inc} between (C) and (D). E_5) the change in E_{inc} from (A) to (D).

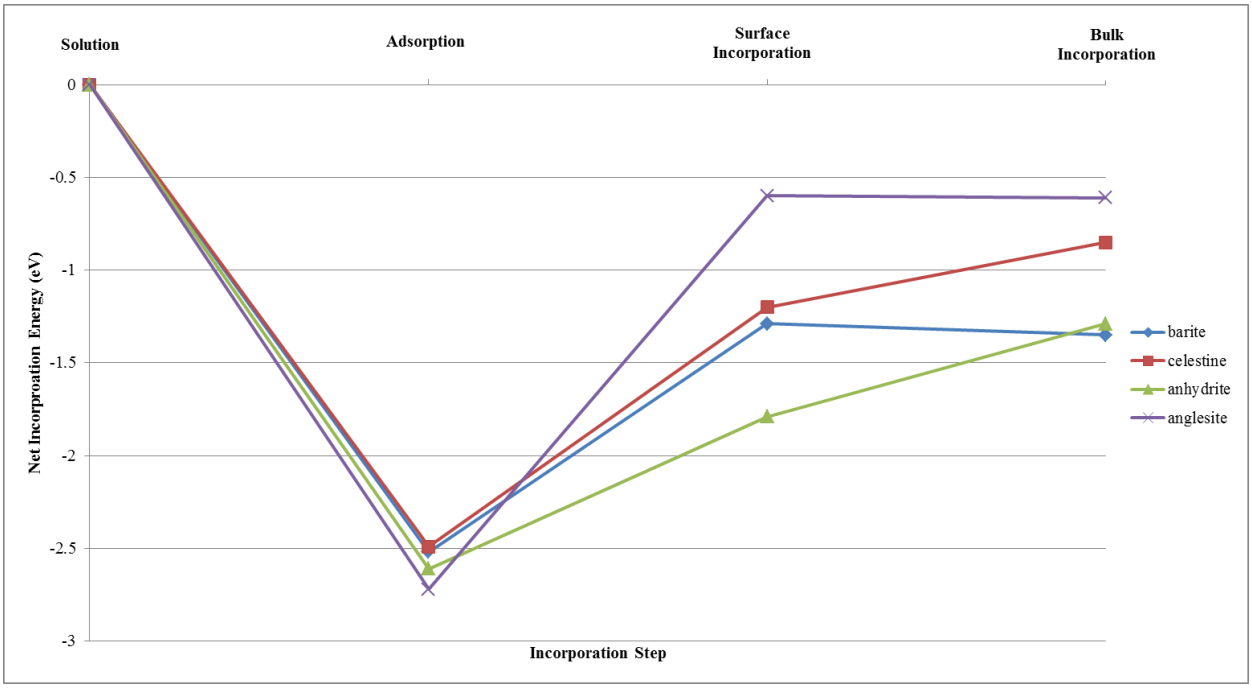

Figure 4.6: Incorporation cycle for all host minerals. Each step is representative of the net energy gain or loss (in eV) from each incorporation step from solution (starting point) to adsorption, surface incorporation, and finally to bulk incorporation.

Host Mineral	Solution → Adsorption (E_1)	Adsorption → Surface Incorp. (E_2)	Solution → Surface Incorp. (E_3)	Surface Incorp. → Bulk Incorp. (E_4)	Solution → Bulk Incorp. (E_5)
barite	-2.52	+1.23	-1.29	-0.06	-1.35
celestine	-2.49	+1.29	-1.20	+0.35	-0.85
anhydrite	-2.61	+0.81	-1.79	+0.50	-1.29
anglesite	-2.72	+2.12	-0.60	-0.01	-0.61
aragonite	-2.89	+0.87	-2.02	+0.20	-1.82
calcite	-1.24	+2.52	+1.28	+0.85	+2.13

Table 4.6: Incorporation energies for PuO_2^+ incorporation into selected sulfate and carbonate host minerals using aqueous sources and sinks as described using Equations 7 and 8. The reaction energy is calculated utilizing $DMol^3$ with COSMO solvation model using Equation 7 for carbonates and Equation 8 for sulfates.

4.4.3 Comparisons to Experiment

Pu(V)-O distances in our calculated structures compare well with experimentally determined Pu(V)-O distances obtained via extended x-ray absorption fine structure (EXAFS) spectroscopy (Table 4.7) (Ankudinov et al., 1998; Conradson et al., 2004).

Experimental Pu-O Distance: 1.84 Å	
Host Mineral	Calculated Pu-O Distance (Å)
barite	1.89 – 1.84
celestine	1.83 – 1.92
anhydrite	1.83 – 1.86
anglesite	1.89 – 1.80
aragonite	1.85 – 1.91
calcite	1.91 – 1.93

Table 4.7: Experimental vs. calculated Pu(V)-O distances. Calculations account for differing lengths for each of the two Pu-O bonds in PuO_2^+.

Our incorporated Pu(V)-(CO_3^-) nearest neighbor distances also compare well with x-ray absorption near edge structure (XANES) spectroscopy experimental values for single crystal carbonato complex distance of 2.5 Å. Nearest neighbor Pu(V)-(CO_3^-) distance for aragonite was calculated at 2.7 Å, and calcite at 2.4 Å. The similarity of our calculated values to experimental values indicate that our incorporated species compare with bonding environments similar to those found in natural systems (Conradson et al., 2004). No experimental values for nearest neighbor distances could be found for Pu(V)-(SO_4^-).

4.5 Conclusions

In this study, we have demonstrated the feasibility of PuO_2^+ incorporation into carbonate and sulfate structures using *ab initio* quantum mechanical methods. We have also demonstrated that plutonyl incorporation is a strongly selective process, favoring specific crystal structures and cation sites over others. Based on our calculated incorporation energetics we find that minerals

with (2/m 2/m 2/m) orthorhombic symmetry, accommodating coordination environments, and large cation ionic radii are the most favorable host minerals for PuO_2^+ incorporation. We have investigated two separate computational approaches to calculate the incorporation energies of barite-group sulfates and calcite polymorph host minerals. Starting with solid source and sink phases we used the CASTEP software package to calculate the energetics and structure of PuO_2^+ incorporation into bulk and the more environmentally-relevant surface structures. We then applied the method used by Shuller et al. (2013) to calculate the energetics and structure of PuO_2^+ incorporation into bulk and surface structures using aqueous source and sink phases. This method more accurately models the incorporation of actinides into mineral structures in aqueous environments. This aqueous approach allows for the calculation of each step in the incorporation process, from aqueous actinyl species to PuO_2^+ adsorption, to surface incorporation, and finally to bulk incorporation. We find that the adsorption of PuO_2^+ to common mineral surfaces is overall energetically downhill, indicating a preference for PuO_2^+ adsorption versus remaining in solution. From adsorption to incorporation into the mineral surface, the energy of incorporation is uphill, indicative of a thermodynamic resistance to the integration of the large PuO_2^+ ion into a crystalline surface. Despite this, we find that desorption of the actinyl back into solution is less energetically favorable than remaining in place or incorporating into the surface. If the mineral crystal is allowed to continue growing, we find the PuO_2^+ can become incorporated in the mineral bulk with the input of no more than an additional 0.5 eV, which is due to the high-energy dislocation formed by the actinyl in the crystalline structure.

Based upon the limited number of carbonate and sulfate structures calculated and the vast difference in computational approach, it is difficult to rank these minerals in a definitive order of their ability to uptake and immobilize aqueous pentavalent plutonyl. However, some mineral

hosts consistently result in the most favorable incorporation energies, such as barite and aragonite. These minerals underscore the finding that structures with orthorhombic symmetry (aragonite and calcite), large divalent cation sites (Ba^{2+}), and flexible CO_3^{2-} anion sp^3 hybridization (aragonite) are the most favorable for incorporation and immobilization of large actinyl species.

These findings lay the groundwork for a search for a host mineral that is both highly favorable for actinide incorporation and benign to natural aqueous systems in which it could be applied as a preventative or clean-up method in the event of contamination. As plutonium experimentation is both highly dangerous and costly, the exploration can start with further computational study, perhaps involving high-throughput calculation, narrowing a broad mineralogical search down to a selection of host compounds that can eventually be tested in the laboratory then applied to practical situations such as the continuing contamination of sites like the Hanford Nuclear Reservation in Washington and the reactors in Fukushima Province, Japan.

4.6 Further Research

This study demonstrates the feasibility of pentavalent plutonyl incorporation into carbonate and sulfate mineral structures. It is however, only a beginning. Further study is being undertaken presently to address the limitations of this paper. To expand the range of our incorporation data concerning structural and cation effects, we aim to assess Pu(V) uptake within uncommon carbonate and sulfate host minerals hashemite and vaterite. Additionally, we will investigate the kinetic barrier between bulk and surface incorporations and the favorability of incorporation into existing defects in host minerals. The surface energy contribution of hanging bonds will be further investigated using far larger mineral surfaces in order to minimize the single point energy contribution. We will calculate the electronic and vibrational entropy for each phase in all

reactions and obtain the Gibbs free energy (ΔG), a more accurate and integral term for total energy calculations. ΔG values are more easily compared to experimental values in literature. Finally, we will investigate further the effects of adding explicit water molecules to aqueous species for hydration calculations. Addition of 1st and 2nd hydration spheres more accurately model natural aqueous geochemical conditions. We hope that our following paper will add pertinent information concerning the incorporation of Pu(V) into mineral structures and onto mineral surfaces, as well as paving the way for future experimental studies.

4.7 Acknowledgements

We gratefully acknowledge the Department of Energy: Heavy Element Chemistry grant DE-FG02-06ER14783 for support.

4.8 Appendix

A. Supplementary Calculations

Reaction	ΔE_{rxn} (eV)
$BaO + SO_3 = BaSO_4$	-4.4
$PbO + SO_3 = PbSO_4$	-2.4
$SrO + SO_3 = SrSO_4$	-3.7
$CaO + SO_3 = CaSO_4$	-3.2
$CaO + CO_2 = CaCO_3$	-1.6

Table 4.8 - Appendix: Unstable SrO, CaO, PbO, and BaO species are removed from reaction (1) and (2). The reaction energy is calculated utilizing CASTEP.

Host Mineral	Bulk Incorporation Hubbard U = 0 eV	Surface Incorporation Hubbard U = 0 eV	Bulk Incorporation Hubbard U = 4 eV	Surface Incorporation Hubbard U = 4 eV
barite	+0.02	+1.55	-0.20	+1.12
anglesite	+0.40	+2.13	-0.08	+1.82
celestine	+1.10	+2.14	+0.17	+2.40
anhydrite	+1.35	+2.33	+0.43	+2.09
aragonite	+1.18	+2.76	+0.99	+1.42
calcite	+3.17	+5.96	+0.68	+5.60

Table 4.9 - Appendix: Incorporation energies for PuO_2^+ incorporation into selected sulfate and carbonate host minerals using solid oxide sources and sinks. The reaction energy is calculated utilizing CASTEP with and without an assigned Hubbard U parameter using Eqns. 5 for carbonates and 6 for sulfates.

Host Mineral	Bulk Incorporation	Surface Incorporation
barite	+0.93	+2.45
anglesite	+1.31	+3.04
celestine	+2.01	+3.04
anhydrite	+2.26	+3.24
aragonite	+1.19	+2.77
calcite	+3.19	+5.98

Table 4.10 - Appendix: Incorporation energies for PuO_2^+ incorporation into selected sulfate and carbonate host minerals using solid oxide sources and sinks. The reaction energy is calculated utilizing CASTEP without an assigned Hubbard U parameter using Eqns. 7 for carbonates and 8 for sulfates.

Host Mineral	Bulk Incorporation	Surface Incorporation
barite	+0.28	+0.07
anglesite	+0.66	
celestine	+1.36	
anhydrite	+2.80	+2.59
aragonite	+2.02	
calcite		

Table 4.11 - Appendix: Incorporation energies for PuO_2^+ incorporation into selected sulfate and carbonate host minerals using solid oxide sources and sinks. The reaction energy is calculated utilizing $DMol^3$ using Eqns. 5 for carbonates and 6 for sulfates.

Host Mineral	Bulk Incorporation	Surface Incorporation
barite	+3.52	
anglesite		
celestine	+5.90	
anhydrite	+4.77	
aragonite	+4.85	
calcite	+6.50	

Table 4.12 - Appendix: Incorporation energies for PuO_2^+ incorporation into selected sulfate and carbonate host minerals using solid oxide sources and sinks. The reaction energy is calculated utilizing $DMol^3$ using Eqns. 5 for carbonates and 6 for sulfates.

4.9 Works Cited

Ankudinov, A.L., Conradson, S.D., de Leon, J.M. and Rehr, J.J. (1998) Relativistic XANES calculations of Pu hydrates. *Physical Review B* **57**, 7518-7525.

Ao, B.Y., Qiu, R.Z., Lu, H.Y. and Chen, P.H. (2016) First-principles DFT plus U calculations on the energetics of Ga in Pu, Pu2O3 and PuO2. *Computational Materials Science* **122**, 263-271.

Becker, U., Shuller, L.C., Ewing, R.C. and Rak, Z. (2011) Actinide incorporation into uranyl alteration phases and garnets. *Abstr Pap Am Chem S* **242**.

Bruno, J. and Ewing, R.C. (2006) Spent nuclear fuel. *Elements* **2**, 343-349.

Bryant, R.G. (1996) The dynamics of water-protein interactions. *Annu. Rev. Biophys. Biomol. Struct.* **25**, 29-53.

Burns, P.C., Ewing, R.C. and Miller, M.L. (1997) Incorporation mechanisms of actinide elements into the structures of U^{6+} phases formed during the oxidation of spent nuclear fuel. *J. Nucl. Mater.* **245**, 1-9.

Chen, J., Meng, D.Q., Chen, Q.Y. and Luo, W.H. (2016) Electronic structure and optical properties of plutonium dioxide from first-principles calculations. *Rare Metals* **35**, 643-648.

Choppin, G.R. (2007) Actinide speciation in the environment. *J. Radioanal. Nucl. Chem.* **273**, 695-703.

Conradson, S.D., Abney, K.D., Begg, B.D., Brady, E.D., Clark, D.L., den Auwer, C., Ding, M., Dorhout, P.K., Espinosa-Faller, F.J., Gordon, P.L., Haire, R.G., Hess, N.J., Hess, R.F., Keogh, D.W., Lander, G.H., Lupinetti, A.J., Morales, L.A., Neu, M.P., Palmer, P.D., Paviet-Hartmann, P., Reilly, S.D., Runde, W.H., Tait, C.D., Veirs, D.K. and Wastin, F. (2004) Higher order speciation effects on plutonium L_3 x-ray absorption near edge spectra. *Inorg. Chem.* **43**, 116-131.

Delley, B. (1990) An all-electron numerical method for solving the local density functional for polyatomic molecules. *J. Chem. Phys.* **92**, 508-517.

Dolg, M., Wedig, U., Stoll, H. and Preuss, H. (1987) Energy-adjusted ab initio pseudopotentials for the first row transition elements. *J. Chem. Phys.*, 866-872.

Ewing, R.C. (2015) Long-term storage of spent nuclear fuel. *Nat Mater* **14**, 252-257.

Forbes, T.Z., Burns, P.C., Skanthakumar, S. and Soderholm, L. (2007) Synthesis, structure, and magnetism of Np_2O_5. *J. Am. Chem. Soc.* **129**, 2760-+.

Hernandez, S.C. and Holby, E.F. (2016) DFT + U study of chemical impurities in PuO_2. *Journal of Physical Chemistry C* **120**, 13095-13102.

Jomard, G., Amadon, B., Bottin, F. and Torrent, M. (2008) Structural, thermodynamic, and electronic properties of plutonium oxides from first principles. *Physical Review B* **78**.

Kaplan, A.C., Henzl, V., Menloye, H.O., Swinhoe, M.T., Behan, A.P., Flaska, M. and Pozzi, S.A. (2014) Determination of total plutonium content in spent nuclear fuel assemblies with the differential die-away self-interrogation instrument. *Nuclear Instruments & Methods in Physics Research Section a-Accelerators Spectrometers Detectors and Associated Equipment* **764**, 347-351.

Keeney-Kennicutt, W.L. and Morse, J.W. (1985) The redox chemistry of $Pu(V)O_2^+$ interaction with common mineral surfaces in dilute-solutions and seawater. *Geochim. Cosmochim. Acta* **49**, 2577-2588.

Klamt, A. and Schuurmann, G. (1993) Cosmo - a new approach to dielectric screening in solvents with explicit expressions for the screening energy and its gradient. *Journal of the Chemical Society-Perkin Transactions 2*, 799-805.

Lantzos, I., Kouvalaki, C. and Nicolaou, G. (2015) Plutonium fingerprinting in nuclear forensics of spent nuclear fuel. *Progress in Nuclear Energy* **85**, 333-336.

Marcus, Y. (1987) The thermodynamics of solvation of ions .2. The enthalpy of hydration at 298.15-K. *Journal of the Chemical Society-Faraday Transactions I* **83**, 339-349.

Marcus, Y. (1991) Thermodynamics of solvation of ions .5. Gibbs free-energy of hydration at 298.15-K. *Journal of the Chemical Society-Faraday Transactions* **87**, 2995-2999.

Marcus, Y. (1994) A simple empirical-model describing the thermodynamics of hydration of ions of widely varying charges, sizes, and shapes. *Biophys. Chem.* **51**, 111-127.

Orlandini, K.A., Penrose, W.R. and Nelson, D.M. (1986) Pu(V) as the stable form of oxidized plutonium in natural-waters. *Mar. Chem.* **18**, 49-57.

Paviet-Hartmann, P. (2012) Plutonium Chemistry, Radiochemistry Webinar. National Analytical Management Program (NAMP).

Perdew, J.P., Burke, K. and Ernzerhof, M. (1996) Generalized gradient approximation made simple. *Phys. Rev. Lett.* **77**, 3865-3868.

Petit, L., Svane, A., Szotek, Z. and Temmerman, W.M. (2003) First-principles calculations of $PuO_{2+/-x}$. *Science* **301**, 498-501.

Powell, B.A. (2012) Environmental chemistry of uranium and plutonium. *Actinide Chemistry Series*.

Rak, Z., Ewing, R.C. and Becker, U. (2011) Ab initio investigation of actinide incorporation in Ti, Zr, Hf, and Sn-containing garnet structure. *Abstr Pap Am Chem S* **241**.

Rak, Z., Ewing, R.C. and Becker, U. (2013) Ferric garnet matrices for immobilization of actinides. *J. Nucl. Mater.* **436**, 1-7.

Rashin, A.A. and Honig, B. (1985) Reevaluation of the born model of ion hydration. *J. Phys. Chem.* **89**, 5588-5593.

Renock, D., Mueller, M., Yuan, K., Ewing, R.C. and Becker, U. (2013) The energetics and kinetics of uranyl reduction on pyrite, hematite, and magnetite surfaces: A powder microelectrode study. *Geochim. Cosmochim. Acta* **118**, 56-71.

Roth, R.S., Rawn, C.J., Ritter, J.J. and Burton, B.P. (1989) Phase-equilibria of the system SrO-CaO-CuO. *J. Am. Ceram. Soc.* **72**, 1545-1549.

Saha, S. and Becker, U. (2015) The effect of the aliphatic carboxylate linkers on the electronic structures, chemical bonding and optical properties of the uranium-based metal-organic frameworks. *Rsc Advances* **5**, 26735-26748.

Segall, M.D., Lindan, P.J.D., Probert, M.J., Pickard, C.J., Hasnip, P.J., Clark, S.J. and Payne, M.C. (2002) First-principles simulation: ideas, illustrations and the CASTEP code. *Journal of Physics-Condensed Matter* **14**, 2717-2744.

Shuller-Nickles, L.C., Bender, W.M., Walker, S.M. and Becker, U. (2014) Quantum-mechanical methods for quantifying incorporation of contaminants in proximal minerals. *Minerals* **4**, 690-715.

Shuller, L.C., Ewing, R.C. and Becker, U. (2010) Quantum-mechanical evaluation of Np-incorporation into studtite. *Am. Mineral.* **95**, 1151-1160.

Shuller, L.C., Ewing, R.C. and Becker, U. (2013) Np-incorporation into uranyl phases: A quantum-mechanical evaluation. *J. Nucl. Mater.* **434**, 440-450.

Steele, H. and Taylor, R.J. (2007) A theoretical study of the inner-sphere disproportionation reaction mechanism of the pentavalent actinyl ions. *Inorg. Chem.* **46**, 6311-6318.

Topin, S. and Aupiais, J. (2016) The pentavalent actinide solution chemistry in the environment. *Journal of Environmental Radioactivity* **153**, 237-244.

Walker, S.M. and Becker, U. (2015) Uranyl (VI) and neptunyl (V) incorporation in carbonate and sulfate minerals: Insight from first-principles. *Geochim. Cosmochim. Acta* **161**, 19-35.

Wiss, T., Hiernaut, J.P., Roudil, D., Colle, J.Y., Maugeri, E., Talip, Z., Janssen, A., Rondinella, V., Konings, R.J.M., Matzke, H.J. and Weber, W.J. (2014) Evolution of spent nuclear fuel in dry storage conditions for millennia and beyond. *J. Nucl. Mater.* **451**, 198-206.

Yoshimura, T., Tamenori, Y., Suzuki, A., Kawahata, H., Iwasaki, N., Hasegawa, H., Nguyen, L.T., Kuroyanagi, A., Yamazaki, T., Kuroda, J. and Ohkouchi, N. (2017) Altervalent substitution of sodium for calcium in biogenic calcite and aragonite. *Geochim. Cosmochim. Acta* **202**, 21-38.

Zhang, P., Wang, B.T. and Zhao, X.G. (2010) Ground-state properties and high-pressure behavior of plutonium dioxide: Density functional theory calculations. *Physical Review B* **82**.

CHAPTER 5

Conclusions

The research in this dissertation comprised a multi-method approach employed to understand the redox and sorption effects on mineral surfaces that control actinide mobility within the environment. Novel approaches combining electrochemistry with surface probe imaging, spectroscopy, and atomistic modeling were utilized in order to probe the redox reaction mechanisms, structure, thermodynamics, and kinetics of actinide complexes. This combination of experiment and calculation yielded results unique to existing literature, as well as a more detailed and fundamental understanding of reactions at the mineral-water interface from a macroscopic to atomistic level.

The results from Chapter 2 described the redox reaction mechanisms of the unique and poorly-understood uranyl peroxide cluster U_{60}. This study represents the sole electrochemical investigation of U_{60} in the literature and only the second of any uranyl peroxide nanocluster. There is evidence for the ability of U_{60} to switch from a U(VI) to U(V) oxidation state with and without disruption of the cluster (and probably both at different ratios occurring at the same time, depending on solution conditions, redox potential, and time of reduction). This may be due to the formation of a superoxo complex of U(V). There is evidence that disproportionation of U(V) to U(VI) and U(IV) is occurring if the reduced state of U is held for a certain amount of time but it remains unclear at what rate and time scale. Future experiments, for example using *in situ*

Raman or synchrotron XAS, may help distinguish what fraction of reduced U stays within the cluster. As U_{60} is reduced to U(IV), peroxide linkers maintaining the structure of the clusters are simultaneously reduced to OH^-, the result of which is the irreversible destruction of clusters at the peroxide sites. Results from a combined approach by means of electrochemistry and computational modeling elucidated the contribution of multiple aqueous uranyl species as a mechanistic explanation for the anomalous pH-dependence of U_{60} redox reactions. Furthermore, this multi-method approach demonstrated on an atomistic level how solution chemistry can shift redox peak position, giving a general magnitude and direction of redox peak shift in cyclic voltammetry. These findings suggest a future research direction analyzing peak shifts in voltammograms (which are often glossed over and attributed to the influence of differing ligands), thereby quantifying energies of adsorption, incorporation, and complexation. This analysis is essential to learn more from the interplay between molecular simulations and electrochemical peak shifts.

Building upon the results from U_{60} electrochemistry, Chapter 3 investigated the application of EC-AFM, a technique most commonly used for the study of electrode materials for batteries, though rarely used to solve problems in actinide geochemistry (Burt et al., 2005; Higgins et al., 1996; Walker et al., 2016; Wen et al., 2013). As U_{60} has the potential to self-assemble and enter aqueous systems under certain conditions, the use of EC-AFM has proved to be an effective tool in the study of deposition and dissolution of redox-active actinide contaminants on substrate surfaces. The combination of electrochemical methods with AFM has allowed the imaging of the never-before observed deposition of U_{60} and its dissolution products, *in situ*, on a steel substrate surface polarized at reducing and oxidizing conditions without the use of interfering redox solutions. With the aid of spectroscopic techniques such as SEM, EDS, and AES to analyze

reaction products, results show that U_{60} solutions deposit three types of sorbates: U_{60} fullerene crystals consistent with the formation of macroscopic FCC U_{60} crystals, composite clusters of U_{60} fullerenes, and large deposits of ~10 nm uranium oxide needles that likely form from the dissolution of U_{60} clusters into UO_2^{2+}. At neutral (OCP) and oxidizing (+500 mV) conditions, these sorbates exhibit Oswald ripening, with large numbers of small sorbates becoming a smaller number of large sorbates over time. Reducing (-500 mV) conditions bring about a surge in small sorbate growth and larger sorbate volumes over similar timescales. High-resolution SEM reveals distinct fibrous nanoparticles interlinking composite clusters of U_{60} fullerenes reminiscent of carbon nanotubes. Future studies expanding upon this multi-method approach could investigate links between peroxide bonding and nanotube formation, refine the efficiency of U_{60} production by close observation of its assembly and growth at the substrate-fluid interface, and further characterize nanocluster behavior and integrity at substrate surfaces at different solution chemistries. These methods of describing the stability and redox behavior of U_{60} will aid efforts to discover the conditions at which its dissolution products could be released into the environment.

Chapter 4 utilized a unique combination of different types of *ab initio* quantum-mechanical models (for periodic, cluster, and surface structures) to simulate how actinide contaminants can be immobilized in mineral species via adsorption to surfaces, incorporation within surfaces, and incorporation into the crystalline bulk. This computational approach allowed us to model how hydrated species interact with a mineral host and calculate thermodynamic properties as an approach independent of experiments, the latter of which seldom reflect equilibrium conditions. This approach also allows for the straightforward investigation of actinide elements that are exceedingly rare or dangerous, in this case, the highly mobile PuO_2^+ ion. Through the use of a

novel method of including the effects of hydration, cluster models, surface energy, and Hubbard U parameters, our results could closely approximate real-world conditions with the energy required to immobilize PuO_2^+ lowered by as much as 1.5 eV when compared to previous computational approaches. Furthermore, we found that the adsorption of PuO_2^+ to common mineral surfaces (carbonates and sulfates) is energetically downhill, indicating a predisposition for PuO_2^+ adsorption versus remaining in solution. From adsorption to incorporation into the mineral surface, the energy of incorporation is uphill, indicative of a thermodynamic resistance to the integration of the large PuO_2^+ ion into a crystalline surface. Despite this, we found that desorption of the actinyl back into solution is less energetically favorable than remaining in place or incorporating into the surface. If the mineral crystal is allowed to continue growing, we find the PuO_2^+ can become incorporated in the mineral bulk with the input of no more than an additional 0.5 eV, which is due to the high-energy dislocation formed by the actinyl in the crystalline structure. PuO_2^+ is the dominant form of oxidized Pu found in contaminated sites and being highly soluble, is challenging to mitigate in aqueous environments. By modeling the basic reactions that would take place between a contaminant plume and carbonate and sulfate rock, this study paves the way for more detailed, surface-oriented studies that rapidly characterize suitable minerals for the immobilization of actinide contaminants. Although Chapter 4, unlike Chapters 2 and 3, does not concern the effects of redox reactions catalyzed by mineral surfaces, it could be easily extended to account for them. Moreover, actinide removal experiments, larger unit cells, crystal defects, macroscopic calculations, or case studies specific to the rock chemistry of sites contaminated with Pu represent an important future direction for this study.

This dissertation utilized novel experimental and computational approaches to obtain a deeper understanding of actinide mobility, chemistry, and redox behavior. Electrochemical

experiments, complimented by the use of AFM, computational models, and spectroscopic techniques were utilized to identify reaction pathways and mechanisms affecting actinide mobility in natural systems. Molecular simulations were used extensively to analyze the energetics and kinetics of actinide interactions at mineral surfaces. This multi-method approach contributes to existing knowledge and develops future experimental and computational models to more accurately characterize the interaction of actinide contaminants at the mineral-fluid interface. This knowledge is essential for *in situ* remediation methods such as permeable reactive barriers and mineralization.

5.1 Works Cited

Burt, D.P., Wilson, N.R., Weaver, J.M.R., Dobson, P.S. and Macpherson, J.V. (2005) Nanowire probes for high resolution combined scanning electrochemical Microscopy - Atomic force Microscopy. *Nano Lett.* **5**, 639-643.

Higgins, S.R., Hamers, R.J. and Banfield, J.F. (1996) In-situ real-time imaging of the surface reactions of metal sulfide minerals with electrochemical STM. *Abstr Pap Am Chem S* **211**, 70-COLL.

Walker, S.M., Marcano, M.C., Bender, W.M. and Becker, U. (2016) Imaging the reduction of chromium(VI) on magnetite surfaces using in situ electrochemical AFM. *Chem. Geol.* **429**, 60-74.

Wen, R., Hong, M. and Byon, H.R. (2013) In situ AFM imaging of Li-O_2 electrochemical reaction on highly oriented pyrolytic graphite with ether-based electrolyte. *J. Am. Chem. Soc.* **135**, 10870-10876.